

Investigations on Permeability of Fractured, Steep and Deep Rock Slopes with High Groundwater Pressures

Submitted in partial fulfillment for the requirements
of the degree of

Doctor of Philosophy

of the

Indian Institute of Technology, Bombay, India
and
Monash University, Australia

by

Kunal Kumar Singh

Supervisors:

Prof. D. N. Singh (IIT Bombay)

Prof. Ranjith P. G. (Monash University)



*The course of study for this award was developed jointly by
Monash University, Australia and the Indian Institute of Technology, Bombay
and was given academic recognition by each of them.
The programme was administrated by The IITB-Monash Research Academy*

(Year 2014)

INDIAN INSTITUTE OF TECHNOLOGY BOMBAY, INDIA

CERTIFICATE OF COURSE WORK

This is to certify that **Mr. Kunal Kumar Singh (IITB Roll No. 08404401; ██████████ ██████████ 8)** was admitted to the candidacy of the joint PhD programme of the IITB-Monash Research Academy, after successfully completing all the credits/courses required for the Ph.D. degree programme. The details of the course work done are mentioned below.

Course Code	Course Name	Credits	Grade	Year/Semester
HS 699	Communication and Presentation Skills	4.0	PP	2009-10/Spring
GS 681	Underground Excavation Technology	6.0	AA	2009-10/Autumn
CE 641	Environmental Geomechanics	6.0	AA	2009-10/Autumn
CE 634	Soil Engineering II	6.0	AU	2008-09/Spring
CES801	Seminar	4.0	AA	2008-09/Spring

Verified by Academy Examination Officer
IITB-Monash Research Academy,
Powai, Mumbai, India

Approval Sheet

The thesis entitled: “**Investigations on Permeability of Fractured, Steep and Deep Rock Slopes with High Groundwater Pressures**” by **Kunal Kumar Singh** is approved for the degree of **Doctor of Philosophy**.



(Dr. S K Sharma)
Ext. Examiner



(Prof. T N Singh)
Int. Examiner



(Prof. D N Singh)
IIT Bombay Supervisor



(Prof. Ranjith Pathegama Gamage)
Monash Supervisor



(Prof. P. Phale)
Chairman

Date: 13th March, 2014

**Place: IITB-Monash Research Academy,
IIT Bombay, Mumbai 400076**

CERTIFICATE

This is to certify that the thesis entitled **“Investigation of permeability of fractured, steep and deep rock slopes with high groundwater pressures”** submitted by Mr. Kunal Kumar Singh to the IITB-Monash Research Academy, Bombay, India, is record of bonafide research work under our joint supervision and we consider it worthy of consideration for the award of the degree of Doctor of Philosophy of the Institute.



(Prof. D. N. Singh)
IIT Bombay Supervisor



(Prof. Ranjith Pathegama Gamage)
Monash Supervisor

Date: 13th March, 2014

Declaration

I declare that this written submission represents my ideas in my own words and where other's ideas or words have been included, I have adequately cited and referenced the original sources. I also declare that I have adhered to all principles of academic honesty and integrity and I have not misrepresented or fabricated or falsified any idea/data/fact/source in my submission. I understand that any violation of the above will be cause for disciplinary action by the Institute and can also evoke penal action from the sources which have thus not been properly cited or from whom proper permission has not been taken when needed.

Notice: 1

Under the Copyright Act 1968, this thesis must be used only under the normal conditions of scholarly fair dealing. In particular no results or conclusions should be extracted from it, nor should it be copied or closely paraphrased in whole or in part without the written consent of the author. Proper written acknowledgement should be made for any assistance obtained from this thesis.

Notice 2

I certify that I have made all reasonable efforts to secure copyright permission for third-party content included in this thesis and have not knowingly added copyright content to my work without the owner's permission.


Student Name: Kunal Kumar Singh

IITB ID: 08404401


TABLE OF CONTENTS

ABSTRACT.....	I
LIST OF FIGURES.....	II
LIST OF TABLES.....	IV
NOMENCLATURE.....	V
ABBREVIATION.....	VII
CHAPTER 1.....	1
INTRODUCTION.....	1
1.1 General.....	1
1.2 Motivation for the study.....	2
1.3 Aims of the study.....	3
CHAPTER 2.....	4
FLUID FLOW THROUGH ROCKMASS: BASIC CONCEPTS.....	4
2.1 General.....	4
2.2 Rock.....	4
2.3 Rock Mass Classification.....	4
2.4 Fracture/discontinuity.....	5
2.5 Response of stress on fractures.....	5
2.6 Influence of fractures on stability of slopes.....	6
2.7 Influence of fluid flow on stability of slopes.....	6
2.8 Fluid flow through rockmass- Basic Laws and Concepts.....	7
CHAPTER 3.....	10
LITERATURE REVIEW.....	10
3.1 General.....	10
3.2 Permeability of the fractured rockmass.....	10
3.2.1 <i>Effects of joint geometric parameters</i>	10
3.2.2 <i>Effects of in-situ stress</i>	14
3.2.3 <i>Effects of induced stress due to excavation</i>	20
3.2.4 <i>Effects of slope geometry</i>	22
3.3 Fluid flow through single fracture.....	24
3.4 Quantification (and Measurement) of fractures.....	29
3.5 Roughness measurement of the fracture surfaces.....	31
3.6 Critical appraisal.....	33
CHAPTER 4.....	35
EXPERIMENTAL INVESTIGATIONS.....	35
4.1 General.....	35
4.2 Selection of material.....	35
4.2.1 <i>Analogue material - 'Paraffin wax'</i>	35
4.2.1.1 <i>Sample preparation</i>	35

4.2.1.2	<i>Creation of 'single fracture' in the analogue material</i>	36
4.2.1.3	<i>Particle Morphology of the Standard Sand Grains</i>	37
4.2.2	<i>Natural Material - 'Hard/crystalline rock'</i>	39
4.2.2.1	<i>Creation of 'single fracture' in the natural material</i>	41
4.3	Testing methodology	43
4.3.1	<i>Determination of Engineering Properties of Analogue material</i>	43
4.3.2	<i>Determination of Engineering Properties of natural material</i>	45
4.3.3	<i>Fluid flow characteristics of Analogue Material using FWP</i>	45
4.3.3.1	<i>The Test Setup</i>	45
4.3.4	<i>Roughness measurement of the fracture surface of the Natural Material</i> . 48	
4.3.5	<i>Fluid flow characteristics of Natural Material using HPTC</i>	49
4.3.5.1	<i>The Test Setup and Working Principle</i>	49
CHAPTER 5	52
RESULTS AND DISCUSSION	52
5.1	General.....	52
5.2	Particle Morphology of the Standard Sand Grains	52
5.3	Engineering properties of the material.....	54
5.4	Determination of Flow Characteristics of the Analogue Material.....	54
5.5	Determination of roughness of fracture surface.....	62
5.6	Determination of Flow Characteristics of the Rockmass	67
5.7	A comparison of the flow properties of the analogue and natural materials	85
5.8	Relationship between σ_3 , b_p and Q	86
5.8.1	<i>Analogue Material</i>	86
5.8.2	<i>Natural Material</i>	87
CONCLUSION	88
FUTURE SCOPE	90
APPENDIX	91
REFERENCES	101
SUMMARY	111
PUBLICATIONS	113
ACKNOWLEDGEMENT	114

Efforts have been made in this study to determine fluid flow properties of the fractured rockmass, which greatly influence the construction/execution of any civil and mining engineering projects. In general, any engineering and mining activities brings fractures/discontinuities in the rockmass. Such fracture/discontinuity becomes a pathway for fluid flow. Further, presence of fluid in the fractured rockmass exerts pore water pressure on the rockmass. Increase or decrease in pore water pressure reduces or increases the effective stress respectively. As such, the strength of the rockmass depends on the behaviour of the effective stress. Consequently, an understanding of effective stress and pore water pressure becomes essential for the safe and economical execution of any civil or mining engineering projects.

With this in view, a novel methodology to simulate flow of water through a fractured rockmass, by using an analogue material imbibing a single fracture, was developed. Further, fluid flow experiments were carried out on triaxial samples of granite, containing a 'single rough walled fracture', by employing high confining pressures (≈ 40 MPa) covers depth of upto 1000 m. Elevated fluid pressures (≈ 25 MPa) were applied and different fracture roughness created by selecting granite rock of different grain sizes, were considered in the present study. Furthermore, results obtained from the tests on analogue material and naturally occurring rockmass have been critically evaluated. This study demonstrates the usefulness of analogue material for easy and fast simulation of fluid flow properties through the fractured rockmass rather than resorting to the cumbersome and tedious process of sampling from the deep locations.

Keywords: rockmass, fractures, permeability, extremely high confining and seepage pressures, non-linear flow, laboratory investigations.

LIST OF FIGURES

Fig. 2-1 (a) Normal stress and (b) shear stress Joint deformation model (modified after Gangi and Carlson, 1996)	6
Fig. 2-2 Typical arrangements of irregular fracture surface (a) teeth-teeth and (b) teeth-socket (modified after Zhou et al., 2008).....	8
Fig. 3-1 Variation in permeability (milliDarcy) with effective pressure (MPa).....	18
Fig. 3-2 Closure/opening of cracks due to application of pressures	18
Fig. 4-1 The mould used for preparing the cylindrical samples, (b) cylindrical halves of the sample with adhered sand and (c) the sample with a single fracture.....	36
Fig. 4-2 Optical micro-photographs of the standard sands ($\times 10$)	38
Fig. 4-3 Method to determine the (a) particle morphology (b) Elongation Index, using software AutoCAD, v. 2009 software.....	38
Fig. 4-4 Index Map of Victoria, Australia showing location of the granite rock sample collection site	40
Fig. 4-5 The rock block placed in the rectangular boxes for coring (a) Fine grained granite and (b) medium grained granite	41
Fig. 4-6 V-Blocks setup to create a fracture in the rockmass, (a) Base Plate, (b) Top Plate, (c) both top and bottom plate placed over each other, (d) sample placed in between the top and bottom platen	42
Fig. 4-7 (a) Cylindrical halves of the fractured granite sample, (b) samples with a single fracture	43
Fig. 4-8 A Master loader for determining the engineering properties of the analogue sample	44
Fig. 4-9 Details of the positioning of LVDTs in the above setup (after Patel et. al., 2009)	44
Fig. 4-10 The Humboldt Flexi-Panel HM-4150 permeameter for determination of permeability. a) The Master Control Panel, with the Cylindrical Sample Cell	47
Fig. 4-11 The schematic diagram of the test setup	47
Fig. 4-12 The asperity profile and the statistical parameters associated with it	48
Fig. 4-13 The test setup used for determining the flow characteristics of water through the fractured rockmass	50
Fig. 4-14 The schematic diagram of the experimental setup used for determining flow characteristics of water through the fractured rock mass.....	51
Fig. 4-15 The variation in Q with t for different values of b_p as obtained from fluid flow test.....	51
Fig. 5-1 Typical arrangements of irregular sand grains (a-c) and perfect rounded glass beads (d-e) on sample halves	53
Fig. 5-2 The stress vs. strain relationship of the analogue material.....	54
Fig. 5-3 The variation of Q with σ_3 for b_p equal to (a) 10 kPa, (b) 20 kPa, (c) 30 kPa, and (d) 40 kPa of sample S-SG.....	56
Fig. 5-4 The variation of Q with σ_3 at different values of b_p corresponding to e_i (a) ≤ 1.1 mm ($425\mu\text{m}$) and (b) ≥ 1.7 mm ($710\mu\text{m}$) of sample S-SG	56
Fig. 5-5 The variation of Q with σ_3 of sample S-GB (a) at different values of e_i and (b) corresponding to $b_p = (10, 20, 30$ and 40 kPa).....	57
Fig. 5-6 The variation of Q with σ_3 corresponding to $e_i =$ (a) 0.9 mm, (b) 1.8 mm.....	57
Fig. 5-7 The variation of (a) ΔQ_s and (b) ΔQ_i with σ_3 corresponding to $b_p=10$ kPa.....	59
Fig. 5-8 The relationship between e and σ_3 corresponding to (a) various values of e_i (b) various values of b_p	60

Fig. 5-9 The variation of R_e with σ_3 for b_p equal to (a) 10 kPa, (b) 20 kPa, (c) 30 kPa and (d) 40 kPa.....	60
Fig. 5-10 The variation of R_e with σ_3 corresponding to different values of b_p	61
Fig. 5-11 The relationship between the apparent fracture aperture and the specific flow (corresponding to $b_p=10$ kPa)	61
Fig. 5-12 3-Dimensional surface profile of the fracture surfaces of Samples (a) S1-CG-38, (b) S2-MG-38 and (c) S3-FG-38	64
Fig. 5-13 3-Dimensional surface profile of the fracture surfaces of Samples (a) S1-CG-54, (b) S2-MG-54 and (c) S3-FG-54	65
Fig. 5-14 The variation of Q with b_p for samples (a) S1-CG-38, (b) S2-MG-38 and (c) S3-FG-38	68
Fig. 5-15 The variation of Q with b_p for samples (a) S1-CG-54, (b) S2-MG-54 and (c) S3-FG-54	69
Fig. 5-16 The variation of Q with the σ_3 corresponding to different b_p for the samples S1-CG-38, S2-MG-38 and S3-FG-38.....	70
Fig. 5-17 The variation of Q with the σ_3 corresponding to different b_p for the samples S1-CG-54, S2-MG-54 and S3-FG-54.....	71
Fig. 5-18 The variation of hydraulic fracture aperture, e , with base pressures, b_p , for samples (a) S1-CG-38, (b) S2-MG-38 and (c) S3-FG-38.....	73
Fig. 5-19 The variation of hydraulic fracture aperture, e , with base pressures, b_p , for samples (a) S1-CG-54, (b) S2-MG-54 and (c) S3-FG-54.....	74
Fig. 5-20 The variation of e with σ_3 corresponding to different b_p , for sample S1-CG-38, S2-MG-38 and S3-FG-38	75
Fig. 5-21 The variation of e with σ_3 corresponding to different b_p , for samples S1-CG-54, S2-MG-54 and S3-FG-54	76
Fig. 5-22 Discharge as a function of effective confining pressure, (a) small samples and (b) large samples	77
Fig. 5-23 The variation of R_e with b_p corresponding to different σ_3 , for samples (a) S1-CG-38, (b) S2-MG-38 and (c) S3-FG-38	80
Fig. 5-24 The variation of R_e with b_p corresponding to different σ_3 , for samples S1-CG-54, (b) S2-MG-54 and (c) S3-FG-54	81
Fig. 5-25 A. The computed surface roughness profile from the center of the sample S1-CG-38, showing length l_1 and l_2	81
Fig. 5-26 The variation of R_e with σ_{eff}	81
Fig. 5-27 The variation of Q with σ_3 corresponding to different b_p for coarse grained samples.....	82
Fig. 5-28 The variation of Q with σ_3 corresponding to different b_p for medium grained samples.....	83
Fig. 5-29 The variation of Q with σ_3 corresponding to different b_p for fine grained samples.....	84

LIST OF TABLES

Table 4-1 Particle morphology of the samples of sand grains.....	38
Table 4-2 The elongation index of the samples of sands.....	39
Table 4-3 Engineering properties of the samples and their geometrical details	41
Table 4-4 Detail of fluid flow tests configuration	50
Table 5-1 Computed average initial fracture aperture, $e_{cav.}$, of the samples of sand based on grain model equations.....	53
Table 5-2 Statistical parameters of the surfaces of the fracture/cylindrical halves (all values in mm) for 38 mm diameter rock samples	66
Table 5-3 Statistical parameters of the surfaces of the fracture/cylindrical halves (all values in mm) for 54 mm diameter rock samples	66
Table 5-4 The value of empirical constants appearing in Eq. 5.2 and 5.3.....	86
Table 5-5 The value of empirical constants appearing in Eq. 5.4.....	87
Appendix A Sample designation and geometrical detail of the analogue samples and the fracture, ($l=60$ mm, $W=34.5$ mm).....	91
Appendix B Sample designation and geometrical detail of the samples and the fracture prepared using glass beads ($l=60$ mm, $W=34.5$ mm).....	92
Appendix C Computed Initial fracture aperture, e_c , of S-SG-425 based on grain model equations.....	93
Appendix D Computed Initial fracture aperture, e_c , of S-SG-500, based on grain model equations.....	94
Appendix E Computed Initial fracture aperture, e_c , of S-SG-710 based on grain model equations.....	95
Appendix F A typical datasheet used for recording experimental observations (for S-SG-425, $e_i=1.06 \times 10^{-3}$ m, $b_p=10$ kPa, Trial 1).....	96
Appendix G A typical datasheet used for recording experimental observations (for S-GB-0.45 ($e_i=0.86 \times 10^{-4}$ m, $b_p=10$ kPa, Trial 1).....	97
Appendix H The computed e_a and Q_{sf} values corresponding to different e_i for b_p (= 10 kPa).....	98
Appendix I Typical datasheet used for recording experimental observations and calculated parameters for natural sample, S1-CG-38.....	99
Appendix J The measured and calculated parameters for natural samples,.....	100

NOMENCLATURE

σ	Stress
ε	Strain
ζ	Initial seating stress used in Eq. 3.1
d	Joint closure used in Eq. 3.1
d_m	Maximum joint closure used in Eq. 3.1
t	Exponent used in Eq. 3.1
Q_p	Quality factor of P-wave
Q_s	Quality factor of S-wave
r	Correlation coefficient
K	Acceleration
ε_{trans}	Lateral strain
ε_{axial}	Longitudinal strain
ν	Poisson's ratio
P	Applied load
A_c	Corrected area used in Eq. 4.6
D_c	Corrected diameter used in Eq. 4.7
D_o	Initial diameter of the sample used in Eq. 4.7
$\delta_1, \delta_2, \delta_3,$	Transverse deformation at 120° used in Eq. 4.7
A_g	Area of groove made on two sides of the rock sample (mm^2)
Q	Discharge (cc)
E	Young's Modulus
h	Head (m)
μ	Dynamic viscosity of water ($=1 \times 10^{-3} \text{ N}\cdot\text{s}/\text{m}^2$ at 20°C)
ρ	Fluid density ($=998 \text{ kg}/\text{m}^3$ at 20°C).
σ_3	Confining stress (kPa)
b_p	Base pressure/injection pressure (kPa)
l	Length of sample/fracture (mm)
W	Width of the fracture (mm)
A	Area (m^2)
A_f	Initial area of the fracture (mm^2)
d_f	Final diameter of the sample with sand particles (mm)

d_i	Initial diameter of sample without sand particles (mm)
dP/dL	Pressure gradient over contact length 'L'
EI	Elongation index
g	Acceleration due to gravity (=9.81 m/s ²)
Q	Discharge (m ³ /s)
Q_s	Specific flow, (m ³ /s)
I	Hydraulic gradient (m)
k	Permeability (m/s)
k_i	Intrinsic permeability (m ²)
K_f	Fracture permeability (m/s)
l_1	Major axes of the particle (mm)
l_2	Intermediate axes of the particle (mm)
Re	Reynolds number
e	Fracture aperture (mm)
e_a	apparent fracture aperture (mm)
e_i	Measured initial aperture of the fracture (mm)
e_f	Final aperture of the fracture at certain σ_3 (mm)
e_c	Computed initial aperture of the fracture (mm)

ABBREVIATION

AE	Acoustic Emission
ASTM	American Standard for Testing and Materials
DST	Drift Scale Test
FWP	Flexible Wall Permeameter
HPTC	High Pressure Triaxial Cell
ISRM	International Society for Rock Mechanics
LVDT	Linearly Variable Differential Transducer
MTS	Material Testing System
RQD	Rock Quality Designation
SVI	Sound Velocity Index
THM	Thermal–Hydrological–Mechanical
UCS	Uniaxial Compressive Strength

1.1 General

Investigation of permeability is important in understanding the behavior of fluid flow through the rockmass. Rockmass consists of, intact rock as well as discontinuities/fractures such as, joints, faults, shear zones, bedding plane, lineation, foliation, gneissosity etc. In general, most of the engineering activities (viz., execution of any civil and hydro-geological engineering projects; extraction of ores/minerals, geothermal energy, petroleum and natural gases from the deep earth crust and disposal of nuclear/radioactive waste and greenhouse gases) are associated with hard and crystalline rockmass, which occur at great depths inside the crust. As such, the matrix permeability of the hard and crystalline rock is considerably low and fluid flow in such type of rocks mainly occurs through the fractures, which happens to be quite higher than the intact rock. This leads to seepage/fluid-in-rush related problems during the execution of any engineering projects.

Further, execution of the above mentioned activities will inevitably bring about a concentration of stresses and subsequently local joints or tension fractures in the rock mass come into existence and consequently, decreases the strength of the rockmass. In addition, fluid flow through such rockmass results in the development of excess internal water pressure, which substantially reduces the effective normal stress and hence, further reduces the shear strength of the rockmass. Such a situation may lead to failure of underground constructions (tunnel/mine roof, longwall mines, rock cavern, etc.) and in-stability of any deep and steep open cut slopes. Therefore, understanding the behavior of fluid flow (mechanics and transport of fluid) through a rockmass, especially occurring at great depth (>200 m) and with an elevated groundwater pressures becomes essential for all kinds of surface and underground engineering and mining activities involving water, oil and gas fluid.

In this direction, several efforts were made by earlier researchers (Brace et al., 1968; Jones, 1975; Pratt et al., 1977; Raven and Gale, 1985; Oda, 1985, Zhang and Sanderson, 1995; Inoue and Sugita, 2003; Zisser and Nover, 2009 etc.) by employing different approaches viz., empirical, numerical and combined approach are worth mentioning. In general, investigations were made by considering the geometry of fracture (length, aperture, orientation, roughness etc.), type of the material, and state of stress. It has been

observed that the behavior of fluid flow through the rockmass depends upon the properties of the rockmass (strength, modulus, and Poisson's ratio), properties of fractures (orientation, length, density, aperture, roughness, in-filling materials, and inter-connectivity) and properties of the fluid (density and viscosity) as well. It has also been noticed that the pore dimensions viz., the fracture aperture, or width of the fracture, change with stress, and hence, permeability is quite stress-dependent (Brace et al., 1968; Walsh, 1981; Cook, 1992).

Some other researchers have conducted permeability investigations under in-situ conditions to evaluate the behavior of fluid flow through fractured rockmass at large scale (Hsieh and Neuman, 1985; Wang and Kulatilake, 2002; Rutqvist et al., 2005). Most of the earlier researchers have investigated the fluid flow behavior of intact rock or rockmass having interconnected voids/fracture network. However, fluid flow through rockmass is governed by the flow properties of the fractures or the most prominent single fracture and simulating fluid flow through a fracture network, which is a conglomeration of several individual fractures, is quite intricate and difficult. In addition, a clear understanding of the interaction of various mechanisms and processes such as redistribution of stresses and fluid flow in fractured rocks, fluid-rock interactions, scale effect etc. remains a challenge to the scientific community, due to heterogeneities involved with the rock and rockmass.

1.2 Motivation for the study

This calls for developing techniques that would facilitate measurement of permeability through the fractured rock masses under varied confining stresses and ground water pressures. Based on these studies efforts should also be made to develop a mathematical model which correlates these parameters with the rock mass specific parameters.

Such a model should also corroborate with the results from the other empirical and conventional methods and should be easy to adopt, cost and time effective. It is believed that such model would be quite helpful in providing insight into the seepage induced instability of rock masses and fluid-rock interactions.

1.3 Aims of the study

- To develop a novel methodology, which can simulate flow of water through fractured rockmass, by using an analogue material imbibing a single fracture by employing a flexible wall permeameter, under varied hydraulic heads and confining stresses.
- To estimate mechanical properties (Uniaxial compressive strength, Modulus of elasticity, and Poisson's ration) of triaxial samples of hard and crystalline rock.
- To investigate permeability properties of the triaxial samples of hard and crystalline rock, containing a 'single rough walled fracture', under varying conditions of confining pressures (5 to 40MPa), elevated fluid pressures (upto 25MPa), and fracture roughness, created by selecting rocks of different grain sizes.
- To establish the relation between the analogue and the natural material

CHAPTER 2

FLUID FLOW THROUGH ROCKMASS: BASIC CONCEPTS

2.1 General

A brief discussion on the basic of intact and fractured rockmass and the behavior of fluid flow through the rockmass are presented in this chapter. Also, the basic governing laws for the fluid flow through a single fractured rockmass are discussed herein.

2.2 Rock

A rock is composed of naturally occurring solid aggregate of one or more minerals or an aggregate of organic matter (such as coal), a glassy substance (such as obsidian) which has no crystalline structure. Rock can be divided into intact rock, i.e. homogenous, isotropic, solid, and continuous in nature with no obvious structural defects, and mostly exists only at the hand-specimen scale and rockmass, i.e. heterogeneous and anisotropic in nature, carrying all the structural defects and is exists at the field scale. The rock mass is the total in-situ medium containing bedding planes, faults, joints, folds and other structural features. So, it is essential to characterize the rock mass and fractures for the stability of any civil or engineering geological structures.

2.3 Rock Mass Classification

Rock mass classification is a classification system in which empirical relations between rock mass properties and the behaviour of the rock mass in relation to a particular engineering application, are combined to give a method of designing engineering structures in or on a rock mass. Based on the different site conditions and situations, a number of classification schemes for the rock masses have been developed. These classification schemes assigned the numerical values to those properties or features of the rock mass which are likely to influence its behaviour, and combined these individual values into one overall classification rating for the rock mass. The rockmass classifications are done with an objective to quantify the inherent properties based on previous understanding and to determine the extent of external loading conditions influencing rock mass behaviour. The understanding of such processes will help in successful prediction of rockmass behaviour under different conditions. The earliest attempt of rock mass classification for tunnel support design was made by Terzaghi (1946), in which the rock loads, carried by steel sets, were estimated based on descriptive classification known as, Terzaghi's Rock Mass

Classification. The most commonly used classification schemes in the mining and civil engineering practices are the Rock Quality Designation (RQD) developed by Deere et al. (1967), NGI tunnelling quality index (Q-System) developed by Barton et al. (1974) and CSIR geomechanics or Rock Mass Rating (RMR) scheme developed by Bieniawski (1973, 1976, 1989). Although, several other classification schemes are, Geological Strength Index (GSI) introduced by Hoek (1994), Slope Mass Rating (SMR) proposed by Romana (1985) to evaluate the stability of rock slopes, the Rock Structure Rating (RSR) classification by Wickham et al. (1972) and the Rock Mass index (RMi) system developed by Palmstrom, 1995.

2.4 Fracture/discontinuity

A fracture is any planar or curvi-planar separation or discontinuity that divides the rock into two or more pieces formed due to the stress exceeding the rock strength, such as joint and fault. Fractures can occur in wide range from micro-scale to continental scale. All rocks in the earth's crust are fractured to some extent and occur at a range of scales, from microscopic to megascopic or continental. Fractures can be Joints, Faults, Discontinuity, Bedding Plane, Shear Zones, Foliations, Cleavage, Schistosity, Gneissic Layering, etc. Highly fractured rocks may possess both significant permeability and secondary porosity. Fractures are important in engineering geology, geotechnical engineering, and hydrogeological practices. They can affect the stability of engineered structures and underground excavations. Fractures act as a conductor that can provide pathway for fluid/gas movement such as water, hydrocarbons and ore-forming fluids in rock mass or as a barriers that prevent flow across them. Also, fractures act as conduits for or can control the transport of radioactive, nuclear or chemical contaminants into and through the earth surface.

2.5 Response of stress on fractures

The fractures tend to open or close depending upon the states of stresses. If normal stress acts perpendicular to the fracture surface, then closing of fractures occur (Fig. 2-1a), this reduces the permeability significantly. Whereas, when stress acts parallel to the fracture surface, the width of the fracture increases and hence the magnitude of permeability increases (Raven and Gale, 1985; Zhang and Sanderson, 1995). However, due to confining pressure, (σ_3), the initiation of new cracks retards and it has great effect on the suppression of the axial splitting (Li et al., 1998). It has also been reported that the laboratory and in-

situ permeability results of rock fractures do not show significant dilation for the initial ‘elastic’ shear displacement until a peak shear stress is reached (Zhou et al., 2008).

According to Li et al. (1997), in the strain-softening region, σ_3 has the greatest influence on permeability. However, ratio of pore pressure, (μ_w) to σ_3 have significant effect only in the area of the highest permeability. The wider the aperture, (e), the greater the influence of the σ_3 and μ_w , on the e , so the σ_3 and μ_w slightly influence the permeability in the pre-peak region but exhibit a significant influence in the post-peak region.

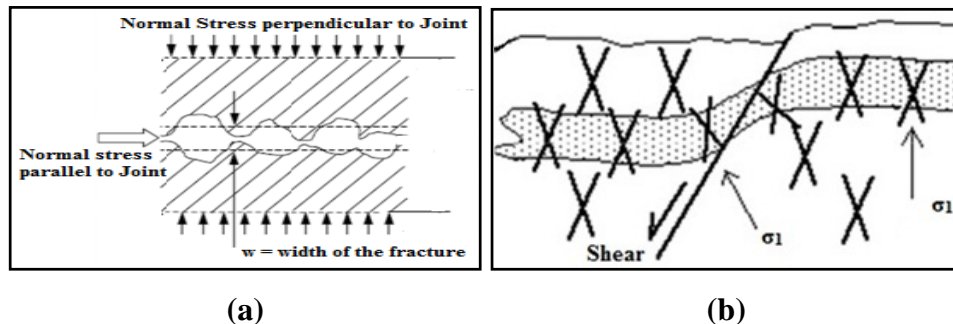


Fig. 2-1 (a) Normal stress and (b) shear stress Joint deformation model (modified after Gangi and Carlson, 1996)

2.6 Influence of fractures on stability of slopes

Fractures play an important role in the stability of deep and steep rock slopes of open-cast or underground mines. All the joint parameters such as orientation, spacing, density, size or extent etc., plays an important role in the stability of rock slopes. Joint sets striking parallel or nearly parallel to the rock slope leads to failure of the rock slopes, therefore orientation of the joints plays a major role in the mechanical and permeability parameters of the rock mass. An underground excavation in a jointed rock mass leads to redistribution of in-situ stresses, which induces substantial amount of deformation (opening or closing of joints) of pre-existing joints (Kim et al., 2004). This is because of the variation in normal stresses acting across the joints or by shear sliding along joints (Fig. 2-1b).

2.7 Influence of fluid flow on stability of slopes

The mechanical properties of a rock mass can be affected in two ways (i) water pressure in the jointed rockmass reduces the effective normal stress, and which reduces the shear stress. The pore water pressure reduces the ultimate strength of the rockmass, under saturated condition. An indirect effect of fluid flow on rock mechanical properties arises from the damaging action of water on particular rocks and minerals such as, in the clay horizon, presence of groundwater reduces the strength and increases the deformability of the rock mass. Argillaceous rocks, such as shales and argillitic sandstones, also demonstrate

marked reductions in material strength following infusion with water (Brady and Brown, 2006). The implications of the effect of groundwater on rock mass strength have significant role in the steep and deep rock slopes of underground excavations, cavern, longwall or open cast mines. In general, permeability of a fractured rock mass would be increased in the zones where stresses are relieved, however, decreased in zones where stresses are increased due to excavation without accompanying shear deformation (Kim et al., 2004).

2.8 Fluid flow through rockmass- Basic Laws and Concepts

Fluid flow through a porous media can be calculated by using Darcy's law (1-D flow):

$$Q = k \cdot i \cdot A \quad (2.1)$$

where Q is the discharge rate per unit area A normal to the flow, i is the hydraulic gradient in the direction of the flow and k is the permeability, which is a material property of both the fluid and the geological medium and may be written as

$$k = k_i \cdot \left(\frac{\rho \cdot g}{\mu} \right) \quad (2.2)$$

where k_i is the intrinsic permeability, g is the acceleration due to gravity ($=9.81 \text{ m/s}^2$), μ is the dynamic viscosity of water ($=8.90 \times 10^{-4} \text{ kg/m}\cdot\text{s}$ for water, at 25°C) and ρ is the fluid density ($=997.05 \text{ kg/m}^3$ at 25°C).

It must be noted here that Equations 2.1, assume that 'A' remains constant, which in reality decreases under the influence of external stresses (Lomize, 1951). However, in case of the fractured rockmass, under the influence of external stresses, the area through which the fluid flow occurs decreases (Balberg and Binenbaum, 1983; Walsh and Brace, 1984; Sour and Ubbes, 1987; Ranjith, 2010). In addition, it has been reported that the magnitude of the fluid flow through a fracture is always higher than the corresponding flow through the surrounding rock matrix (Brown, 1987; Cook, 1992; Min et al., 2009). Further, it is a well-known fact that these complexities cannot be considered by employing Darcy's law and hence differentiating between the fluid flow through a single fracture and through the surrounding rock matrix becomes mandatory. With this in view, earlier researchers (Snow, 1965; Somerton et al., 1975; Kranz et al., 1979; Nuezil and Tracy, 1981; Tsang and Witherspoon, 1981; Brown and Scholz, 1985; Schrauf and Evans, 1986; Tsang, 1992; Nemoto et al., 2009) have employed the following relationship for computing discharge, Q (m^3/s), through a single fracture.

$$Q = \frac{\rho \cdot g \cdot W \cdot e^3}{12\mu \cdot l} (\Delta h) \quad (2.3)$$

where, ρ is the density of water, g is the acceleration due to gravity ($=9.81 \text{ m/s}^2$), W is the width of the aperture normal to the flow path (m), e is the fracture aperture (m), Δh is the difference in hydraulic heads over the fracture length (m), μ is the dynamic viscosity of water and l is the fracture length (m).

Equation 1, which is also known as the “cubic law” assumes linear flow between two parallel smooth plates, spaced at a certain finite distance without any contact, and the flow takes place only through the fracture and not through the matrix.

However, in general, it is difficult to get a smooth wall fracture in nature, and most of the time the fracture surface is rough and irregular with uneven walls contacting each other at discrete points (Rissler, 1978; Brown and Scholz, 1985; Brown, 1987; Indraratna et al., 1999) in the form of teeth-teeth or teeth-socket arrangement, as depicted in Fig. 2-2.

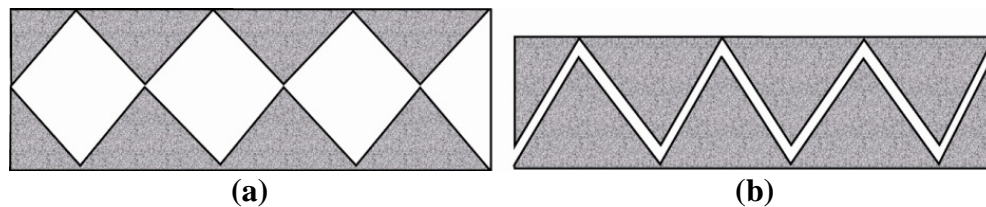


Fig. 2-2 Typical arrangements of irregular fracture surface (a) teeth-teeth and (b) teeth-socket (modified after Zhou et al., 2008)

It has been reported by the earlier researchers (Somerton et al., 1975; Tsang, 1984; Brown, 1987; Cook, 1992; Ranjith, 2010) that the fluid flow through a single fracture is a function of surface roughness, variable fracture aperture, fracture infillings and stress state relative to the orientation of fracture. As such, for determining the flow properties of a single fracture, it is necessary to measure the fracture aperture, as there is a significant decrease in the cross-sectional area of the fracture under the influence of external stress, as stated earlier. However, it is quite difficult to measure the fracture aperture, as fracture asperities make contact at discrete points in case of natural and rough fracture surfaces. Therefore, for the sake of simplicity, simulation of fracture has been done often based on the assumption that the fracture surfaces are smooth and parallel to each other.

Several researchers have investigated the validity of “cubic law” by computing the flow rate through the fractured rockmass, with uneven, rough and deformable natural fracture surface at low confining stresses (Iwai, 1976; Witherspoon et al., 1980; Tsang and Witherspoon, 1983) and the findings of these studies have been used for developing mathematical models (Engelder and Scholz, 1987; ITASCA, 1996).

Further, the fracture permeability (K_f) can be computed by employing the following relationship (Raven and Gale, 1985):

$$K_f = \frac{\rho \cdot g}{\mu} \cdot \frac{e^2}{12} \quad (2.4)$$

For fracture flow, the Reynolds number, R_e , which defines the flow as laminar or turbulent flow, can be determined by employing the following relationship.

$$R_e = \frac{e \cdot v \cdot \rho}{\mu} \quad (2.5)$$

where ρ , v and μ are the density, velocity and dynamic viscosity of the fluid, respectively, and e is the fracture aperture. The flow within fractures becomes turbulent when R_e exceeds the critical value, called the transition R_e , which is equal to 2400 for flow between parallel plates (Lomize, 1951; Louis, 1969).

However, direct measurement of the flow velocity and closure of fracture aperture, due to the application of confining stress during the fluid flow test under triaxial conditions, is quite complicated and necessitates usage of sophisticated instrumentation. Hence, discharge measurement has been preferred over measurement of the flow velocity. Also, knowing the discharge, the fracture aperture can be computed by employing Eq. 2.3. However, to avoid usage of sophisticated instrumentation and back computation of e , earlier researchers (Zimmerman et al., 2004; Ranjith, 2010; Ranjith and Viete, 2011) have preferred to compute R_e , by employing the following relationship.

$$R_e = \frac{\rho \cdot Q}{\mu \cdot W} \quad (2.6)$$

where ρ , Q and μ are the density, discharge and dynamic viscosity of the fluid, respectively, and W is the fracture width which is a function of e .

The flow within the fracture(s) becomes turbulent when R_e exceeds the critical value, called the transition R_e . Incidentally, a wide range of R_e (=10 to 2400) for flow between the (parallel) walls of the fracture has been reported in the literature (Louis, 1969; Wang and Davis, 1996; Oron and Berkowitz, 1998; Zimmerman and Yeo, 2000; Zimmerman et al., 2004; Ranjith and Viete, 2011). However, Zimmerman et al. (2004) have observed complete inertial effects for $R_e > 20$, and Hassanizadeh and Gray (1987) have proposed that non-linearity in flow becomes significant for $R_e > 10$. Marsily (1986) and Ranjith (2010) have observed the critical value of transition in R_e occurs beyond R_e equal to 1150 and 1000, respectively, if R_e is computed by using Eq. 2.5. As such, in short, it can be opined that computing R_e by employing Eq. 2.6 would be handy and practical, in case of straightforward laboratory experimentations, where measurement of flow rates are preferred over flow velocity.

3.1 General

A brief review of the literature that deals with the investigations on permeability of fractured rock and the various parameters that influence the flow in steep and deep rock slope has been presented in this chapter. In addition, literature regarding quantification/measurement of fracture and fracture roughness has also been included in the following.

3.2 Permeability of the fractured rockmass

Permeability is the ability of rocks to transmit fluid through interconnected voids or fractures viz., joints, faults, etc. The behavior of fluid flow through fractured rock mass depends upon the geometry of fractures (orientation, length, density, and connectivity), roughness of the fractures, aperture of the fractures and also on the stress conditions. Several researchers have worked on the permeability of fractured rock mass and are discussed herein.

3.2.1 *Effects of joint geometric parameters*

Goodman (1976) has conducted laboratory measurements of joint closure, across and within a gauge length, as a function of normal stress on artificially induced tensile fractures in rock cores. Measurements have been made for both mated, two halves of the core, placed in the same relative position, and non-mated joints, surfaces were rotated from their original positions relative to one another. It has been observed that non-mated joint exhibit signs of crushing on about 10% of the area of the joint which represents the area of contact between the two surfaces. Based on the results obtained author has proposed the following relationship (Eq. 3.1) that represents the joint closure stress-curves:

$$\frac{\sigma - \zeta}{\zeta} = \left(\frac{d}{d_m - d} \right)^t \quad (3.1)$$

where, σ is the normal effective stress, ζ is an initial seating stress, d is the joint closure, d_m is the maximum joint closure, and t is an exponent.

It has also been noticed that the closure-stress curves are of highly non-linear nature, which can be attributed to inelastic crushing and splitting at the asperities of contact. In this study, author has opined that the correlation between the topographies of each surface for natural joints in the rock mass may differ from those of artificially-induced tensile fractures for a variety of reasons including different loading to produce the fracture, changes in

surface roughness due to dissolution and precipitation or weathering and the effects of relative displacement.

Long et al. (1982) have investigated porous media equivalents for networks of discontinuous fractures. In this study, two-dimensional permeability of a fracture system has been estimated based on directional flow-rates by numerical method. It has been reported that heterogeneity of flow behavior results from fracture geometry in the fractured rock masses.

Balberg and Binenbaum (1983) have conducted a computer aided study of the percolation threshold in a two-dimensional anisotropic system of conducting sticks and have used fracture length, density and orientation to describe the anisotropy of simulated two-dimensional systems of conducting sticks in a given direction. The results indicate that heterogeneity of flow in fractured rock masses is due to the fracture geometry.

Bandis et al. (1983) have studied varieties of natural, unfilled joints with different degrees of weathering and roughness in dolerite, limestone, siltstone and sandstone. In this study, measurements of the displacement across a gauge length on an intact sample and the displacement across the same gauge length of a sample containing the joint have been performed. Later, the difference between these two displacements, at every stress, has been taken into account to determine the joint closure. The obtained results indicate highly non-linear closure-stress curves and the slope of the closure-stress curves tends to a vertical asymptote at high stress, which corresponds to maximum displacement across the joint or maximum joint closure. Cycles of loading and unloading exhibited hysteresis and permanent set that diminished rapidly with successive cycles.

Oda (1985) has calculated the crack tensor and permeability tensor of a fracture system in given directions. In this method, the permeability of a fracture system is dependent on the fracture geometry, including length, density and orientation of fractures.

Shimo and Long (1987) have done numerical modeling of transport parameters in fracture networks. It has been found that the percolation threshold (the critical fracture density) of a fracture system is important to understand the hydraulic and mechanical behaviors of the rock masses.

Cook (1992) has consolidated results of selected research and given personal perspective synthesizes with some new material on mechanical, hydraulic, seismic behavior and properties of single joints, focuses on measurements and analyses of natural joints. Further, author has described how these properties are related to each other, by examining the deformation of the asperities of contact between the two rough surfaces of

joints and of the void spaces adjacent to these contacts through which fluid flows. This study shows that the mechanical stiffness of joints depends mainly upon the area of contact between the two surfaces of a joint. The fluid flow through a joint depends mainly on the smallest aperture in the flow path. The area of contact and the apertures of the void spaces depend on (i) topographies of the two rough surfaces of the joint and (ii) on their deformation under applied stress. Laboratory measurements shows that the transmission of P and S-waves across natural joints at different effective stresses provide the location of individual joints and their specific stiffness's and viscosities by measuring seismic reflections or changes in amplitude and travel time of seismic waves transmitted across them.

Zhang and Sanderson (1995) have investigated anisotropic features of geometry and permeability in fractured rock masses. Based on the fracture spacing and its orientation in a given direction, a geometric anisotropic factor, A_f , for two-dimensional, natural fracture system has been proposed. In addition to this, the effect of average fracture length and fracture orientation on geometric anisotropy factor has also been discussed. The relation of geometric anisotropy and critical fracture density of a fracture system has also been studied. Finally, the directional flow-rates of a fractured system have been calculated using a two-dimensional distinct element code (UDEC). Simulated and natural fracture patterns, sampled on outcrops in the Lake District (U.K.), have been tested to examine the relation between geometric anisotropy and permeability anisotropy to demonstrate a power-law form. It has been reported that geometric anisotropy of fracture system influences the percolation threshold (the critical fracture density) of a fracture system and below this the permeability is negligible. The obtained results indicate that different fracture lengths and their orientation can result anisotropy in geometry of the fracture patterns. Further, authors have mentioned that fracture orientation has a stronger effect than the fracture length and are stronger factor in controlling both geometric anisotropy and permeability anisotropy. Also, it has been mentioned in the study that critical fracture density increases with increase in geometric anisotropy of fracture pattern. The relation between A_f and the anisotropy factor of permeability, A_p , follows a power-law form. Different geometries of fracture patterns have different slopes. Authors have proposed the universal law between average flow rate and fracture density, d , [$q=A_p \cdot (d-d_c)^p$], based on geometric anisotropy of fracture patterns, which results in different universal exponents, p , and the percolation threshold, d_c .

Zhang et al. (1996) have established an approach to evaluate the 2-D permeability tensor for naturally fractured rock masses using Modified Universal Distinct Element Code (UDEC). Directional flow-rates through a unit square of fractured rock under head gradients in two orthogonal directions have been calculated based on the superposition principle. The flow-rates have been transformed into flow-rates through a field rock mass to evaluate the permeability tensor. A sensitivity analysis of fracture pattern geometry on permeability of fractured rock masses has been discussed. Angle between the reference axes and one of two fracture sets, angles of two fracture sets, standard deviation of fracture orientation, fracture length and fracture density etc., have been considered in the study. The effects of stress, (both magnitude and direction), on the permeability of naturally fractured rock masses have been discussed, i.e. the changes in hydraulic fracture apertures under stress condition have been taken into account. The obtained results from sensitivity analysis of fracture patterns indicate that geometric parameters of fractures, such as fracture orientation, deviation angle of fracture sets, fracture length and fracture density have a major effect on the permeability of a fractured rockmass. It has been observed that applied stress and fracture geometry both dominates the permeability of a fractured rockmass. In general, magnitude of permeability decreases with an increase in applied stress. It has also been mentioned that direction of permeability depends on critical value of applied major stress. Further, rotated stress state has been applied to a fractured rock mass and the value of major stress has been found above the critical value. It has been noted that the direction of permeability approximately corresponds with the direction of major stress.

Zhou et al. (2008) have proposed an analytical model to estimate the flow-stress coupled permeability tensor for fractured rock mass based on the superposition principle of flow dissipation energy. The model relies on the geometrical characteristics of rock fractures and fracture network, also, the pre-peak dilation and contraction effect of the fractures under shear loading, empirically considered. The developed analytical model has been validated vis-à-vis with (a) Snow's (1969) and Oda's and Oda et al. models (1985, 1986), and (b) in-situ hydraulic packer tests performed at the construction site of the Laxiwa Hydropower Project, of the Yellow River, China. The authors opined that the proposed model would be quite helpful in rock engineering practice and demonstrate that coupling effect between fluid flow and deformation. It has also been noticed that laboratory and in-situ permeability results of rock fractures do not show remarkable dilation for the initial 'elastic' shear displacement until a peak shear stress is reached.

3.2.2 *Effects of in-situ stress*

Brace et al. (1968) have carried out investigations to determine permeability of the granite under high pressure. Tests have been conducted on samples of granites (Intact rock) for confining pressures ranging from 25 to 444 MPa, and the pore pressure ranging from 15 to 40 MPa. Authors have concluded that the permeability of granite is a function of effective confining pressure, σ_{eff} , and it decreases with increase in σ_{eff} , which is the difference between the confining pressure and the pore pressure, $\sigma_{\text{eff}} = (\sigma_3 - b_p)$.

Jones (1975) has measured permeability of a number of fracture systems (Carthage marble, Smackover limestone, Ellenberger dolomite, and Portland cement with an artificial fracture), under hydrostatic stress condition, and has proposed a linear relationship between the cube root of normalized permeability [permeability at stress divided by permeability at reference stress of 50 psi (344.7 kPa)] and the log of the confining pressure.

Somerton et al. (1975) have established the permeability behavior and sonic velocities of coal fracture systems as a function of the applied stress that simulates the possible in-situ stress condition of underground environment (up to a depth of 2000 ft). Permeability experiments were conducted on three cylindrical samples of bituminous coals of two-inch diameter and three inch length, having large differences in hardness and degree of fracturing with minimum disturbance of the fracture system. For applying radial stress and axial stress, a high pressure [upto 2500 psi (17236.9 kPa)] Hasler sleeve holder has been designed. Nitrogen and Methane gases have been employed as model fluids, axially under a specific sequence of stress conditions. Static elastic moduli and sonic velocities were measured using electrical resistance strain gauges and barium zirconite titanate based piezoelectric transducers (a transmitter and receiver) respectively. For measuring strain, two separate strain gauge indicators (Shinkok model PS7-LT) were connected with pair of strain gauges. Dilatational velocities measure employing first pulse arrival techniques using a Sperry Ultrasonic Attenuation Comparator (Model 56A001). It has been observed that permeability varies over a wide range from 0.1 to 100 milli-Darcy at the lowest stress and exhibits strong stress dependence except for occasional cases, where the stress level or excessive differences in principal stresses cause further fracturing and temporary increase in flow. However, application of repeated stress after further fracturing shows continued reduction in the permeability. It has also been noticed that the permeability decreases by more than two orders of magnitude in the stress range of 250-2000 psi (1723.7 – 13789.5 kPa).

Pratt et al. (1977) have determined the permeability of a 3 m block of granite containing a joint, by applying uniaxial stress normal and parallel to the joint. It has been observed that when uniaxial stress of 12 MPa parallel with the joint is applied, permeability increases by two folds, while permeability decreases to its half of initial value for uniaxial stress of 3 MPa applied normal to the joint.

Witherspoon and Gale (1977) have studied mechanical and hydraulic properties of the rocks for induced seismicity. Authors have reviewed many of the complications apparent from field and laboratory observations and suggested that, at larger scales, more than a meter, there is large variation in the behavior of individual joints and important differences from smaller scale fractures.

Brace (1978) has studied the permeability changes in a geologic material due to applied stress. As stress increases an increase in permeability of nearly threefold in granite, 20% in sandstone, and a hundredfold decrease in compacted sand, has been observed. It has also been noticed that permeability of sand and sandstone did not follow the effective stress law.

Gowd and Rummel (1980) have studied the effect of confining pressure on the fracture behavior of a porous rock by conducting triaxial compression tests on cylindrical sample of sandstone 6 cm length and 3 cm in diameter. Axial compressive stress, σ_1 , was applied by a closed-loop electro-hydraulic servo-controlled loading system using a constant displacement rate of the axial loading piston (10 mm per hr) and axial strain, ϵ_1 , was calculated. Then constant confining pressure, σ_3 , was applied to the specimens by a 2 kbar capacity triaxial fluid pressure vessel and radial expansion (caused due to fracture development or axial compression) of the rock specimen was calculated and finally, total volumetric strain of the rock was determined. The obtained result indicates that macroscopic shear faults developed in intact porous rock at low confining pressure during pre-peak micro-fracturing process whereas, post peak dilation occur at low pressure due to fault dilation. Multiple shear fractures developed at high pressures with progressively less dilation. At 100 MPa confining pressure, transition from brittle to ductile deformation has been taken place and also ductile shear occurred without any dilation.

Witherspoon et al. (1980) have investigated the validity of cubic law for fluid flow in a deformable rock fracture. Experiments of fluid flow through artificial tensile fractures in granite, basalt and marble for apertures down to 4 μm and stresses up to 20 MPa have been conducted. It has been also reported that one of their results, for a joint in marble, shows clear departures from a straight line representing the cubic law. It has been reported

that for apertures $<10\ \mu\text{m}$, the flow decreases more rapidly than the cube of the aperture and at apertures of $<6\ \mu\text{m}$, which corresponds to a stress of more than 10 MPa, the specific flow becomes more or less independent of further reductions in aperture with increasing stress. Authors have concluded that the cubic law is valid for fluid flow through artificial tensile fractures in granite, basalt and marble for low stresses and large apertures.

Walsh (1981) has investigated the effect of both the pore pressure and confining pressure on fracture permeability. It has been shown that the cube root of the fluid permeability, k , is proportional to $\ln p_e$, where p_e is the effective pressure, which is equal to $(p_c - s \cdot p_p)$, where p_c and p_p are the confining pressure and pore pressure, respectively, and s is a constant that varies between 0.5 and 1.0, depending on the topography of the fracture surfaces and the rock type. The obtained result shows that the permeability of fractures increases or decreases with increasing or decreasing effective pressure respectively.

Raven and Gale (1985) have studied the water flow in natural rock fractures as a function of applied stress and sample size. In this study the steady-state radial flows of water from the central hole to the circumference of cylindrical samples of granite sample ranging in sample diameter from 0.1 to 0.294 m have been measured as a function of stress. Also, joint closure-stress curves have been measured on samples of granite. Each cylindrical sample contained different part of the same natural joint orthogonal to its axis. The joint was bolted together along the axis of the core to avoid the damage to the joint surface, and to preserve the relative positions. It has been found that closure-stress curves were highly non-linear with significant permanent set and hysteresis on the first cycle of loading. This has been attributed to the disturbances to the joint surface during handling. For the later cycles, behavior of joint under in-situ condition exhibited greater closure across the joint for the larger sample. Correspondingly, the specific stiffness has been less for the larger sample than it has been for the smaller sample. Also the stiffness's were not linear functions of stress except for the smaller sample and joint stiffness tends to asymptote to some constant value at the higher stresses. An asymptotic stiffness indicates that the geometry of the asperities of contact has no changes due to applied stress. However, there must still be substantial void space to accommodate the deformations from which the finite joint stiffness results. It has been attributed to the fact that the distribution of asperity heights is not exponential rather, it is, Gaussian or inverted chi-square. This has been due to large fraction of all the asperities contact at certain values of stress. Their results show departures from the cubic law, i.e., at large apertures, corresponding to low stresses, flow decreases faster than the cube of the apertures for the fracture surfaces separated by

particles of grit. However, the specific flow becomes insensitive to changes in aperture corresponding to high stresses and for small apertures. Actual flow measurements suggest that, the flow asymptotes to some constant value corresponding to the aperture-independent flow at the highest stresses.

Zhu and Wong (1997) have studied the transition from brittle faulting to cataclastic flow, permeability evolution. It has been reported that the permeability of sandstones consistently decreases with decreasing strain and samples that were subjected to confining pressures ranging from 13 to 550 MPa and a pore pressure of 10 MPa. These observations were independent of whether the sample showed strain softening or hardening and failed by shear localization or cataclastic flow.

Zisser and Nover (2009) have studied the anisotropy of permeability, at effective pressures up to 100 MPa, and complex resistivity, in the frequency range of 1 kHz to 1 MHz, of low permeable sandstone samples of diameter 30 mm and length 20-35 mm collected from a depth of 3000 m of a gas reservoir located in the Northwest German Basin. It has been observed that the permeability of the investigated fractured sandstones decreases continuously with increasing effective pressure (up to 100 MPa) up to two orders of magnitude, while the porosities noticed to be remain unchanged. Also it has been noticed that the anisotropy of permeability is a strong function of applied pressure and for an applied pressure change of the preferred flow paths occurred. Further, it has been observed that the formation factor increases with increasing effective pressure and the spectra of complex resistivity also exhibit dependence on effective pressure. Also, authors attempted to relate permeability with electrical parameters measured corresponding to a particular effective stress.

Data obtained from experimental studies (Brace, 1968; Brace et al., 1978; Kranz et al., 1979; Bernabe, 1988; Zisser and Nover, 2009) on low permeability hard and crystalline rocks were compiled, as indicated in Fig. 3-1.

The figure shows variation in permeability with effective pressure (confining pressure – fluid pressure) of different rock types. It can be inferred from the figure that, (a) significant changes in permeability occur due to increase in effective confining pressure, (b) jointed/fractured rock permeability is greater than that of intact rock permeability (Brace, 1977; Kranz et al., 1979). This variation is mainly caused due to the closure of inter-connected pores or can be attributed to the closure of open cracks and therefore of the preferred flow paths of the fluid (Gangi, 1978; Jones and Owens, 1980) at higher confining pressure/stresses. Incidentally, distribution and orientation of the fractures and other rock

fabric elements (like sedimentary layering, shear zones, lineation, gneissosity etc.) also influence the permeability, and mechanical characteristics of rocks. In addition, the state of stress also influences the permeability of the fractured rock mass significantly (Fig. 3-2). If stress acts perpendicular to the fractures/joints then joints closes up and hence reduces the permeability significantly, whereas, if fluid pressure becomes higher than the surrounding stresses, joints opens up and increases the permeability of the medium.

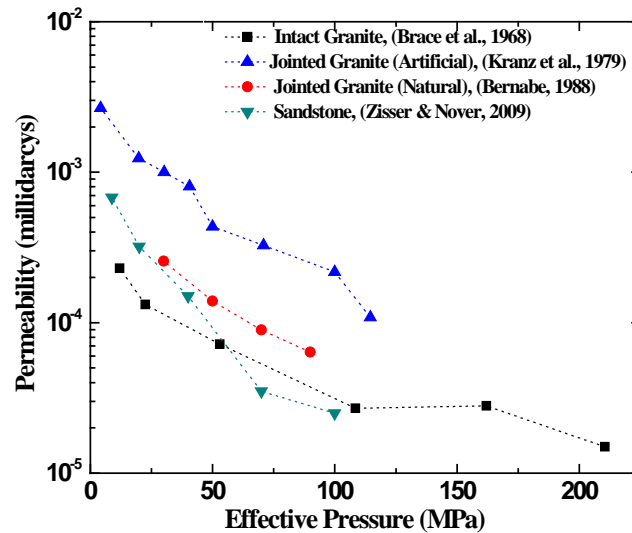


Fig. 3-1 Variation in permeability (milliDarcy) with effective pressure (MPa)

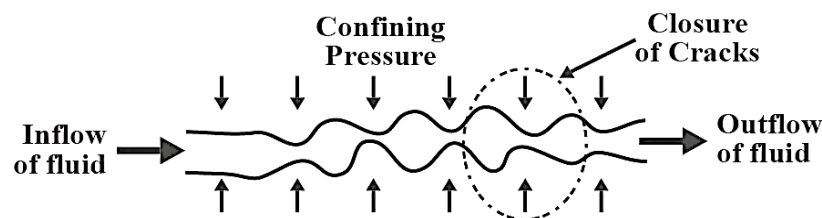


Fig. 3-2 Closure/opening of cracks due to application of pressures

Numerical approach or modeling is essential for scaling the experimental results to field scale and also preferred over empirical approach due to involvement of complicated test apparatus and tedious procedures. In this regard, several researchers have worked on the behavior of fluid flow through fractured rockmass as discussed in the following.

Gangi (1978) has studied variation of the whole and fractured porous rocks permeability with confining pressure and derived phenomenological models to determine the variation in permeability with the confining pressure, P , of whole porous rocks and fractured porous rock. In this study, two models have been used to derive the permeability

variation, Hertzian theory of deformation of spheres model for whole porous rocks and ‘bed of nails’ model for fractured porous rock. Later, comparison of experimental data with the theoretical curves have been performed, which shows that good correlation exists between the two models and given reasonable values for the constants k_0 , P_1 and m , where, P_1 is the effective modulus of the asperities (is of the order of one-tenth to one-hundredth of the asperity material bulk modulus) and m is a constant ($0 < m < 1$) which characterizes the distribution function of the asperity lengths. Based on the results obtained, it has been found that for whole porous rocks, the normalized permeability, $k(P)/k_0$ decreases with increasing normalized confining pressure, P/P_0 , where, k_0 and P_0 are the initial permeability and initial pressure respectively. The permeability and porosity show the same variation with pressure for more than one cycle, if the effective pressure is not too high and if the porous rock is well cemented or for well packed non-cemented aggregates.

Li et al. (1994) have investigated the permeability in Yinzhuang sandstone under various confining pressure and pore water pressure, with respect to a complete stress–strain path by employing an advanced test setup, MTS-815.02S, Electro-Hydraulic Servo controlled Rock Mechanics Testing System. It was found that permeability is a function of the axial stress and strain. By employing curve-fitting techniques, polynomial permeability–strain equations have been derived that reference different stress–strain regions, such as, the elastic, elasto-plastic, peak value, post-peak strain softening and plastic flow regions.

Li et al. (1997) have studied the effect of confining pressure, pore pressure and specimen dimension on permeability, by conducting series of tests using MTS 815 Electro-Hydraulic Servo-controlled Rock Mechanics Testing System on Yinzhuang sandstone, based on an orthogonal experimental design and the mathematical statistical analysis. Based on the result obtained, it has been found that for most regions in a complete stress–strain path, effects of confining pressure, pore pressure and specimen’s dimensions on permeability were not obvious. However, in some individual regions, individual factors has been found to have a significant effect. For example, the confining pressure has great influence on permeability in the strain-softening region, whereas the ratio of the pore pressure to the confining pressure has been found significant only in the area of the highest permeability. It has been observed that wider the aperture of the fissure, the bigger the influence of the confining pressure and pore pressure on the aperture of the fissures, so the confining pressure and pore pressure have minor influence on the permeability in the pre-peak region, whereas, have significant influence in the post-peak region.

Li et al. (1998) have investigated the stress-strain behavior of rock material related to fracture under compression and developed a constitutive model to describe the relationship between the macro deformation of rock and the micro fracture within rock. Using this model, authors have estimated the propagation of micro-cracks, the non-linearity of deformation, the loading and unloading hysteresis and the variation of the apparent Young's modulus, E and Poisson's ratio, ν . The result obtained from model simulation demonstrate that i) the fracture toughness, initial crack length, crack density and Young's modulus are four crucially important parameters that affect the deformations behavior of rock, ii) the elastic parameters (E and ν) of rock matrix should be measured in triaxial tests, iii) the confining pressure retarded the initiation of new cracks and has great effect on suppression of the axial splitting, and iv) the slope of the reloading stress-strain curve has been a measure of the damage in the specimen.

Wang and Park (2002) have investigated the fluid permeability of sedimentary rocks (viz., mudstone, sandy-mudstone, sandy-shale, medium sandstone and fine sandstone) during triaxial compression test on samples of diameter 54 mm and height 55 mm to 80 mm using Electro-Hydraulic Servo-controlled Rock Mechanics Testing System (MTS 815) under maximum confining and pore pressures of 50 MPa. Results obtained were correlated with the stress-strain response of these rocks. Also, measurements of in-situ fluid flow and pressure in floor strata in a double longwall mining face of the Yangzhuang colliery, China, were carried out. Based on obtained laboratory and in-situ investigations authors have developed 3-D numerical model using FLAC^{3D} for better understanding of the change in hydraulic behavior around the mining faces and to provide insight into the mechanism. It has been found that the permeability initially decreases with loading after which it gradually increases with increasing load, and, in general, it is directly proportional to the pore pressure and inversely proportional to the confining pressure. It has also been observed that the permeability of rock is maximum during the strain softening stage rather than at its peak strength. Authors have also found that the porosity and mineral content of the rock influence the permeability.

3.2.3 Effects of induced stress due to excavation

Kim et al. (2004) have worked on the flow analysis of jointed rock masses based on excavation induced transmissivity change of the rough joints. In the present work, a number of numerical techniques (the Micromechanics-Based Continuum (MBC) model-FE excavation analysis in a jointed rock mass and FracMan/Mafic package-FE flow and

transport analysis in the discrete network of joints) has been employed to evaluate the changes in the flow properties of a jointed rockmass, induced due to excavation. A separate computational module connecting these two codes has been incorporated to modify the excavation induced transmissivities by initially imposed ones. The effect of excavation on the flow properties has been evaluated by including these excavation-induced transmissivity changes of individual joints in the FE flow analysis. Numerical and analytical techniques have been developed to compute the excavation-induced transmissivities of flow through a single rock joint. The excavation-induced transmissivity calculation involves the distributions of shear displacements and normal stresses around the excavation, and indirectly takes account of the effect of surface roughness.

Rutqvist et al. (2005) have validated the drift scale test (DST), which is a large scale underground heating field test, by comparing the results vis-à-vis those obtained from different numerical models. The basic intention is to predict and simulate the coupled thermal–hydrological–mechanical–chemical behavior in unsaturated fractured and welded tuff from a side alcove of an underground tunnel of Yucca Mountains, Nevada, U.S.A. The test includes simulation of heat transfer by conduction and convection, liquid and vapor water movements, mineralogical and petrological studies, pore-water chemical and isotopic analysis, rock-mass stress and displacement, and stress-induced changes in fracture permeability. The predicted response of models have been evaluated by comparing in-situ measurements of temperature, water saturation (employing geophysical measurements), rock-mass classification, fracture mapping, video logging of boreholes, rock-mass displacement, and changes in permeability estimated through air injection tests. The test results indicate a good correlation between simulated and measured THM data and adopted continuum model approaches has been revealed adequate for simulating relevant coupled THM processes at the DST. Also, thermo-mechanically induced rock-mass deformations are found to be reasonably well predicted using elastic models, but some local displacements appeared to be better captured using an elasto-plastic model. It has been concluded that fracture closure and opening caused due to the changes in normal stresses across the fractures and were the dominant mechanism for changes in the intrinsic fracture permeability.

Chen et al. (2007) have developed a methodology to quantify the changes in hydraulic conductivity resulted from engineering disturbance, material nonlinearity and anisotropy in rock masses. Authors have developed an equivalent elasto–perfectly plastic constitutive model for the fractured rock mass under complex loading conditions, non-

associated flow rule and mobilized dilatancy to describe the nonlinear response of the rockmass. Fractured rockmass has been modeled by cutting 'n' sets of planar and parallel fractures of constant apertures having different fracture geometry. Based on results from field tests, numerical simulations, and back analysis techniques, different techniques have been proposed to quantify the hydraulic conductivity tensor. Strain-dependent hydraulic conductivity tensor has been formulated for the disturbed rock masses by integrating the normal compressive deformation of the fractures, the effect of material nonlinearity and post-peak shear dilatancy and by separating the deformation of fractures from the equivalent medium. Using this methodology, a closed-form solution has been derived to describe the hydraulic behavior of a single fracture during combined normal and shear loading processes. This methodology has been validated under wide ranges of normal and shear loads by an existing coupled shear-flow test. Numerical simulations have been performed to investigate the changes in hydraulic conductivities of a cubic block of the fractured rock mass under triaxial compression and shear loading. Circular underground excavation has been investigated under a biaxial stress field at the Stripa mine, Sweden. The observed results demonstrated that the shear load drastically changes (in the magnitude of as high as 4–5 orders) the hydraulic properties of the fractured rocks, and lead to anisotropic hydraulic conductivity tensor. The simulation results have been found to match very well with the in-situ experimental observations as well as with an existing elastic strain-dependent analytical solution. It has been opined that the proposed model is capable of predicting the changes in hydraulic properties of the fractured rockmass under loading or excavation loads.

3.2.4 Effects of slope geometry

Water plays an important role in the stability of the stability of steep and deep rock slopes of underground excavations, cavern, longwall or open cast mines. As such, investigations related to the permeability of the deep and steep fractured rockmass under stressed condition becomes essential. Several researchers have worked on the effect of fractures and fluid flow on the stability of steep and deep rock slopes under different stressed environment, and are presented in the following.

Singh and Gahrooe (1990) have determined the stability and sensitivity analysis of slopes in heavily jointed rock masses with planar, circular or combined modes of failure. FORTRAN77 code, has been employed to generate a computerized solution for stability analysis of slope in heavily jointed rockmass. In this study, two typical slopes of an open pit coal and iron mines have been selected. In the open pit coal mines, coal seam was

overlaid by soft tuff and existing failure has been occurred along the coal seam, where the soft tuff has been broken out at Toe. Whereas, in the iron mine dolerite has been overlaid by shale formation and within which failure surface has been passed. The data from these sites has been used and analysed for dry and wet states. In order to assess the effect of water level on factor of safety, phreatic surface has been arbitrary chosen. The obtained results of sensitivity analysis indicated that the inter-slice strength parameters have an effect on the factor of safety. The effect of vibrations (blasting, earthquake, etc.) and acceleration on the factor of safety of slopes have been shown in the plot of factor of safety (F), against acceleration (K). The influence of various strength parameters on the F and the K , have also been considered in this paper.

Pariseau et al. (1997) have studied the large scale open pit copper mine to determine the effect of water, time and mining activity on the rock slope stability using coupled two-dimensional finite element code (simultaneous effects of rock mass deformation and transient fluid flow) assuming poroelastic/plastic behavior. The results have been compared with the previous poroelastic/plastic results of a generic homogenous, isotropic rock slope cut at a depth of 300 m (1000 ft) at an angle of 45 degrees and bench height has been kept as 15 m, in a rockmass with reasonable values of elastic moduli, strengths and hydraulic conductivity. In this study, the pre excavation total stresses, slope geometry, elastic moduli, hydraulic conductivities, water pressure and rock mass deformation have been taken into account. A two dimensional finite element model has been generated for a cross-section (DD) through the north wall of the pit. A total of 11,248 elements have been used in this model. The observed results indicates that in the poroelastic case, strength does not limit stress and potential zones of yielding indicated by regions of low factor of safety (high stress) diminish in time. It does not occur in the more realistic elastic/plastic model. In such case, neither hardening nor softening has been allowed, which increases or decrease stability respectively.

Shiotani (2006) has described the methodologies to mount the Acoustic Emission (AE) sensors into the rock slope to monitor the AE, developed due to the elastic wave's that generated by the initiation, formation/growth and coalescence of cracks for evaluating the long-term rock slope stability.

Pantelidis (2009) has assessed the rock slope stability based on earlier developed rockmass classification systems. In this study, attempts have been made to review the rockmass classification systems in order to identify potentially hazardous rock cut slopes. The study has illustrated main differences and similarities among the classification systems,

and the relevant recommendations has also been proposed. The present study highlights that the existing rock mass classification systems, which contains following parameters, i.) Intact rock strength, ii.) RQD index, iii.) Groundwater outflows, iv.) Method of excavation and v.) Failure history. It has been opined that as stability of rock cuttings predominately governed by discontinuities, and failure occurred due to excess intact rock strength will be highly improbable. Based on the comparative study, author has given the following recommendations as, (i) each possible failure type must be examined independently. (ii) the dip and orientation of discontinuities are the stability (major tectonic or weathering induced discontinuities) parameters, which can be measured on-site and expressed in a quantitative manner. Factors related to the rock mass condition and the triggering mechanism have been found as a key component for the attainment and reliability of every system envisioned for the assessment of the hazard for failure of rock cuttings quantitatively.

3.3 Fluid flow through single fracture

Tsang (1984) has investigated the effect of tortuosity and connectivity on fluid flow rate through a single rough fracture and discussed implications with regard to the theoretical prediction of fluid flow through rough fractures. In this study, flow paths has been represented by electrical resistors placed on a two-dimensional grid, and the resistances varied as the inverse of cube of fracture aperture. Derived and hypothetical analytical solution generated fracture apertures have been used in a parametric study to investigate the dependence of tortuosity on fracture roughness. It has been observed that the more the smaller apertures present in the aperture distribution, the larger the effect of tortuosity. The aperture distributions has been found to be invariably large at small apertures, when the fraction of contact area between the fracture surfaces rises above 30%. Further, the effect of fracture roughness and flow path tortuosity decreases flow rate from the value predicted by the parallel plate representation of a fracture by three or more orders of magnitude. Finally, author has finished the discussion with the question that whether tortuosity has importance or not in flow through real fractures and how the fractional contact area of a fracture varied as a function of stress.

Brown (1987) has presented a direct approach to the study of fluid flow through fractures using the finite-difference method, (FDM). In this study, computer simulation of laminar flow between rough surfaces, based on Reynolds equation, (a form of the Navier-Stokes equations) has been performed. Realistic rough surfaces has been generated

numerically using a fractal model of surface topography and pairs of these surfaces were placed together to form a "joint" with a random aperture distribution. Flow rate through joints has been computed on the 2-dimensional aperture mesh employing FDM and solution has been used in the well-known 'Cubic law' to get the hydraulic aperture for various surface roughness's (fractal dimensions). Further, the hydraulic aperture has been compared with the mean separation of the surfaces. It has been observed that at large separations the surface topography has little effect. On the contrary, at small separations the flow has been found to be tortuous, tending to be channeled through high-aperture regions. It has been noticed that the parameter most affects fluid flow through rough joints was the ratio of the mean separation between the surfaces to the root-mean-square surface height. It has also been observed that though the aperture has been not unique for a rough walled fracture, it allowed the cubic law to approximate the flow through fractures within a factor of 2. It has been noticed that use of the arithmetic mean value of the aperture has given better results than more complicated arithmetic averages.

Pyrak-Nolte and Cook (1988) have investigated the fluid percolation through single fracture. Authors have opined that before addressing problem of flow through fractures or set of fractures in rockmass, it has been necessary to investigate the flow behavior of fluid through the primary unit i.e., single fracture in rock. In this study, the authors have investigated the large values observed for the exponent 'n' in Equation (3.2) given by, (Raven and Gale, 1985; Pyrak-Nolte et al., 1987) in a simple way that include mechanical deformation and results from percolation theory without requiring detailed fluid transport calculations.

$$Q - Q_{\infty} \propto (e_a)^n$$

$$\propto (d_{\max} - d_{\text{mech}})^n \quad (3.2)$$

where, Q is discharge; Q_{∞} is residual or irreducible flow; and apparent fracture aperture, $e_a = (d_{\max} - d_{\text{mech}})$, has been defined as difference between maximum value of stress and the fracture deformation.

Authors have assumed three basic assumptions: (1) cubic-law dependences have been explicitly assumed at the microscopic level; (2) the details of the deformation mechanics of the fracture surface have been included to lowest order by requiring conservation of rock volume; and (3) the macroscopic flow properties have been dominated by the deformation of the critical neck. Authors have discovered macroscopic dependences of flow on apparent aperture that have exponents larger than cubic, but with cubic dependence as a lower bound.

Hakami and Larsson (1996) have carried out flow experiments and aperture measurements on the same specimen having a single natural fracture, to compare the measured flow with the predicted flow based on geometrical parameters describing the actual fracture void space. Authors have developed a technique to measure the aperture by injecting fluorescent epoxy in the fracture specimen. An image analysis system has been employed in this study to take measurements along sections across the fracture surface in granite having a mean aperture of 360 μm at 0.45 MPa, normal stress with spatial correlation of the aperture of about 1 cm. It has been observed that the predicted and measured flow through the fracture specimen were in good agreement and ratio between calculated and measured flow was 2.4.

A comprehensive review of single-phase flow thorough rough walled fractures including deviation of cubic law has been discussed by Zimmerman and Bodvarsson (1996). The authors have addressed the problems related to the hydraulic conductivity of a single fracture to the geometrical parameters (mean aperture, fractional contact area, etc), topography of the fracture walls and asperities. Authors have also compared various theoretical models to sets of data available from the literatures in which conductivity and aperture statistics have been measured on the same rock fracture. It has been observed that in general, reasonably accurate predictions of conductivity can be made by combining the perturbation result, and the geometric mean, with the tortuosity factor.

Brown et al. (1998) have developed a method for obtaining precise replicas of real fracture surfaces using transparent epoxy resins to study the fluid flow paths within a fracture plane. In this study, rocks having natural fracture were collected and silicon rubber molds of fracture surfaces have been used to make a transparent epoxy replica of original fracture. Digitized optical images have been used to observe wetting, saturated flow, and drying of the specimen. Nuclear magnetic resonance imaging has been used for quantitative measurement of flow velocity. It has been observed that both video imaging and nuclear magnetic resonance imaging techniques have distinct and strong channeling of the flow at the sub-millimeter to several-centimeter scale. Authors have discovered that fluid velocities range over several orders of magnitude, with the maximum velocity of factor of 5 higher than the mean velocity. It should be noted that the fluid velocities have been measured simultaneously at various locations along the fracture plane during steady state flow, suggests flow channeling in fractured rock, which can cause the break through velocity of contaminants to far exceed the mean flow.

Inoue and Sugita (2003) have studied the fourth- order approximation of fluid flow through rough-walled rock fracture based on Reynolds lubrication equations. In this study, a stochastic partial differential equation using perturbative expansion method has been adopted for analyzing the fluid flow through a rough surface of single rock fracture. The results were compared with the numerical deterministic analysis for randomly generated aperture distributions and indicate that second-order approximation as shown by Zimmerman and Bodvarsson (1996), which has been valid only when the aperture distribution was nearly isotropic.

Giacomini et al. (2008) have investigated the flow anisotropy within a single natural rock joint subjected to mechanical shear. In this study, micro-scale roughness has been taken into account to define a reduced coefficient of permeability. Numerical simulations have been performed by applying Darcy's law to the rock joint, described as an equivalent porous medium. The numerical simulations were based on experimental data obtained by Hans (2002) from a series of hydro-mechanical shear tests on a rock joint replica (five shear steps of the hydro-mechanical test, from $W = 2$ to 10mm with a 2mm increment). Further, the numerical results were compared to the experimental ones, and to the results obtained by applying the Reynolds equation, to assess the significance of the simulations. The obtained results indicate that linear evolution of flow rate versus injection pressure has been seen for relative tangential shear displacement, W , ranging from 4 to 10 mm. It has been observed that the flow was turbulent at $W = 2$ mm (non-linear evolution) and the model has reproduced the flow anisotropy and given realistic values of fluid velocities.

Tempone and Lavrov (2008) have investigated the applicability of discrete-element method (DEM) for mudloss (occur during overbalance drilling of petroleum wells) modelling in naturally-fractured formations (Single fractures and fracture networks), and to perform an initial parametric study using two dimensional discrete-element code UDEC. In this study, authors have assumed the in-situ stresses as isotropic and equal to 30 MPa, the formation fluid pressure as equal to 20 MPa. The normal K_n and shear K_s stiffness of the joints was equal to 10 GPa/m except for the series of simulations in which K_n was varied as part of a parametric study. The authors have observed that in the case of mudlosses into a fracture network, the total length of the network and the fracture stiffness control the cumulative loss. Further, the dynamics of a mudloss event, i.e. the duration, the ramp-up and the tail in the mudloss flow rate *versus* time curve, has been controlled by the geometry of the fracture network (network being more or less isometric or elongated).

Ranjith (2010) has performed triaxial tests on single natural fractured granite specimens (width of 54 mm and length of 110 mm), having joint roughness coefficient, (JRC<10), to discover whether the phases of fluid flow within rock fractures has been laminar or turbulent using two-phase flow of air and water. It has been observed that the estimated Reynolds numbers for various inlet fluid pressures were $Re \leq 1000$. Further, both single and two-phase flow through rock fractures has been characterized as laminar flows at moderate inlet fluid pressures. However, for single-phase air flow, an increase in inlet air pressures has been resulted in the formation of turbulent flow. It has been also observed that at confining pressure of 1.0 MPa and inlet fluid pressure up to 0.5 MPa, an approximate linear relationship exist between Reynolds number and fluid pressure, and beyond the fluid pressure of 0.5 MPa, the linear relationship diminishes. Further, at low confining pressure, the two-phase Reynolds number of water has been observed as much larger than that of the air phase and an increase in fluid pressure has caused the Reynolds number to change. The author has opined that at elevated fluid pressures, flow cannot be modeled using conventional cubic law. This may be because of the formation of non-linear laminar flow or turbulent flow. Reynolds number depends mainly on the joint surface roughness, the fluid properties and the inlet fluid pressure, and Reynolds numbers increases with the increase in inlet fluid pressure. The magnitude of the critical Reynolds number represented the flow regimes between parallel walls was 1000 and indicated that the single-phase flow derived in this study was laminar.

Qian et al. (2011) have studied the effect of roughness and Reynolds number ($Re > 10$) on fluid flow in rough-walled single fractures to examine the validity of cubic law. In this study, authors have glued identical square plates on one surface of single fracture to simulate the fracture roughness precisely and have control over the aperture and surface roughness. Experiments have been performed on the vertical fracture constructed by employing two plexiglass plates of dimensions 982 mm in length and 250 mm in width under varying hydraulic gradient from 0.015 and 0.046 and six different fracture roughness's. The different fracture roughness has been created by gluing identical plates following a regular order on one of the fracture surface. Two different sizes of square of 40 mm \times 40 mm and 20 mm \times 20 mm with three different thicknesses of 1, 2, and 3 mm have been used to generate six different roughness patterns. The artificially created single fracture has been mounted vertically in a tank which has been connected with two constant-head flumes to establish steady-state horizontal flow in the fracture. Various flow discharges have been created to examine the flow schemes under various Re values and

fracture roughness. The results of the study have been illustrated the relationship between flow rate and the hydraulic gradient for flow in an SF based on various controlled surface roughnesses. It has been observed that increase in the roughness deviates the flow within the fracture from the Darcian flow, and becomes more turbulent. Linear flow close to Darcian flow has been observed through smooth and homogenous fracture surfaces. Further, greater hydraulic gradient has been lead to greater deviation from the cubic law.

3.4 Quantification (and Measurement) of fractures

As fractures play an important role in fluid/gas flow, in the stability of deep and steep slopes of underground or open-cast mines, caverns, for storing safely contaminated materials and nuclear/radio-active wastes in far deep underground sites, designing the blasting and grouting patterns, their quantification or measurement becomes mandatory. In the past, several researchers have worked on the quantification of fractures and fracture geometry with the seismic wave measurements. Some of these efforts have been presented in the following.

Boadu (1997) has related the seismic properties and fractured rock mass parameters based on a modified displacement discontinuity fracture model. In this study, models of fractured medium were developed to represent vertically aligned fractures embedded in an intact rock and seismic properties viz., compressional and shear wave velocities and quality factors, Q (which is the inverse of the attenuation), are computed from the seismic waves measurements. Two models have been developed viz., Model-A and Model-B with four and seven vertically aligned fractures of average length of 0.8 m imbedded in a section of sandstone of length of 2 m, respectively. The discontinuity index I_d , fracture density parameter C , and the RQD, were also computed for simulated distribution of the geometric fracture properties i.e., the fracture length, spacing, aperture, type of infilling material (viscosity), and the areal fraction of opposing fracture faces in contact. These factors have been analyzed and related to the seismic properties. The obtained results has been indicated that fracture properties strongly influence the hydraulic transport properties or the strength of the fractured medium. In addition, seismic velocities (both P and S wave) decrease with an increase in the discontinuity index I_d and the fracture density parameter. It has been opined that low velocity zones may indicate high transmissivity fractured zones. A fractured rockmass with high I_d indicates high permeability and, hence, lower-velocity fracture zones will also have higher permeability. Further, it has been opined that a fractured rock mass with lower strength or RQD value will tend to possess lower seismic

velocities. Author has also stated that the seismic quality factor Q (P and S) decreases with an increase in I_d and C , and also decreases with a decrease in RQD. In addition, the ratio Q_p/Q_s has provided different signature from either Q_p or Q_s in terms of its variation with I_d , C , and RQD. It has been further opined that permeable or hydraulically transmissive zones were indicative of consistent low seismic velocity and Q values associated with a fracture zone. Lower seismic velocity and Q values were associated with low strength rocks. The fractures caused a time delay in the propagating waveform and act as a filter by attenuating the high frequency in the range of the waveform. The results exhibited that reasonable inferences has characterized the hydraulic and strength properties of fractured rockmass, which may have been derived from the measured seismic properties.

Kahraman (2001) has developed a relationship between P-wave velocity, number of joints and Schmidt hammer rebound number by conducting test on artificially created joints in different types of rocks. Both field and laboratory studies have been carried out. Schmidt hammer (N-Type) tests have been performed on six different types of rock blocks, keeping the hammer vertically downwards and at right angles to the horizontal rock faces. Laboratory tests have been performed on artificially created jointed rock samples having dimension $100\text{ mm} \times 200\text{ mm} \times 10\text{ mm}$ and P-wave velocity were measured perpendicular to the joints after applying the axial load of 20 kN. Least squares regression method has been employed to analyze the sound velocity and the Schmidt hammer test results. For each regression, best-fit line equation, 95% confidence limits, and the correlation coefficient (r) have also been determined. The test results exhibited that inverse linear relation exists between the number of joints and the P-wave velocities i.e., P-wave velocity decreases with an increase in the number of joints. Also, slopes of the regression lines were described as the sound velocity index (SVI), which exhibits that a linear relationship exists between the SVI values and the rebound numbers. High strength rocks exhibit higher SVI as compared to the low strength rocks.

Kahraman (2002) has investigated the P-wave velocity of intact rock by correlating the direct P-wave velocity value and the indirect P-wave velocity values obtained from laboratory measurements. In this study, measurements have been made on eleven rock specimens collected from the marble and granite factories in the Konya, Antalya and Kayseri areas of Turkey. Three of these specimens were igneous, six were sedimentary and two were metamorphic and are $200\text{ mm} \times 300\text{ mm} \times 200\text{ mm}$ in size. The rocks blocks have been diamond-sawed and subjected to an axial load of 20 kN. P-wave velocities have been measured by employing E48 pulse generator unit (make, Controls) and two

transducers (transmitter and a receiver) having a frequency of 54 kHz in three perpendicular directions repeatedly and the average values were recorded. The results of the sound velocity tests have been analyzed by using the method of least-squares regression and equation of the best-fit line. 95% confidence limits, and the correlation coefficients (r) have been determined for each regression. These results exhibited a linear relationship between the direct P-wave velocity and both the semi-direct and the indirect P-wave velocities. The correlation coefficients have been found to be quite high, which has indicated the utility of the variables for engineering usage.

Kahraman et al. (2008) have investigated the depth of fractures in a rock block by conducting P-wave velocity measurements in the laboratory. Investigations were carried out on the rocks collected from stone processing plants, quarries and natural outcrops in Nigde, Kayseri and Konya area of Turkey. The rock block dimensions are 250 mm \times 150 mm \times 200 mm. Standard tests such as Density, Porosity, Uniaxial compressive strength and Brazilian tensile strength were performed on each of the rock types, and their physical and mechanical properties were determined. Ultrasonic tests were conducted on blocks with a progressively deepened cut, on nine different rocks with polished surfaces and then a fracture (measuring 10 mm in depth and of 5 mm aperture) parallel to the measuring direction was artificially created. The fracture depth was gradually increased from 10 mm to 80 mm at 10 mm increments, and the P-wave velocity measurements were conducted. A distance of 150 mm between the transducers was maintained in all tests. In this study, the E48 Pulse Generator unit made by Controls Company (Nigde, Turkey) and two transducers (a transmitter and a receiver, which work at a frequency of 54 kHz) were used for sound velocity measurements. The P-wave velocities were correlated with the fracture depth for each rock type; an inverse linear relationship was found. The slope of the regression lines was approximately same for one rock class and varied for the different material types viz., igneous and metamorphic rocks have the highest (average 131.44) and lowest slope (average 21.77) respectively. Some poor non-linear relationship has been observed between the slope and the rock density and between the slope and the porosity but no correlation has been proposed with the mechanical properties of rocks. The study highlights the fact that the depth of a cut fracture can be estimated from the P-wave velocity.

3.5 Roughness measurement of the fracture surfaces

Roughness of any surface can be defined by the geometric properties of a surface through a quantitative parameter describing the intuitive notions of “rough” or “smooth”

(Cord et al., 2007). Characterization of geometric properties of roughness of the fracture surface and aperture, statistics of the asperity height and of the joint aperture are important (Lanaro, 2000). Roughness measurements by employing 3D laser profile scanner can be used to capture the texture of fracture surface profiles or the topography of the surfaces using the laser beam and the co-ordinates of the scanned surface were in general in ASCII or binary files in the X, Y and Z format. X, Y and Z coordinates represents the width, length and asperity height of the fracture surface respectively. Statistical analysis can be performed to generate classical statistical parameters, mean, median, mode, skewness, kurtosis, standard deviation, etc., on the data generated from the 3D laser topographical inspection scanner. Several researchers have used root means square, (RMS) roughness, R_q and Roughness average, R_a to detect the variation on the fracture surface roughness.

R_q is a mathematical representation of the asperities height and depth of the fracture surface, and is defined as average between the asperity height deviations and the mean of the line/surface, taken over the entire surface. R_a is the mean height as calculated over the entire surface. R_q and R_a were computed by employing the Eq.3.2 and Eq. 3.3 respectively (Mellott et al., 2001, Guerrero et al., 2002, Vasconcelos et al., 2006).

$$R_q = \sqrt{\frac{1}{n} \sum_{i=1}^n (Z_i - \bar{Z})^2} \quad (3.2)$$

$$R_a = \frac{1}{n} \sum_{i=1}^n |Z_i - \bar{Z}| \quad (3.3)$$

where, n is the number of data points, and Z is the asperity height.

The above mentioned parameters are scale dependent and their magnitude differs for the same surface, depending on the measurement done, such as, with a profilometer (scale from mm to cm) or with an atomic force microscope (scale from \AA to mm) (Guerrero et al., 2002), the parameters R_q and R_a , helps in differentiating the surfaces of different topography quantitatively.

Rengers (1970) and Fecker and Rengers (1971) have offered an innovative method to measure statistical characteristics of joint roughness by choosing a reference line parallel to the common direction of the joint and then digitizing the profile at 1 mm intervals in discrete steps by recording the maximum positive and negative angles over the profile. Further, the step length has been progressively increased, and the tangents for the maximum positive and negative angles for each step size have been plotted. The maximum possible dilation occurs for any given relative shear movement can be represented as a hypothetical "free" dilation curve using this data and the method would be effective in addressing scale

effects of roughness. However, the methodology have been not incorporated any aspects of strength, and its value as a predictive tool has been limited to either hard rocks, (where slight surface degradation occurred at moderate stress levels), or to soft rocks with very low stress levels.

Williams (1980) has worked on rock socketed piles. In this study, the roughness of wall sockets has been sampled and the socket profiles as a set of statistics of roughness angles and heights for 2 mm step lengths has been measured.

Haberfield and Johnston (1994) have adopted a similar procedure in their model of joint behavior by keeping a roughness profile obtained from a typical joint cross-section. In this study, the joint profile, has been shown as a dashed line could be idealized as the series of straight lines or chords. Authors have noted that such a typical joint profile was one of an infinite number of cross-sections of the same joint surface and other joint cross-section would result in different straight line profiles. Researchers have suggested that each idealized profile could be analyzed (independently or collectively) on a statistical basis to obtain different roughness parameters viz., the mean and standard deviation of the chord absolute inclinations, and the mean and standard deviation of chord end-point and absolute heights.

Apart from the work relating surface parameters to friction in the field of tribology and wear theory, e.g. Koura and Omar (1981), many other investigators (Krahn and Morgenstern, 1979; Williams, 1980; Tse and Cruden, 1979; Reeves, 1985) have specifically attempted to correlate surface roughness with the frictional behavior of rock joints by statistical methods. The statistical parameters can be divided into two categories (Reeves, 1985):

- i. those describing the magnitude of roughness; such as, the center-line roughness and root mean square roughness;
- ii. those describing the texture of the rough surfaces, namely the root mean squares of the first and second derivatives of the surface profile, auto-correlation function, spectral density function, mean square value and structure function.

3.6 Critical appraisal

A comprehensive review of the literature presents investigations on permeability of fractured rock taking into account, the influence of axial load, confining pressure (Gangi, 1978; Gowd and Rummel, 1980; Walsh, 1981) and pore pressure (Walsh, 1981; Li et al., 1997). Many theoretical or experimental investigations indicate that the decrease in

permeability at relatively low pressure is caused by the closure of open cracks and therefore follows preferred flow paths of the fluid (Gangi, 1978; Jones, 1975). Also, improved models for fluid calculation have been proposed and practical measures to control fluid in-rush have been developed (e.g. Jones, 1975; Somerton et al., 1975; Bear et al., 1993; Zhang et al., 1997; Rutqvist et al., 2005; Zhu and Wong, 1997). Many progresses have been made in the study of rock mass behavior over the past three decades; however, most of these methods are noticed to be tedious and time consuming or are found to exhibit logistical difficulties. Also, several empirical approaches (Brace et al., 1968; Jones, 1975; Somerton et al., 1975; Goodman, 1976; Witherspoon and Gale, 1977; Pratt et al., 1977; Brace, 1978; Walsh, 1981; Bandis et al., 1983; Raven and Gale, 1985; Zhu and Wong, 1997; Zisser and Nover, 2009) and analytical solutions (Indraratna, et al., 2003; Hugh, et al., 2004) have been developed and adopted by the researchers for investigating the permeability of fractured rocks. However, most of these researchers have either used numerical simulation or complicated test setups to study the behavior of fluid flow through the rockmass, which are either test-specific or rock specific and hence do not yield any generalized relationship. Major problem with existing methods is that they do not identify the influence of fracture network within a large rock mass.

Further, permeability of each rock type is conditional to its formation, tectonic activities and heterogeneities involved and hence behaves differently. Therefore, still there is a need to study or investigate further in detail, the simultaneous effect of various parameters on the permeability of fractured rockmass and come up with some generalized model. Many progresses have been made over the past three decades to study the behavior of permeability as a function of stress, and several empirical approaches (Brace et al., 1968; Somerton et al., 1975; Jones and Owens, 1980) have been developed for investigating the permeability of fractured rocks. Major problem with existing methods is that they do not identify the influence of fracture network or in particular 'single fracture' within a large rockmass. In addition, the critical issue of scale effects, such as how to relate properties measured in the laboratory to rock mass properties at the field scale, has not been rigorously studied. In addition, most of these methods are noticed to be tedious and time consuming or are found to exhibit logistical difficulties.

Hence, it is essential to investigate (a) the influence of state of stresses on the permeability of fractured rock mass (b) identify the influence of fracture network within a large rock mass and simulate the in-situ/field stress condition in the laboratory to study the fluid-rock interaction.

4.1 General

In this chapter, details of the experiments conducted on different types of materials (both analogue and natural) are presented. The methodologies adopted for determining the permeability of fractured rock mass have been discussed in details.

4.2 Selection of material

For the simplicity and understanding the basic interdependency of various parameters on permeability of the fractured- rock mass, the 'Paraffin wax' was selected as an analogue material. Further, collection of undisturbed rock samples from the deep locations and creation of the fracture(s) are quite cumbersome.

4.2.1 Analogue material - 'Paraffin wax'

Samples were prepared with the help of molten wax, to emulate the rockmass, which allows flow of water through the fractures, primarily, and not through the matrix. Apart from the ease of sample preparation and ensuring the homogeneity of the sample, it also facilitates creation of a single fracture with well-defined geometrical shape and aperture of the fracture. The methodology to create a cylindrical samples and fracture of certain apertures in the sample, are discussed in the following.

4.2.1.1 Sample preparation

Cylindrical samples made of Paraffin wax, imbuing a 'single fracture' were prepared for simulating flow characteristics of water as described in the following. The molten wax was poured into the cylindrical mould (38 mm in diameter and 76 mm in length, as depicted in Fig. 4-1a. This mould consists of a circular base plate, two cylindrical halves, and an aluminum rectangular plate of 1 mm thickness. The two halves were joined together with "screw arrangement" by keeping the aluminum plate in between the two cylindrical halves. After that the molten wax was poured into the mould and it was allowed to solidify at the room temperature. Before pouring the wax in the mould, both the ends of cylindrical halves were lubricated with the help of silicon grease. This facilitates easy removal of the sample from the mould. In this way, two cylindrical halves of the wax sample were prepared.

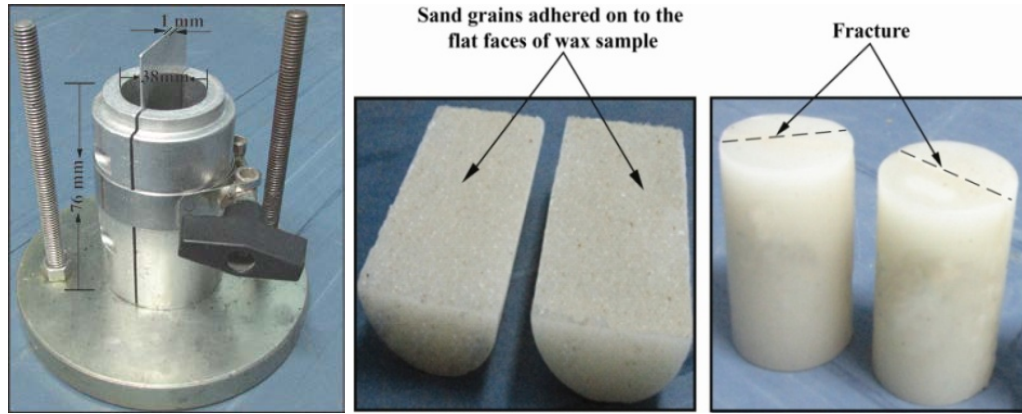


Fig. 4-1 The mould used for preparing the cylindrical samples, (b) cylindrical halves of the sample with adhered sand and (c) the sample with a single fracture

4.2.1.2 Creation of 'single fracture' in the analogue material

For creating a single fracture, of certain aperture, (e), in the sample, standard sand grains and glass beads were used in an interesting manner. The sand grains were passed through 500 μm , 600 μm and 850 μm sieves and were retained on 425 μm , 500 μm , and 710 μm sieves, respectively. The four different sizes of glass beads were selected, having diameters as, 0.45 mm, 1.00 mm, 1.42 mm and 1.85 mm. By using these sand grains, and glass beads, different fracture apertures were created as described in the following. These samples were designated as S-SG-425, S-SG-500, and S-SG-710, and S-GB-0.45, S-GB-1.00, S-GB-1.42 and S-GB-1.85, where, S stands for sample, SG and GB, sand grain and glass beads and numerals, size of the grains, respectively.

In order to create a fracture of certain aperture, the sand fractions or glass beads were heated up to 50 $^{\circ}\text{C}$ and the flat faces of the cylindrical halves were lightly pressed on them. This facilitates adhering of the sand grains or glass beads onto the both cylindrical halves, as depicted in Fig. 4-1(b). These halves when joined together yield a sample with a single fracture having certain fracture aperture, as depicted in Fig. 4-1(c). Several identical samples were prepared, following this methodology, and their designation and details are listed in Appendix A. This Appendix also presents geometrical details of the sample and the fracture such as: the sample length, l ($=60$ mm), its initial diameter without sand grains, d_i , the final diameter with sand grains, d_f , initial aperture of the fracture, e_i ($=d_f-d_i$), the width of the fracture, W ($=34.5$ mm), and the initial area of the fracture, A_{fi} ($=e_i \cdot W$). These dimensions were measured by employing a digital Vernier Caliper with a least count of 0.01 mm. Particle morphology of the sands was determined with an intention to determine the average particle sizes so as to develop a model which substantiates the assumed value of e , and the details are presented in the subsequent heading.

4.2.1.3 Particle Morphology of the Standard Sand Grains

Particle morphology of the standard sand grains has been studied using an optical microscope and the micro-photographs of the samples are depicted in Fig. 4-2. As suggested by Robinson, and Friedman, 2002, it has been assumed that the optical micro-photograph yields the maximum cross sectional area of the grain.

For the sake of completeness, the procedure adopted for determining sphericity, S , roundness, R , regularity, ξ , and elongation index, EI , of a single grain of the sand sample, S-SG-425, by employing Adobe Illustrator CS2, Ver. 12.0.0, is depicted in Fig. 4-3.

As depicted in Fig. 4-3(a), maximum/largest inscribed circle $d_{\max\text{-in}}$ ($= 0.568$ mm) and the minimum/smallest circumscribed circle $d_{\min\text{-cir}}$, ($= 0.934$ mm) were constructed and S , was computed by using the Eq. 4.1 (Wadell, 1935; Riley, 1941; Robinson and Friedman, 2002; Patel et al., 2009).

$$S = \sqrt{\frac{d_{\max\text{-in}}}{d_{\min\text{-cir}}}} \quad (4.1)$$

R is the average radius of the curvature of corners of the particle with respect to the radius of the maximum inscribed circle (Wadell, 1935; Patel et al., 2009) and is determined by plotting several circles for several surface curvatures, and by employing Eq. 4.2,

$$R = \frac{\sum_{i=1}^N r_i / N}{r_{\max\text{-in}}} \quad (4.2)$$

where r_i is the radius of curvatures of the convex corners of the grain boundary and N is the number of the inscribed circles.

ξ is the average of S and R , and hence can be determined by employing Eq. 4.3,

$$\xi = (R+S)/2 \quad (4.3)$$

The elongation index, EI , of these sands was also determined (Fig. 4-3b), which defines the relationship between the two principal axes of the particle in a two-dimensional image and is the ratio between the intermediate, l_2 , and the major, l_1 , axes of the particle (Krumbein and Pettijohn, 1938).

The above procedures were repeated for 30 grains of each sand fractions and the average of S , R , and ξ , were obtained (refer Table 4-1). In addition, EI was determined and the details are listed in Table 4-2, which also presents the standard deviation, SD .

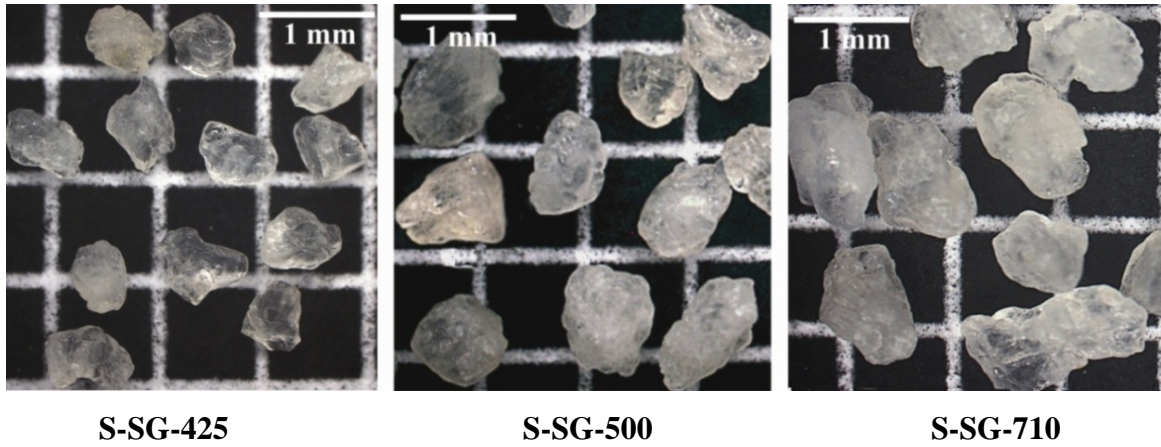


Fig. 4-2 Optical micro-photographs of the standard sands (×10)

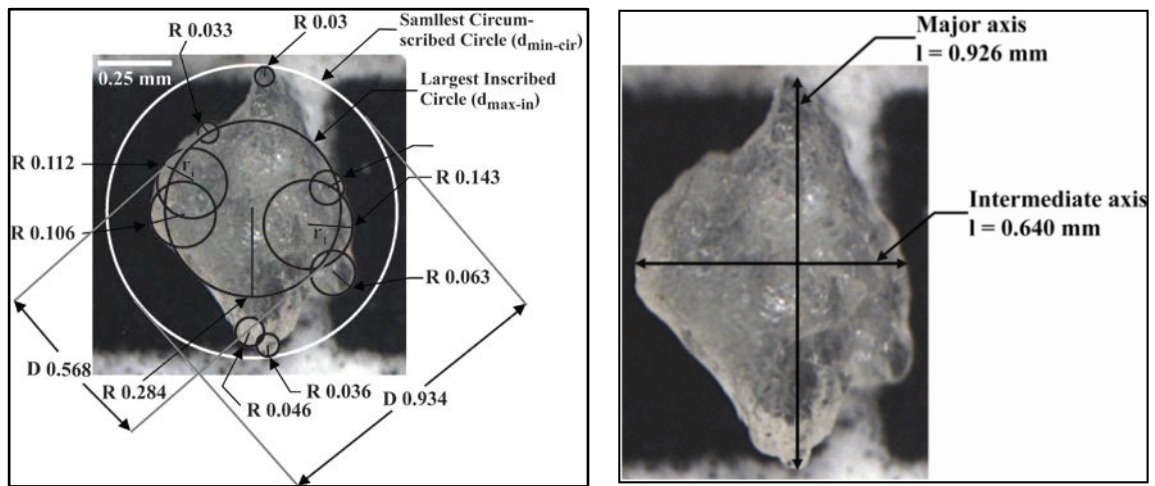


Fig. 4-3 Method to determine the (a) particle morphology (b) Elongation Index, using software AutoCAD, v. 2009 software

Table 4-1 Particle morphology of the samples of sand grains

Sample	S	R	ξ
S-SG-425	0.820	0.3260	0.573
S-SG-500	0.809	0.3264	0.568
S-SG-710	0.792	0.3034	0.548

Table 4-2 The elongation index of the samples of sands

Sample	l_1 (mm)		EI			SD
	Max.	Min.	Max.	Min.	Average	
S-SG-425	0.94	0.63	0.98	0.53	0.77	0.10
S-SG-500	1.41	0.74	0.97	0.45	0.75	0.15
S-SG-710	1.73	0.90	0.96	0.44	0.71	0.12

Perfect spherical standard glass beads were purchased based on their grain size. 30 grains of each glass beads, were selected randomly and diameter of the glass beads were measured by using a Vernier Caliper and accordingly four different types of glass beads based on their diameter were selected as depicted in Appendix B.

4.2.2 Natural Material - 'Hard/crystalline rock'

In this study, granite rock was collected under in situ conditions from in and around Melbourne, Victoria, Australia (Fig. 4-4). Based on visual identification of the grains, three different types of rocks of granitic composition were selected. These rocks were brought to the laboratory in the form of irregular blocks (≈ 300 mm in length, 200 mm in width and 150 mm in height). These blocks were set into the rectangular wooden boxes (slightly larger than the rock block) and white cement slurry was poured, as depicted in Fig. 4-5. This facilitates a proper sitting of the block in the wooden box and subsequent coring of the samples for testing. It was ensured that the flat surface of the rock block is facing upwards, which helps in smooth coring of the cylindrical samples from each of the rock blocks. The shallow and deep levels were marked on the top portion of the rock blocks so that the proper required length of the cores can be obtained.

To obtain the cores, a diamond core driller (120 Diamond Core System) was employed. Several cylindrical rock cores were retrieved. These cores were 38 mm and 54 mm in diameter, and 76 mm and 108 mm in length. The cores were designated as S1-CG-38, S2-MG-38, S3-FG-38 and S1-CG-54, S2-MG-54, S3-FG-54, representing the sample number, grain size (CG- Coarse grain; MG- Medium grain; & FG- Fine grain) and sample diameter (38 mm and 54 mm), respectively.

The sample designation and their geometrical details are presented in the Table 4-3. Further, a single vertical fracture running all along the length of the core was created, as described in the following section.

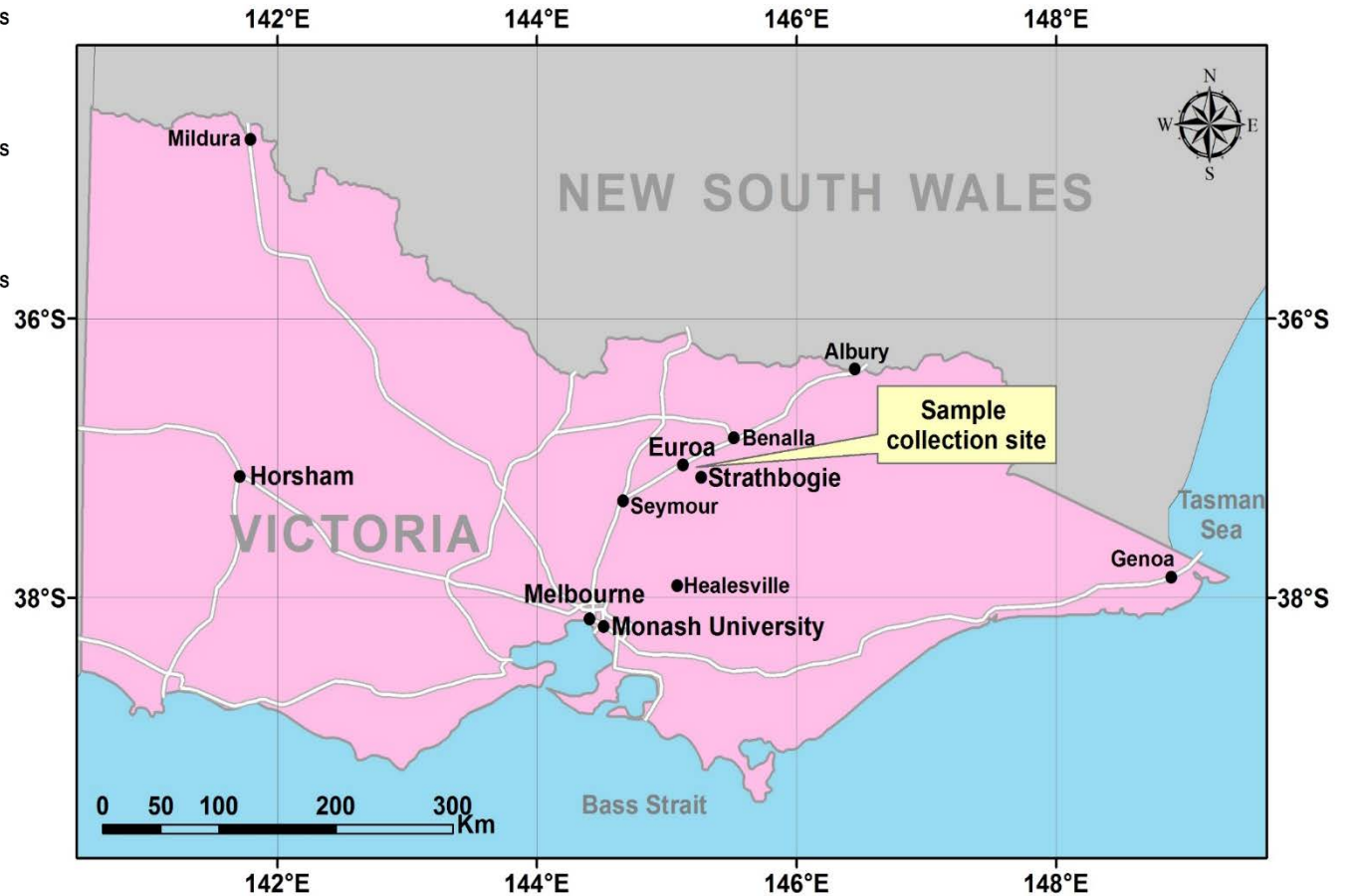
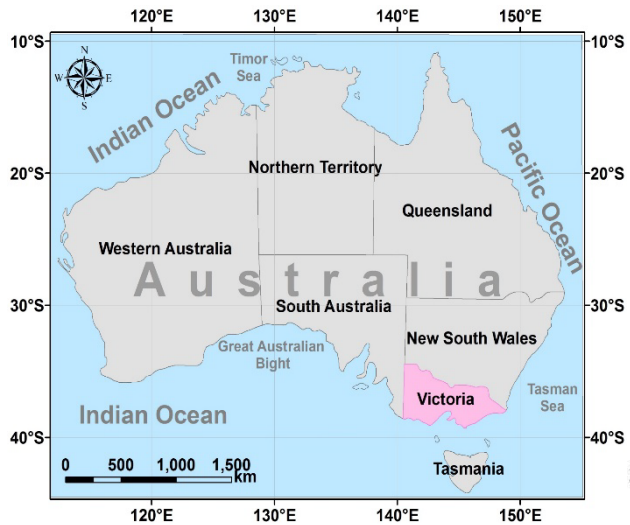


Fig. 4-4 Index Map of Victoria, Australia showing location of the granite rock sample collection site

Table 4-3 Engineering properties of the samples and their geometrical details

Sample No.	Rock type	$d(\text{mm})$	$l(\text{mm})$	$A_g(\text{mm}^2)$	$\sigma_c(\text{MPa})$	$E(\text{GPa})$	$P(\text{kN})$
S1-CG-38	Coarse Grained	39.7	76.2	152.4	150	42	25
S2-MG-38	Medium Grained	39.5	73.3	146.6	172	24	28
S3-FG-38	Fine Grained	39.6	74.6	149.2	249	77	35
S1-CG-54	Coarse Grained	53.8	106.94	213.88	126	35	22
S2-MG-54	Medium Grained	53.94	96.08	192.16	127	21	26
S3-FG-54	Fine Grained	53.83	99.92	199.84	181	62	30
S2-CG-54	Coarse Grained	53.9	97.3	194.61	124	33	23

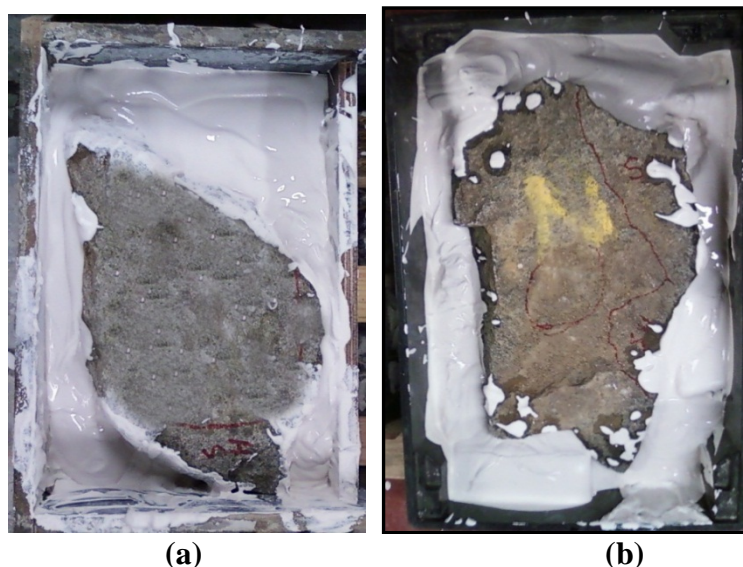


Fig. 4-5 The rock block placed in the rectangular boxes for coring (a) Fine grained granite and (b) medium grained granite

4.2.2.1 Creation of 'single fracture' in the natural material

To create a 'single fracture' in the rock core sample a setup made up of high carbon (1.20% C by weight) steel (refer Fig. 4-6) was fabricated. This setup consists of a pair of V-blocks and each of the V-block was placed on the flat metal plate. The setup consists of four holders to clutch the samples in the center of the V-block as depicted in Fig. 4-6(a). These V-block were fixed on the top and bottom platen of the Universal Compression Testing Machine, UCTM, respectively as shown in Fig. 4-6(d). To ensure the proper adjustment and alignment of the top and bottom V-blocks, both the top and bottom platen of the UCTM were brought close to each other and verified that the sharpen portion of top and bottom plate of the V-blocks were matching each other [refer Fig. 4-6 (c)]. After

ensuring the alignment of the V-blocks, the top platen of the UCTM was raised up and the sample was placed in between the V-blocks, positioning horizontal, so that the contact of the sharpen portion of the V-block occur along the sample length as depicted in Fig. 4-6(d). Before, placing the sample in between the V-blocks, 2 mm groove was made on two sides (at 180°) of the sample, whole along the length. The computed area of groove, A_g (mm²) for all the samples is mentioned in the Table 4-3. This facilitates, proper coupling of sharpen portion of the V-blocks and the sample with groove/contact area, mentioned in Table 4.3. Also, it allows equal distribution of the load throughout the sample length, which allows the sample to fail in tension, like Brazilian/point load test. Further, loading was applied perpendicular to the sample length, using the UCTM till failure [refer Fig. 4-6(d)] and details of the load, P at which the sample failed is listed in the Table 4-3 along with the engineering properties and geometrical details. In this way, the rock core separated into two cylindrical halves as depicted in Fig. 4-7(a). Then, both the cylindrical halves were joined together by means of silicon adhesive, as applied on both sides, along the length of the sample as depicted in Fig. 4-7(b).

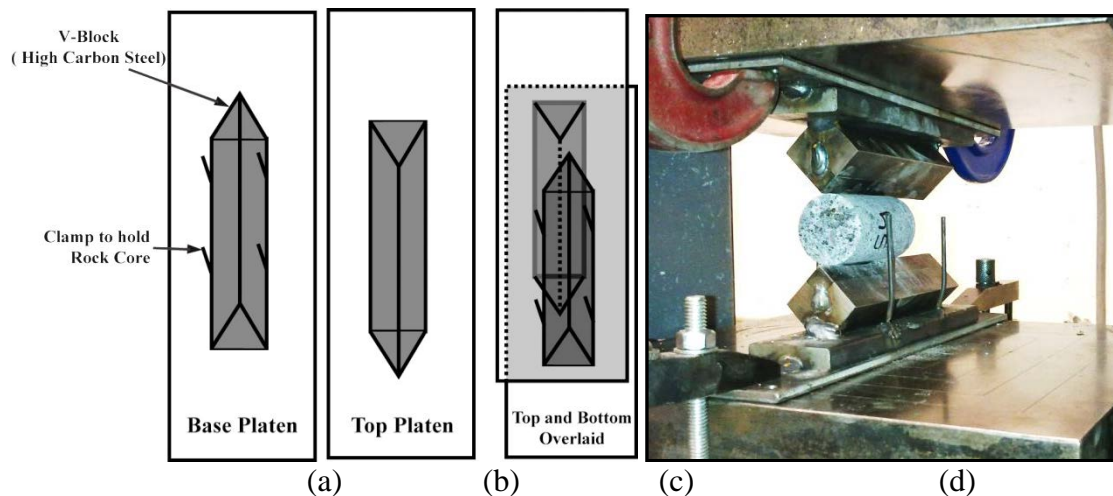


Fig. 4-6 V-Blocks setup to create a fracture in the rockmass, (a) Base Plate, (b) Top Plate, (c) both top and bottom plate placed over each other, (d) sample placed in between the top and bottom platen

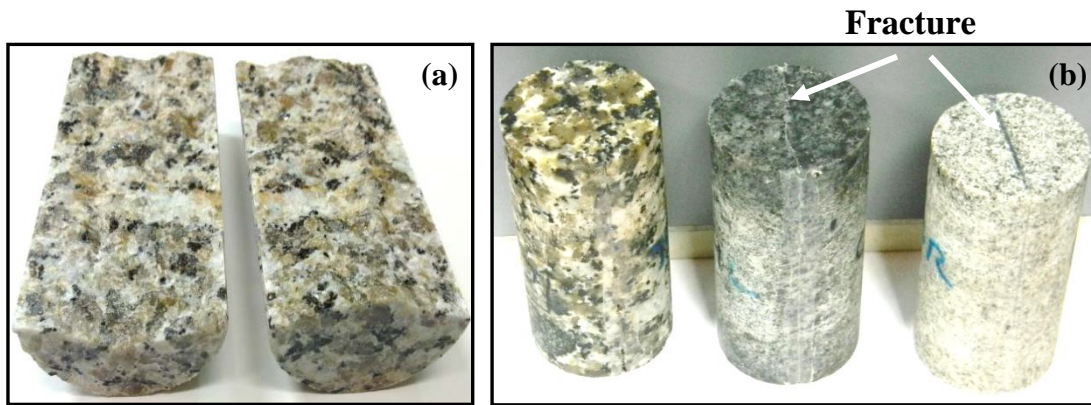


Fig. 4-7 (a) Cylindrical halves of the fractured granite sample, (b) samples with a single fracture

4.3 Testing methodology

4.3.1 Determination of Engineering Properties of Analogue material

The mechanical properties viz. uniaxial compressive strength (UCS) and load-deformation characteristics of wax specimen were determined by compression testing machine, Master Loader HM-3000, based on UCS testing procedure of cylindrical rock cores (ASTM D 4543-08). The test setup consists of UCS testing machine, load cell of 1000 kg capacity, and a sample cage made of three derlin rings, the connecting rods and 4 LVDTs, three in horizontal and one in vertical direction (refer Fig. 4-8 and Fig. 4-9). The middle ring can support three LVDTs (Linearly Variable Differential Transducers) at 120° apart, as depicted in Fig. 4-9. These LVDTs (type KL 17) work on the principle that when AC current (2 Vrms, 5 kHz sine-wave) is applied to primary winding, it produces a magnetic field which, in turn, induces emf-in two differentially connected, secondary windings. The magnetic core moving linearly along the axis varies the flux linkage from primary to both the secondary. The output voltage, thus obtained is linearly proportional to linear displacement. These LVDTs have rounded tips, which restrict their piercing into the sample, and can record deformations in the range 0 to 10 mm, with a least count of 1 μm. The cylindrical wax sample (height 76 mm and diameter 38 mm) was kept inside the, cage and load was applied by the machine. The LVDTs record strain in lateral direction, ϵ_{trans} of the sample, when it was axially loaded. For measuring strain in axial direction, ϵ_{axial} of the sample, another similar LVDT was employed. A 5-channel readout unit, which has a computer interface, was used for recording ϵ_{trans} , ϵ_{axial} and the applied load, P . Using these data the stress-deformation characteristics of the wax specimen can be established by following the steps as mentioned below.

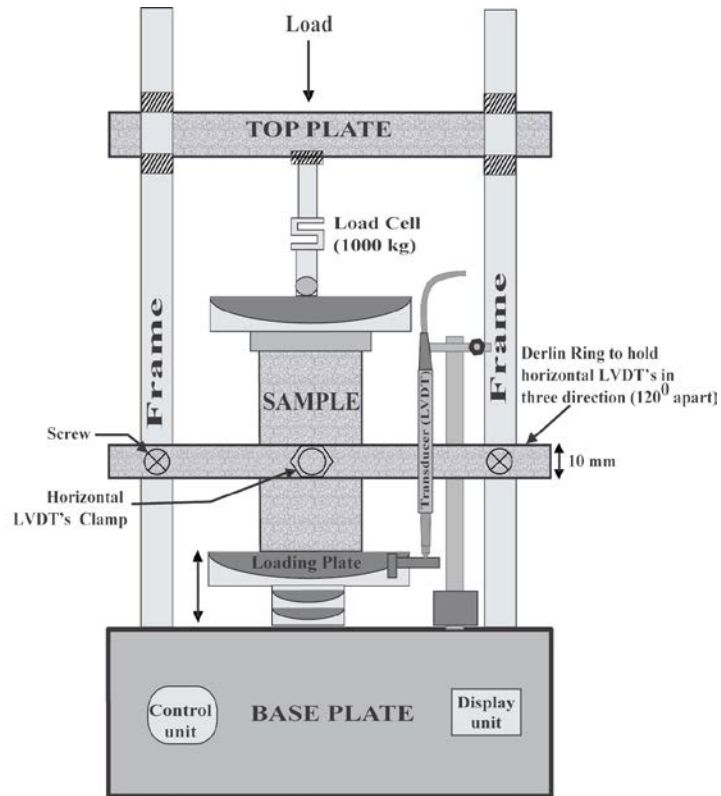


Fig. 4-8 A Master loader for determining the engineering properties of the analogue sample

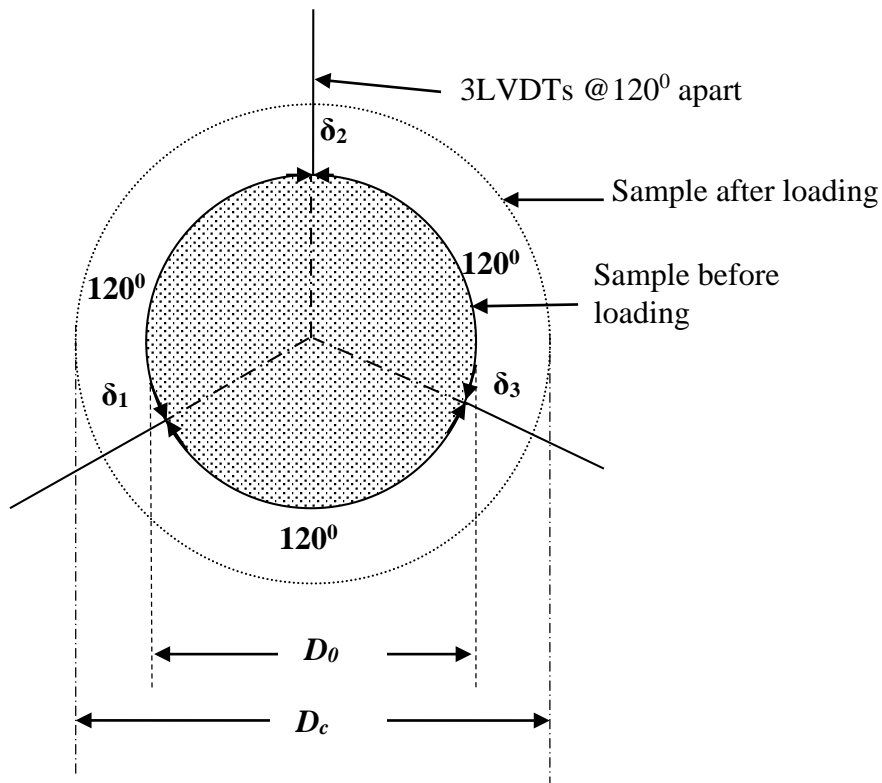


Fig. 4-9 Details of the positioning of LVDTs in the above setup (after Patel et. al., 2009)

If ε_1 , ε_2 and ε_3 are the strains recorded by the three LVDTs, then the lateral strain ε_{trans} can be presented as (Gere and Timoshenko, 1987):

$$\varepsilon_{trans} = \frac{\varepsilon_1 + \varepsilon_2 + \varepsilon_3}{3} + \frac{\sqrt{2}}{3} \cdot \sqrt{(\varepsilon_1 - \varepsilon_2)^2 + (\varepsilon_2 - \varepsilon_3)^2 + (\varepsilon_3 - \varepsilon_1)^2} \quad (4.4)$$

If ε_{axial} is the longitudinal strain then:

$$\nu = \frac{\varepsilon_{trans}}{\varepsilon_{axial}} \quad (4.5)$$

where ν is the Poisson's ratio by employing Eq. 4.5, for a particular stress ($=P/A_c$), where P is the axial load applied on the sample and A_c is the corrected area:

$$A_c = \pi \cdot \frac{(D_c)^2}{4} \quad (4.6)$$

where, D_c is the corrected diameter, after successive deformation in the sample (ref. Fig. 4.5): computed as follows:

$$D_c = D_o + \frac{2}{3}(\delta_1 + \delta_2 + \delta_3) \quad (4.7)$$

where, D_o is the initial diameter of the sample and δ_1 , δ_2 and δ_3 are the transverse deformation of the soil sample shown by the three LVDTs.

4.3.2 Determination of Engineering Properties of natural material

Engineering properties, (uniaxial compressive strength and young's modulus) of intact rock core samples were determined by employing UCTM as per the ISRM guidelines. Three samples of each grain size were tested for compressive strength, σ_c (MPa) and Young's modulus, E (in GPa) and their average values are listed in Table 4-3.

4.3.3 Fluid flow characteristics of Analogue Material using FWP

The main objective of this study is to simulate the flow characteristics of water through a 'single fracture' of different fracture apertures under incremental increase in confining stresses acting on a rockmass. The molten wax was used to emulate the rockmass, which allows flow through the fractures, primarily, and not through the matrix. Apart from the ease of sample preparation and ensuring the homogeneity of the sample, this methodology facilitates proper understanding of the basics of the flow of water through a 'single fracture' and the influence of various parameters on it.

4.3.3.1 The Test Setup

The FWP has been widely used in geotechnical engineering laboratories for determining the hydraulic conductivity of soils. Hence, in the present study, the same has been employed to determine the flow characteristics of the wax sample using the

methodology employed for saturated soils (as per ASTM D- 5084). The HM-4150 Flexpanel (make Humboldt, USA) which consists of a triaxial cell and three burettes (Cell, Base and Top) attached to a master control panel (Flexpanel) has been employed in the present study as depicted in Fig. 4-10(a) & (b). The schematic diagram of the test setup is depicted in Fig. 4-11. This FWP facilitates determination of the permeability of the geomaterials (ASTM D-5084). The major advantage of using the FWP is that due to the application of the confining stress, σ_3 , on the sample, the side-wall leakage that occurs in conventional permeameters can be eliminated (Samingan et al., 2003). The FWP also facilitates determination of the influence of σ_3 on flow characteristics of the sample with 'single fracture'.

The sample was mounted on the base plate in the cell. Two porous stones of the same diameter, as that of the sample, were boiled in demineralized water to ensure saturation. These stones along with filter paper were placed on the top and bottom of the sample. The high vacuum grease was applied between the porous stone and the top and bottom surfaces of the sample, and between the porous stone and the top and bottom base plates so as to reduce friction. The sample was covered with the latex membrane and with the help of O-rings, the membrane was fixed to the top and the bottom plates. The top tube was inserted into the holes provided in the top plate, the cell was closed and completely filled with the de-aired water. Later, the sample was saturated to achieve the complete saturation by applying the base pressure/injection pressure, b_p . After saturation, a constant b_p equal to 10 kPa was applied under σ_3 of 50 kPa. By collecting the amount of the water flowing from the base burette, h_1 , through the fracture, into the top burette, h_2 , as depicted in Fig. 4-11, the discharge, Q , was measured over a period of time, t . Both the burettes come with a 10cc volume with an accuracy of 0.02cc, and the area of the cross section of the burette is 0.263cm². Incidentally, Q (in cc) is equal to the average of the base outflow and the top burette inflow. Later, σ_3 was increased in steps of 50 kPa (up to 1200 kPa, which is the capacity of the FWP) and Q was measured for 15 minutes, corresponding to each σ_3 . For the sake of generality of the test results, several samples were tested with injection pressure, b_p equal to 10 kPa, 20 kPa, and 30 kPa and the results are discussed in the subsequent chapter.

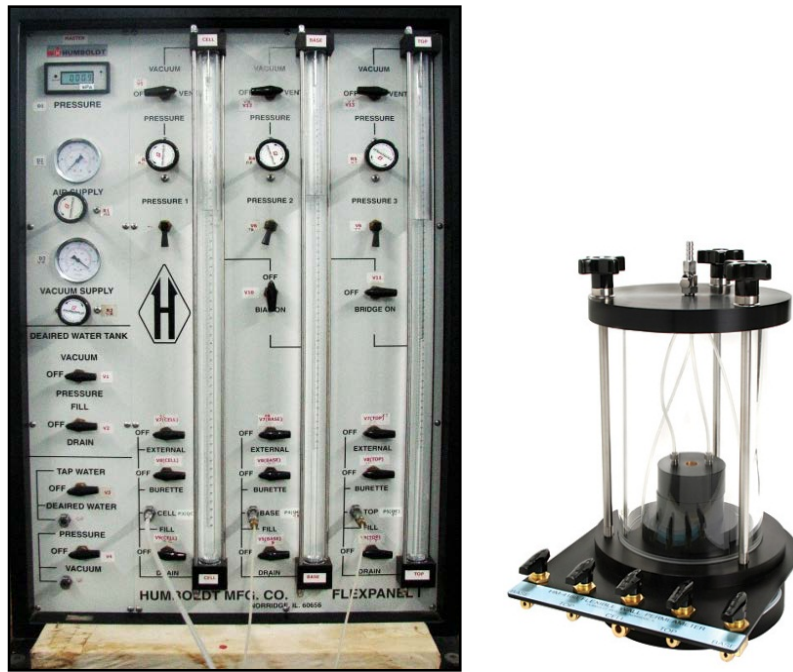


Fig. 4-10 The Humboldt Flexi-Panel HM-4150 permeameter for determination of permeability. a) The Master Control Panel, with the Cylindrical Sample Cell

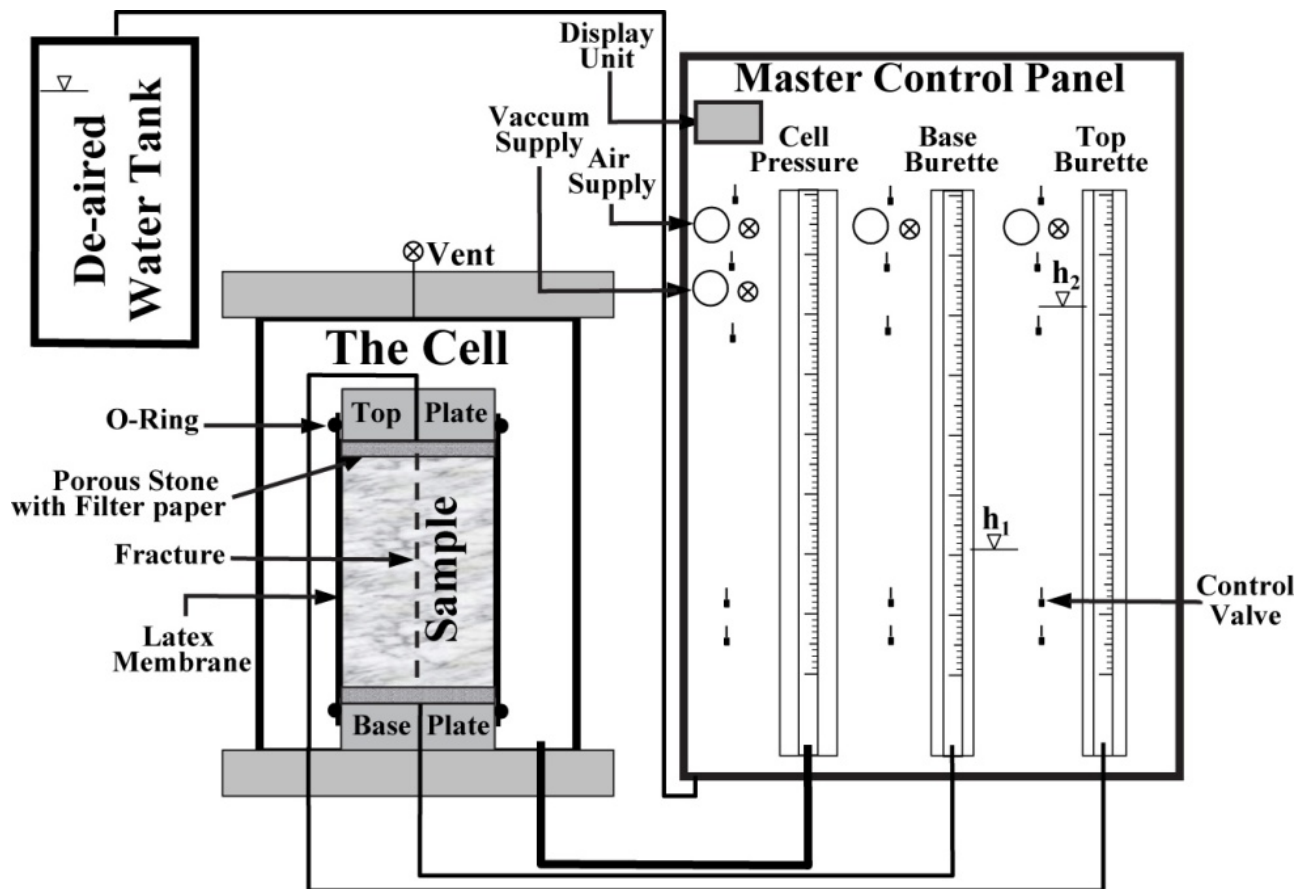


Fig. 4-11 The schematic diagram of the test setup (after Singh et al., 2014)

4.3.4 Roughness measurement of the fracture surface of the Natural Material

In the present work, roughness measurements were performed on the both the cylindrical halves/fracture surfaces, produced from direct tensile tests conducted on samples of granites at 0.04 mm point spacing before affixing together, by employing ROMER 3D laser profile absolute arm scanner, seven axis "SI" series, certified to B:89 specifications. The path of the scanning surface was performed manually by rotating the scanner 180° with respect to the vertical axis to avoid the problems of shadows and reflection from the Quartz grains and the measurements were collected automatically and the co-ordinates of the scanned surface were further discharged into ASCII or binary files. Statistical analysis was performed to generate classical statistical parameters, mean, median, mode, skewness, kurtosis, standard deviation, etc., on the data generated from the 3D laser topographical inspection scanner and the results are discussed in the Chapter 5. Root means square, (RMS) roughness, R_q and Roughness average, R_a were calculated over the entire surface, by employing the Eq. 3.2 and Eq. 3.3, respectively, as depicted in Fig. 4-12.

Although, these parameters are scale dependent and their magnitude will differ for the same surface; depending on the methodology of measurement adopted (viz., a profilometer, scale varies from mm to cm, or with an atomic force microscope, scale varies from A° to mm, Guerrero et al., 2002), they help in differentiating the surface quantitatively.

In the present study, samples are approximately of same dimension (refer Table 4-3) and scanning of the fracture surface was maintained as 0.1 mm (resolution). Data obtained from the 3D scanner (in X, Y, Z format) were exported to the SURFER v.10 to produce grid file. This was followed by developing the 3D surface profile of both the cylindrical halves/fracture surfaces. Further, by employing ArcGIS v.9.3, 2D roughness profiles for all the sample was generated and analyzed, by employing the data obtained from the 3D scanner, as discussed in Chapter 5.

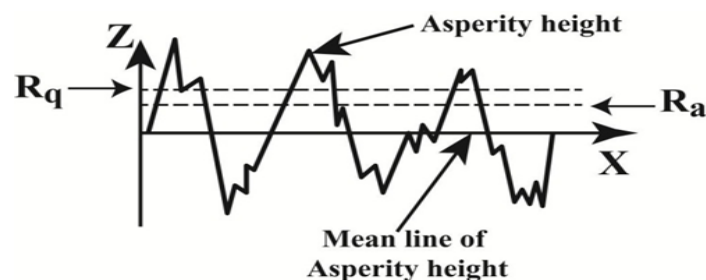


Fig. 4-12 The asperity profile and the statistical parameters associated with it

4.3.5 Fluid flow characteristics of Natural Material using HPTC

The fluid flow characteristics of granite sample imbibing a 'single fracture' were determined using high pressure triaxial cell, HPTC, as depicted in Fig. 4-13.

4.3.5.1 The Test Setup and Working Principle

The test setup consists of a loading system, loading frame, a triaxial cell compressor unit, hydraulic oil reservoir, high pressure hydraulic pump, and water pressure pump as depicted in Fig. 4-13. The schematic diagram of the experimental setup is depicted in Fig. 4-14. The tests setup also consists of a load cell of 150 ton capacity to measure the applied load and 1 LVDT in vertical direction to measure the axial deformation, ϵ_{axial} . To measure lateral deformation, ϵ_{trans} , a metal-foil strain gage was used.

The cylindrical sample with a single fracture was placed on the base pedestal and top cap was placed above the sample. Before keeping the sample on the base pedestal, two porous stones were also placed. Later, the sample was covered with a rubber membrane and two O-rings and horse-shoe clamps on each top cap and bottom pedestals were placed over the rubber membrane to avoid shot circuiting with the applied confining pressure, (σ_3) and the base pressure, (b_p). Hence, the test setup can be idealized creating a one dimensional, leak proof, flow conditions. A metal-foil strain gauge, was fixed over the rubber membrane to measure ϵ_{trans} , when confining pressure was applied. Then, the cell was closed and filled with hydraulic oil ensuring that the cell was free of the air.

Permeability tests were performed on the fractured specimens at different values of σ_3 (5, 10, 15, 20, 30 and 40 MPa). Hydraulic oil was used as the fluid media in the cell and σ_3 was applied using a hydraulic pump and its magnitude was recorded using a pressure transducer that carries a combined total error band of $\pm 0.75\%$ of the maximum measurement. Once the sample has been exposed to the target σ_3 , water was pumped from the high pressure water injection pump to the bottom of the sample and collected from an outlet hose connected to the top of the sample after 30 min. to 45 min after flow becomes stabilized. The magnitude of the inflow was recorded by an independent pressure transducer. The discharge, Q , was collected in an airtight container to avoid the water losses. The container was placed over a weighing balance of 1200 g capacity along with computer interface and Q , was recorded at 3 second interval. A 5-channel readout unit, which has a computer interface, was used for recording σ_3 , ϵ_{trans} , ϵ_{axial} and the applied/resistance load, P . The test was continued until the flow becomes stabilized, corresponding to each b_p and the time, t to stop the test was approximately 30 to 45 minutes, depending upon their stabilization time i.e., Q becomes constant with time, t . Tests were

carried out at different values σ_3 and b_p , as depicted in Table 4-4. There were 33 experiments in total for each sample and 600-1000 test points depending upon the stabilization time of the Q . After each experiment, sample was again exposed to the different target σ_3 . To ensure side wall leakage and to stabilize the fluctuation in target σ_3 , sample was exposed required σ_3 , for a period of 6-8 hours. In the same manner, several samples were tested and discussed in Chapter 5. The variation in Q with t corresponding to $\sigma_3=5\text{MPa}$ and $b_p (=1, 2, 3 \text{ and } 4 \text{ MPa})$, for sample S1-CG-38, has been plotted as depicted in Fig. 4-15. For the sake of brevity, a typical data sheet used for recording experimental observations and calculated parameters for natural sample, S1-CG-38 is listed in Appendix I.

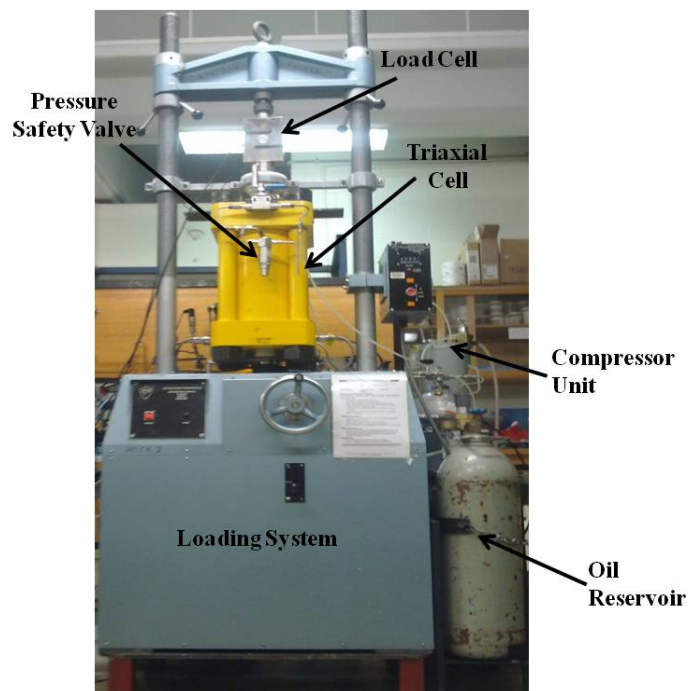


Fig. 4-13 The test setup used for determining the flow characteristics of water through the fractured rockmass

Table 4-4 Detail of fluid flow tests configuration

	σ_3 (MPa)					
	5	10	15	20	30	40
b_p (MPa)	1	1	2	2	2	2
	2	2	4	4	4	4
	3	4	6	8	8	8
	4	6	8	10	14	14
			8	10	14	18
			14	18	25	25

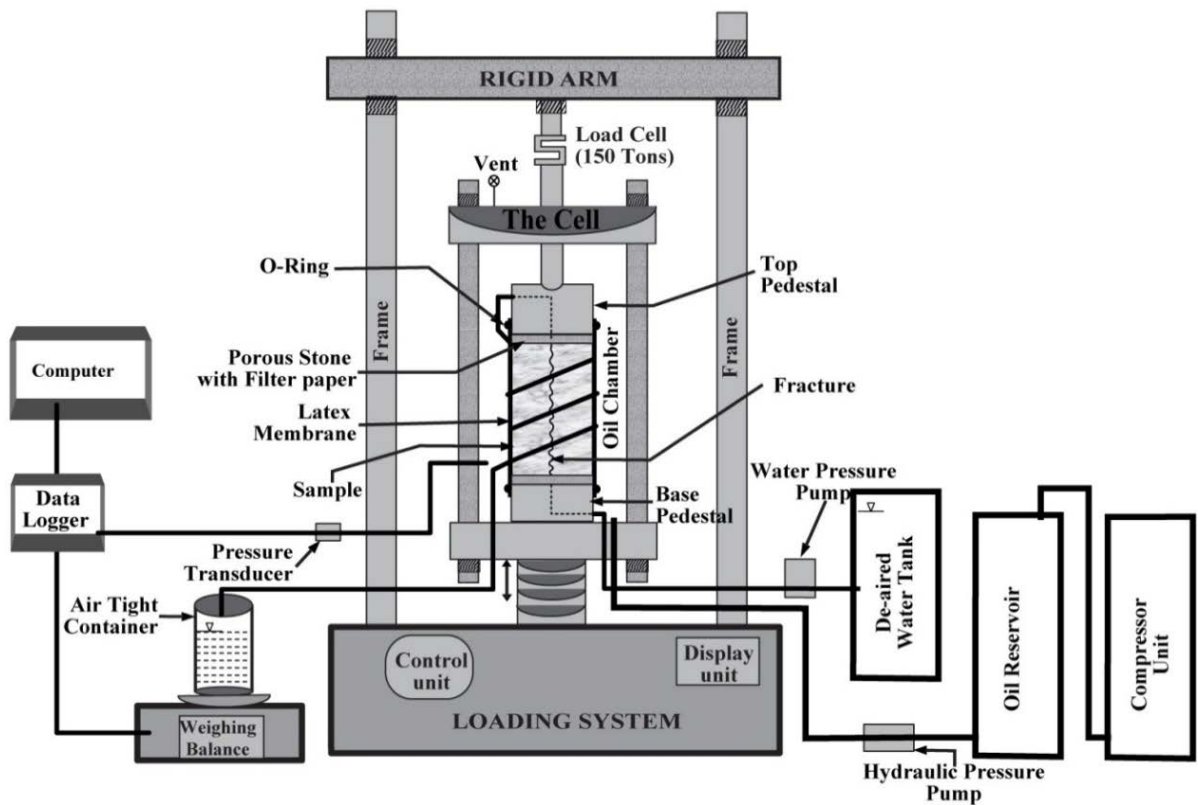


Fig. 4-14 The schematic diagram of the experimental setup used for determining flow characteristics of water through the fractured rock mass

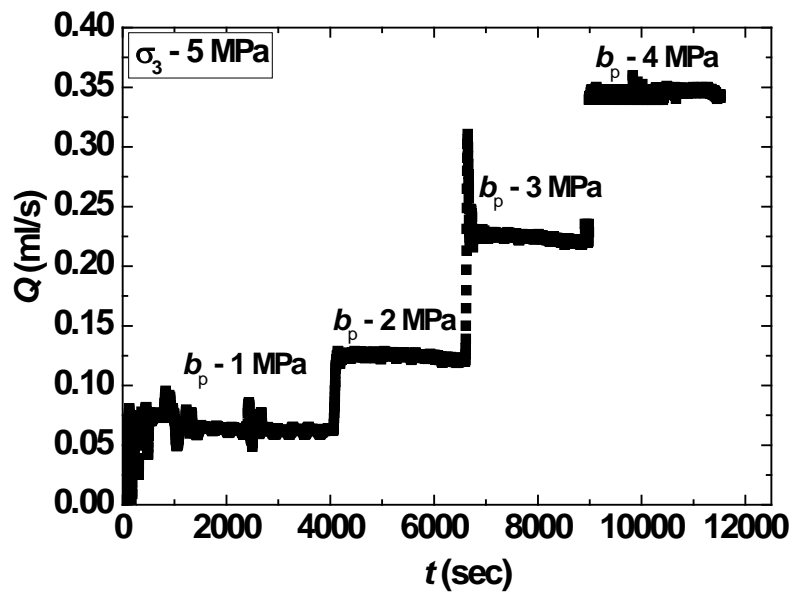


Fig. 4-15 The variation in Q with t for different values of b_p as obtained from fluid flow test

5.1 General

This chapter present the results obtained from the experimental investigation and has been analyzed and discussed in detail.

5.2 Particle Morphology of the Standard Sand Grains

It can be noted from the data presented in Table 4-2 that the sand grains used for creating a fracture of certain aperture, in this study, exhibit practically same EI . As, the initial fracture aperture, e_i , is dependent on the EI and the arrangement of the sand grains, at least three possible grain arrangements, refer Fig. 5-1, can be hypothesized. However, it should be noted that for the perfect spherical glass beads such analysis was not required. Further, it has been assumed that the sand grains and the glass beads glued on the surface of the wax are in regular pattern and the penetration is negligible. As per Fig. 5-1, one of the following relationships could be valid for defining the fracture aperture, e .

Computed fracture aperture, e_c using sand grains

$$e_c = 2 \cdot l_1 \quad (5.1 \text{ a})$$

$$= l_1 \cdot (1 + EI) \quad (5.1 \text{ b})$$

$$= 2 \cdot l_2 \quad (5.1 \text{ c})$$

Computed fracture aperture, e_c using glass beads

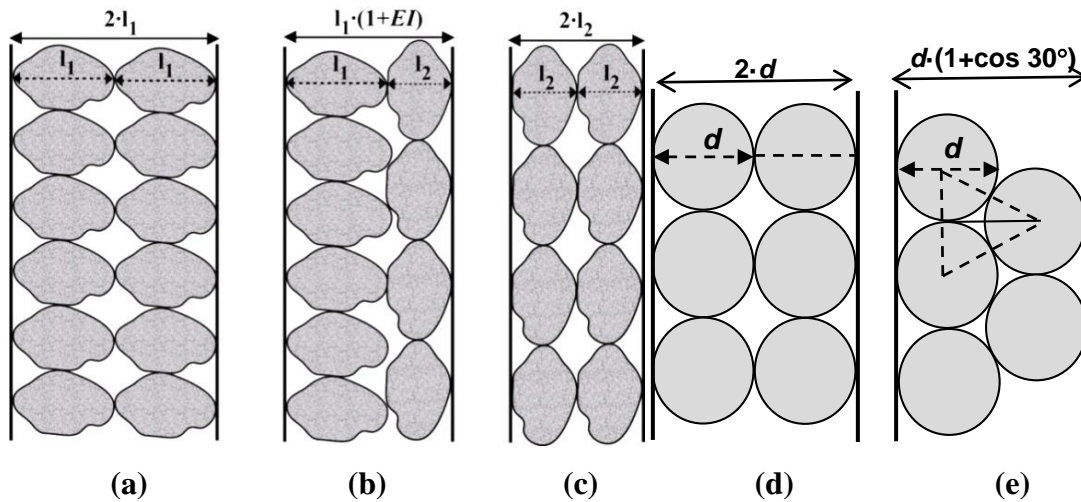
$$= 2 \cdot d \quad (5.1 \text{ d})$$

$$= d \cdot (1 + \cos 30^\circ) \quad (5.1 \text{ e})$$

where l_1 and l_2 are the major and intermediate axes of the particle, EI is the elongation index and d is the diameter of the grain.

The computed fracture aperture, denoted as e_c , of all the samples of sand grains, obtained by employing Equations (5.1 a), (5.1 b) and (5.1 c) is listed in Appendix C, Appendix D and Appendix E. Further, the average initial fracture aperture, $e_{cav.}$, were computed from the data presented in Appendix C, Appendix D and Appendix E for the samples S-SG-425, S-SG-500 and S-SG-710 is presented in Table 5-1. It can be observed from the data presented in the table that Equation 5.1(c) yields the value of e_c which is quite close to the initial fracture aperture, e_i , obtained by employing the Vernier caliper. This indicates that the most probable arrangement of the sand grains on the sample halves would be as depicted in Fig. 5-1(c). Further, e_c , obtained by employing Equations (5.1 d) and (5.1

e), and is listed in Appendix B. It can be observed from table that practically the e_c , computed by using Equation 5.1 (d) is quite close to the initial fracture aperture, e_i , obtained by employing the Vernier caliper. This indicates that the most probable arrangement of the glass beads on the sample halves would be as depicted in Fig. 5-1(d). However, the minor difference between e_c and e_i (obtained by using Vernier caliper) is due to small amount penetration of glass beads on the surface of the sample halves and is computed as about 5 to 13 % depending on the size of the glass beads, i.e., larger the glass beads, more the penetration.



Figs. 5-1 Typical arrangements of irregular sand grains (a-c) and perfect rounded glass beads (d-e) on sample halves

Table 5-1 Computed average initial fracture aperture, e_{cav} , of the samples of sand based on grain model equations

Sample	$2l_1$ (mm)			$l_1(1+EI)$ (mm)			$2l_2$ (mm)		
	Max.	Min.	Av.	Max.	Min.	Av.	Max.	Min.	Av.
S-SG-425	1.88	1.27	1.48	1.58	1.11	1.30	1.49	0.91	1.12
S-SG-500	2.81	1.48	2.05	2.11	1.44	1.78	1.80	1.04	1.50
S-SG-710	3.46	1.80	2.49	2.50	1.63	2.10	1.91	1.37	1.72

5.3 Engineering properties of the material

To know the material properties, the load-deformation tests was conducted on wax specimen and the relationship between stress and axial strain for one sample is depicted in Fig. 5-2. The UCS, which is the stress at failure of the wax, has been found to be 1260 kPa as depicted in the Fig. 5-2. The young's modulus, E , for the same obtained from the stress-strain plot, as depicted in Fig. 5-2 has been found to be 1010 MPa, and Poisson's ratio, ν , calculated by using Eq. 4.5 has been found to be 0.13.

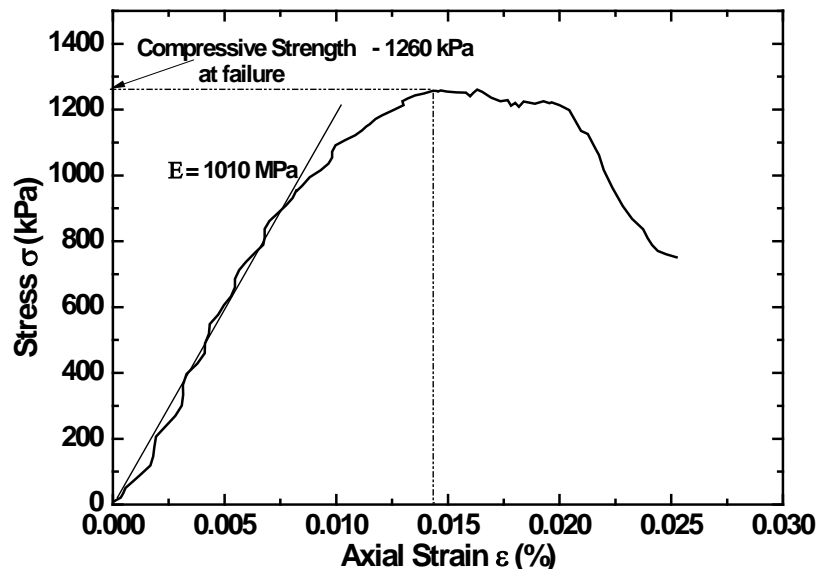


Fig. 5-2 The stress vs. strain relationship of the analogue material

5.4 Determination of Flow Characteristics of the Analogue Material

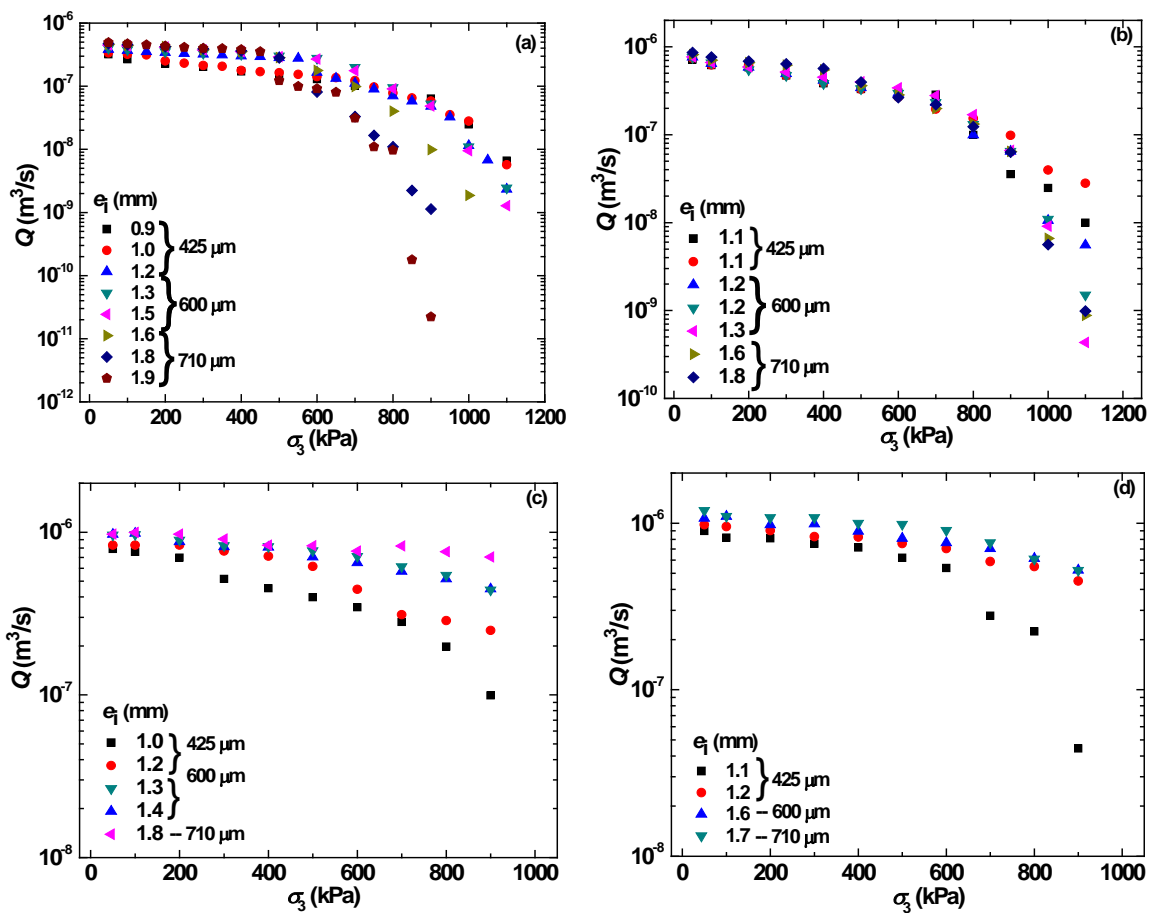
Data obtained from fluid flow tests of the analogue material have been further analyzed as discussed in the following. For the sake of brevity, a typical data sheet for recording the observation of fluid flow test of the sample S-SG-425 and S-GB-0.45 are listed in Appendix F and Appendix G. Fig. 5-3 depicts the variation of Q with σ_3 corresponding to b_p equal to 10, 20, 30 and 40 kPa, respectively, for various values of e_i . It can be observed from the trends depicted in the figure that, as expected, Q decreases with an increase in σ_3 in a non-linear manner. Incidentally, it can also be noted that for the samples with larger $e_i > 1.2$ mm, the influence of σ_3 over Q is much more pronounced as compared to their counterparts corresponding to $b_p \leq 20$ kPa. It can also be observed that in case of b_p equals to 10 kPa, for smaller $e_i \leq 1.2$ mm, Q decreases slowly with σ_3 , this indicates less further reduction in the fracture aperture, whereas, for $e_i > 1.2$ mm, corresponding to $\sigma_3 > 500$ kPa, Q decreases rapidly.

It must be noted here that due to the applied σ_3 , fracture with $e_i > 1.2$ mm, is more susceptible to closure than the fracture with $e_i \leq 1.2$ mm, corresponding to $b_p \leq 20$ kPa. On the contrary, for $b_p > 20$ kPa, [refer Fig. 5-3(c) and (d)], the influence of σ_3 on the e , and hence on Q is less, corresponding to $e_i > 1.2$ mm. These observations are consistent with the findings reported by earlier researchers (Witherspoon et al., 1980; Raven and Gale, 1985; Engelder and Scholz, 1987; Li et al., 1997). The rapid reduction in Q corresponding to $\sigma_3 > 500$ kPa for $e_i > 1.2$ mm [refer Fig. 5-3(a) and (b)] can be attributed, mainly, to an increase in grain-to-grain contact (which may also result in an increased tortuosity) and low values of b_p . It can also be noted that as expected, for $e_i > 1.2$ mm, the value of Q is higher than the cases when $e_i \leq 1.2$ mm, corresponding to all the values of b_p (refer Fig. 5-4). For a better appraisal of the influence of b_p on Q , the variation in Q with respect to σ_3 , corresponding to different values of b_p and for $e_i \leq 1.1$ mm and $e_i \geq 1.7$ mm, have been plotted as depicted in Fig. 5-4. It can be observed from these figures that Q is quite sensitive to both σ_3 and b_p . A closer look at Fig. 5-4(a), reveals that the influence of b_p is less prominent for $e_i \leq 1.1$ mm, and more changes in the Q occurs due to rapid change in fracture aperture (increase in grain-to-grain/asperities contact) and hence, at $\sigma_3 > 800$ kPa, Q corresponding to all b_p converges. On the contrary, Fig. 5-4(b), corresponding to $e_i \geq 1.7$ mm, influence of b_p is much more prominent and no significant change in the Q occurs. It can be attributed to the fact that fracture aperture opens up due to increase in b_p , and hence, Q corresponding to all b_p diverges even at $\sigma_3 > 800$ kPa.

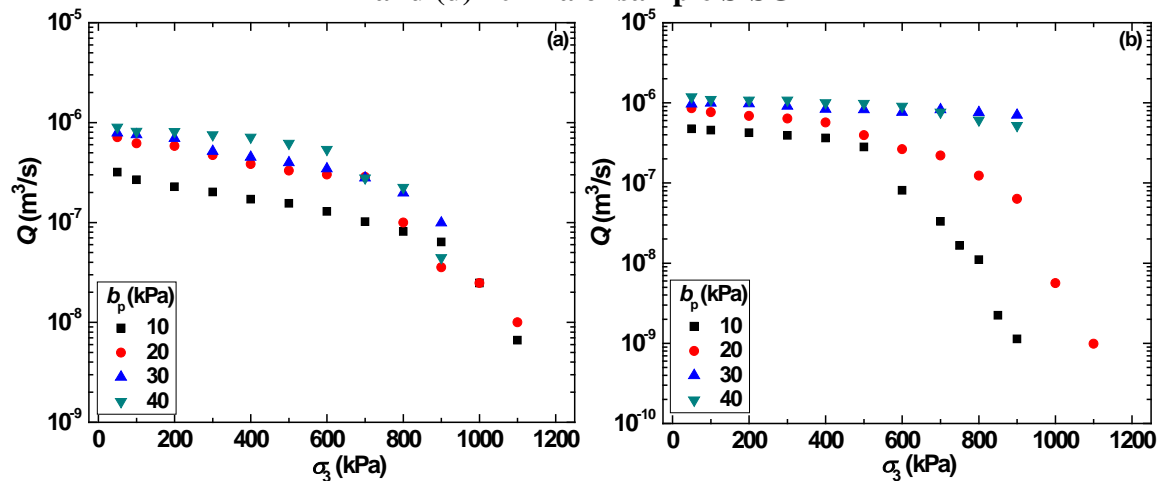
It can also be observed that the relationship between Q and σ_3 , for $e_i \geq 1.7$ mm, corresponding to $b_p \geq 30$ kPa, is almost linear as compared to the non-linear trend for $b_p \leq 20$ kPa. Further it can be noted that the influence of σ_3 over Q is much more pronounced for $b_p \leq 20$ kPa and $e_i \leq 1.1$ mm. Hence, it can be inferred that though Q is dependent on e_i , σ_3 and b_p , the initial fracture aperture, e_i , plays a much important role in governing the behavior of fluid flow through the fracture.

Fig. 5-5 (a) depicts the variation of Q with σ_3 corresponding to various values of e_i for b_p equal 10 kPa of samples S-GB. It should be noted that in sample S-GB, perfect spherical glass beads were adhered on the surface of the fracture instead of, irregular grains of sand. It can be observed from the Fig. 5-5(a) that as expected, Q decreases with an increase in σ_3 in a non-linear manner and Q is more for the larger initial $e_i (= 2.7\text{mm})$ and less for smaller initial $e_i (= 0.9\text{mm})$. Fig. 5-5 (b) depicts the variation of Q with σ_3 corresponding to various values of $b_p (= 10, 20, 30$ and 40 kPa) for initial $e_i (= 0.9\text{mm})$ of

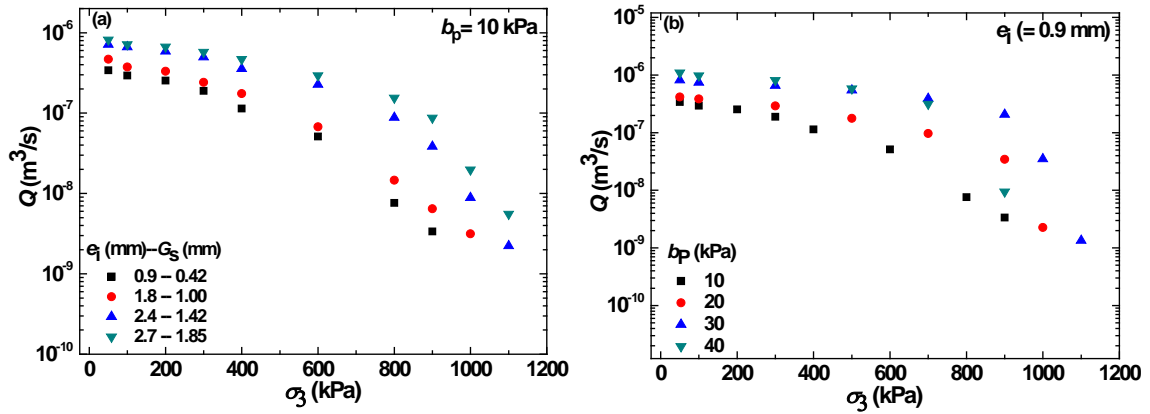
sample S-GB-0.45. It can be noticed from the Fig. 5.5 (b) that as expected, Q increases with an increase in b_p .



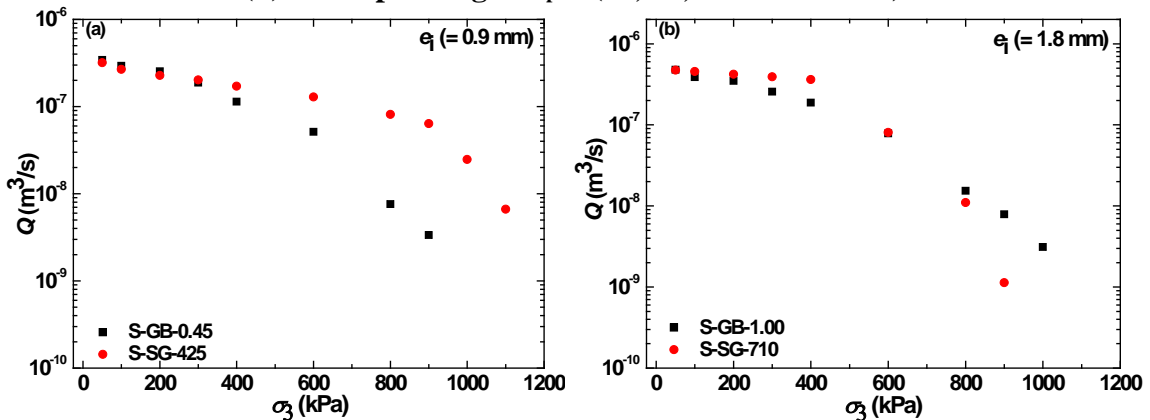
Figs. 5-3 The variation of Q with σ_3 for b_p equal to (a) 10 kPa, (b) 20 kPa, (c) 30 kPa, and (d) 40 kPa of sample S-SG



Figs. 5-4 The variation of Q with σ_3 at different values of b_p corresponding to e_i (a) ≤ 1.1 mm (425 μ m) and (b) ≥ 1.7 mm (710 μ m) of sample S-SG



Figs. 5-5 The variation of Q with σ_3 of sample S-GB (a) at different values of e_i and (b) corresponding to $b_p = (10, 20, 30$ and 40 kPa)



Figs. 5-6 The variation of Q with σ_3 corresponding to $e_i =$ (a) 0.9 mm, (b) 1.8 mm

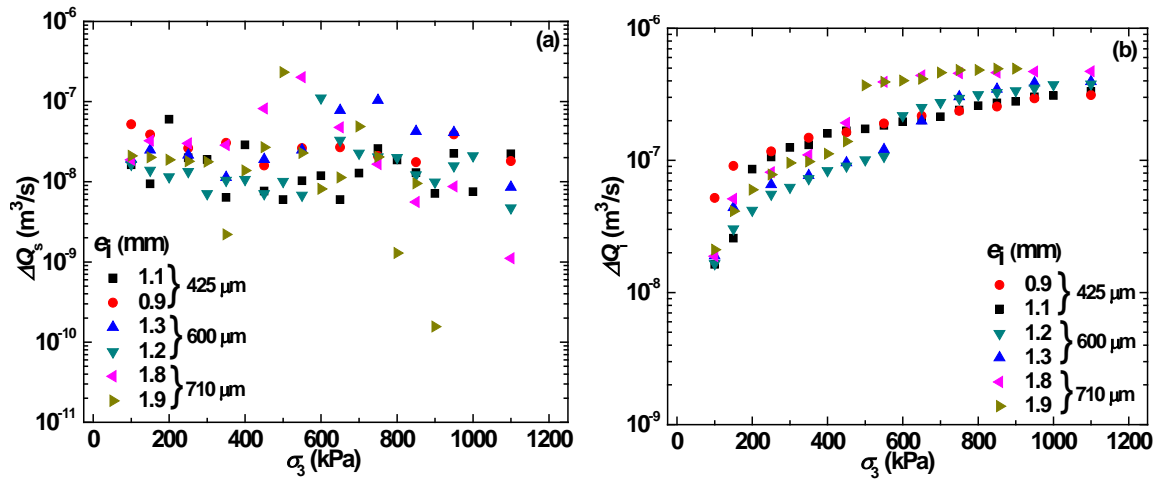
The variation in Q with σ_3 corresponding to $e_i (= 0.9$ mm and 1.8 mm) have been depicted in Figs. 5.6 (a) and (b) respectively. It can be observed from the Fig. 5-6 that Q decreases with an increase in σ_3 and shows a non-linear relationship. A closer look at the Fig. 5-6(a) reveals that before $\sigma_3 \leq 400$ kPa, Q decreases with σ_3 in almost similar manner for both the samples, S-GB-0.45 and S-SG-425. However, Q decreases rapidly with σ_3 for sample S-GB-0.45, as compare to sample S-SG-425, corresponding to $e_i = 0.9$ mm. It can be inferred that in case of sample S-SG-425, grains adhered on the fractured surface (asperities) are rough and irregular as compared to the sample S-GB-0.45, where asperities are quite spherical, well-rounded and smooth. Hence, closure of e is less even at higher $\sigma_3 \geq 600$ kPa, for sample S-SG-425, shows higher Q than the S-GB-0.45. It can be inferred from the Fig. 5.6 (b), corresponding to $e_i = 1.8$ mm that Q decreases with σ_3 and shows cross cutting behaviour. This can be attributed to the fact that as larger grains adhered on the surface of the fracture, it creates larger fracture aperture and hence Q vs. σ_3 relationship is almost similar for both the samples S-SG-425 and S-GB-0.45. There is significantly less effect on Q due to roughness or irregularity of asperities.

Further, the rate of change in flow has been computed from experimentally obtained data, based on the following two approaches: (1) Q at certain σ_3 subtracted from the Q obtained for the previous step of σ_3 and (2) Q at a certain σ_3 subtracted from the initial Q corresponding to $\sigma_3=50$ kPa, denoted as ΔQ_s and ΔQ_i , respectively, as listed in Table 4. The variations in ΔQ_s and ΔQ_i have been plotted as depicted in Fig. 5-7(a) and (b), corresponding to Approaches 1 and 2, respectively. It can be observed that Fig. 5-7(a) does not yield a proper trend, which indicates that Approach 1 should not be adopted. On the contrary, the trends obtained by employing Approach 2, depicted in Fig. 5-7(b), are quite in order and it can be observed that, in general, ΔQ_i versus σ_3 relationship initially shows increasing trend and then ΔQ_i becomes constant after $\sigma_3>800$ kPa, which indicates that with increase in σ_3 , the rate of change in flow decreases and the rate of change in flow ceases after $\sigma_3>800$ kPa corresponding to $b_p=10$ kPa. It can be attributed to closure of fracture aperture due to increase in σ_3 and at $\sigma_3>800$ kPa, fracture aperture has almost closed thus, no further change in rate of flow was observed. In this context, it is worth mentioning that though further increase in σ_3 , subsequent to closure of fracture aperture, could have induced deformation in the sample, even the maximum value of σ_3 (=1200 kPa), up to which the samples have been tested in this study, would not yield any significant deformations.

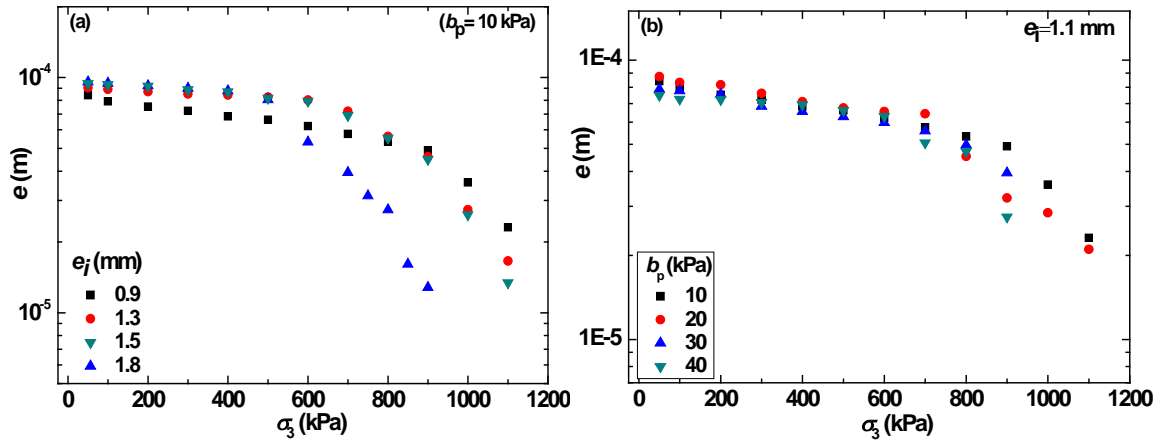
Hydraulic aperture, (e) has been back computed by employing equation Eq. 2.3 for all the samples of S-SG and the relationship between e and σ_3 , corresponding to $b_p=10$ kPa, for various values of e_i , has been plotted as depicted in Fig. 5-8(a). It can be observed from the Fig. 5-8(a) that e with σ_3 relationship is non-linear and as expected, is decreasing with an increase in σ_3 . It can also be observed that e corresponding to $e_i \geq 1.5$ mm, decreases rapidly after $\sigma_3 \geq 600$ kPa as compared to e of sample $e_i \leq 1.3$ mm. This can be attributed to the fact that asperities created due to presence of sand grains of samples $e_i \geq 1.5$ mm are larger (sand grains $\geq 600 \mu\text{m}$) and hence possibility of closure of e is more under the stress. Whereas, for sample of $e_i \leq 1.3$ mm, the possibility of closure of e is less due to the presence of small asperities (sand grain $< 425 \mu\text{m}$). Further, the relationship between e and σ_3 , corresponding to various values of b_p for $e_i=1.1$ mm is depicted in Fig. 5-8b. It can be observed from the figure that with an increase in b_p from 10 to 20 kPa, e increases upto $\sigma_3 \leq 700$ kPa and it decreases rapidly after $\sigma_3 \geq 800$ kPa. However, for $b_p \geq 30$ kPa, e is less as compared to e of $b_p \leq 20$ kPa. It can be inferred that fracture aperture opens up due to increase in b_p from 10 to 20 kPa. However, for $b_p \geq 30$ kPa, the flow becomes turbulent [refer Fig. 5-9(c) and (d)] and hence, computation of e from Cubic equation would be incorrect and hence the computed e for such higher b_p value is not reliable.

R_e was computed by employing Eq. 2.6 and the variation of R_e with σ_3 is depicted in Fig. 5-9, for b_p equal to 10, 20, 30, and 40 kPa, respectively. A line representing critical $R_e > 20$ (Zimmerman et al., 2004) is also added to show the transition in flow from laminar to turbulent. From these figures, it can be observed that, as expected, R_e is quite sensitive to both b_p and e_i , and the later changes significantly with an increase in σ_3 , which further affects R_e . A closer look at Fig. 5-9(a) reveals that flow through the fracture is laminar, corresponding to $b_p = 10$ kPa. On the other hand, for $b_p > 10$ kPa, the flow becomes turbulent, corresponding to $\sigma_3 < 500$ kPa and $e_i \geq 1.2$ mm, which further changes to laminar flow for $\sigma_3 > 500$ kPa.

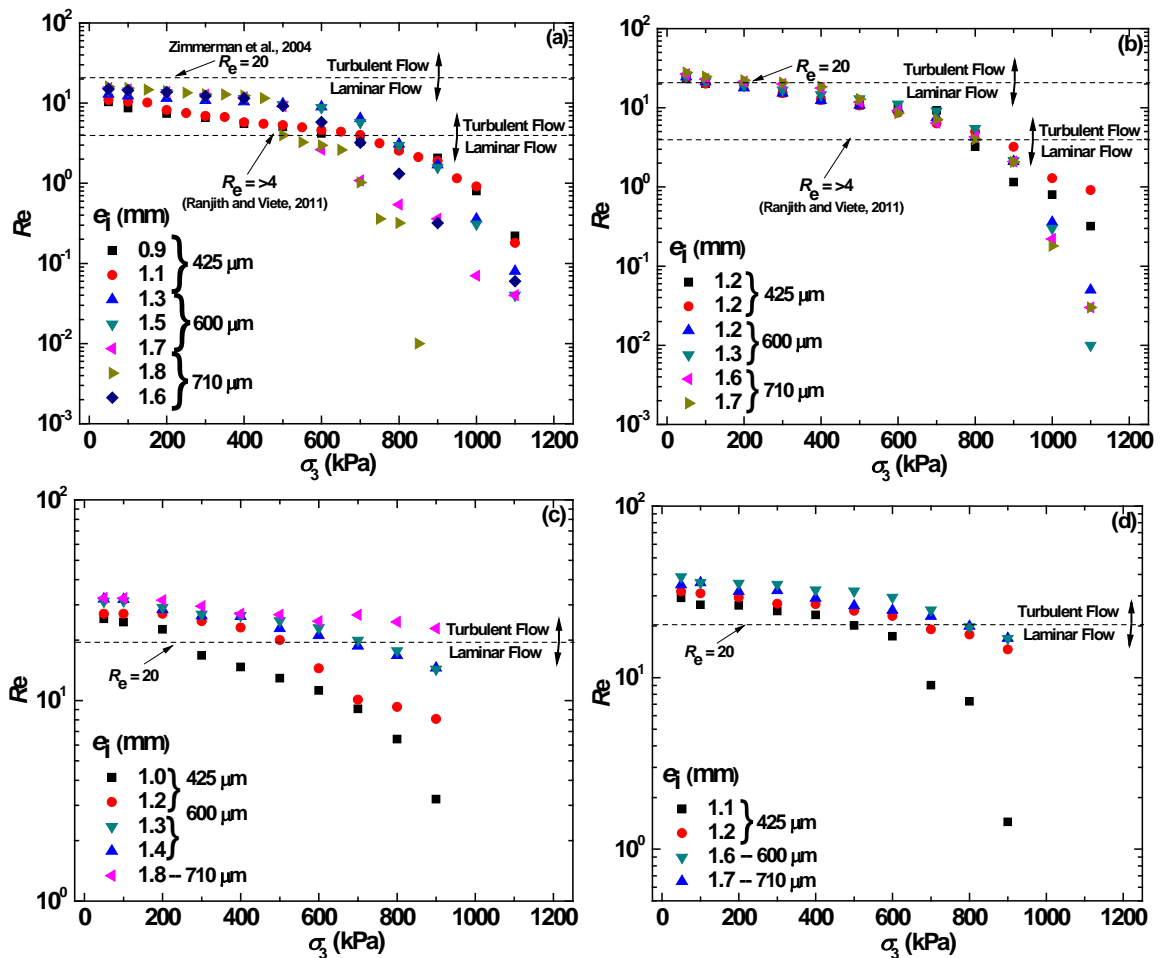
For a better appraisal, the variation in R_e with σ_3 corresponding to different values of b_p for $e_i > 1.2$ mm has been plotted, as depicted in Fig. 5-10. It can be observed from the figure that R_e increases with an increase in b_p and up to $b_p = 10$ kPa, the flow remains laminar while a further increase in b_p results in transition of flow from laminar to turbulent. It can also be observed that with an increase in $\sigma_3 > 400$ kPa, for $b_p > 20$ kPa, R_e changes from 23.5 to 12.5 and 27.87 to 18.40, corresponding to $e_i = 1.2$ mm and $e_i = 1.7$ mm, respectively, which indicates transition from turbulent to laminar flow. This transition in R_e can mainly be attributed to reduction in Q due to closure of the aperture at $\sigma_3 > 400$ kPa.



Figs. 5-7 The variation of (a) ΔQ_s and (b) ΔQ_i with σ_3 corresponding to $b_p = 10$ kPa



Figs. 5-8 The relationship between e and σ_3 corresponding to (a) various values of e_j (b) various values of b_p



Figs. 5-9 The variation of R_e with σ_3 for b_p equal to (a) 10 kPa, (b) 20 kPa, (c) 30 kPa and (d) 40 kPa

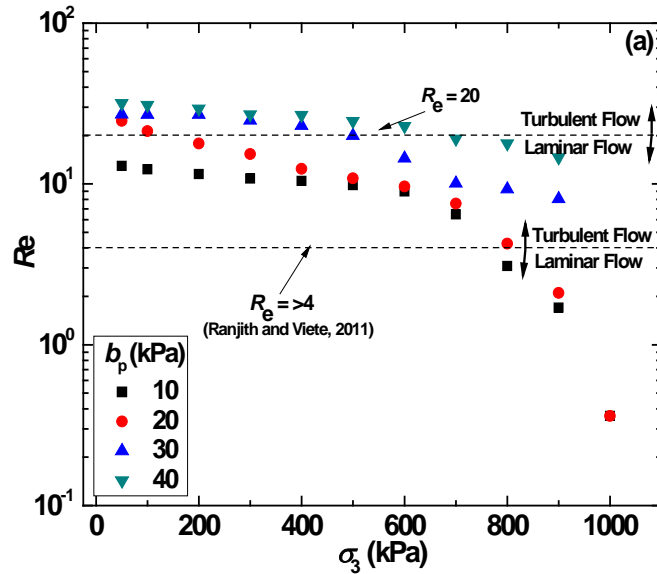


Fig. 5-10 The variation of Re with σ_3 corresponding to different values of b_p

The applicability of cubic law can be assessed by plotting the logarithm of fracture/joint aperture (difference between the initial aperture at zero stress and the final aperture at a certain stress) against the logarithm of a specific flow, $Q_{sf}(=Q/\Delta h)$, which results in a straight line with a slope of 3 for Eq. 2.3, (Cook, 1992). To verify the applicability of the cubic law, e has been back computed, for all the samples used in this study, by employing Eq. 2.3, as depicted in Appendix F, which also lists the changes in the fracture aperture, termed as apparent fracture aperture, $e_a(=e_i-e_f)$. The relationship between e_a and specific flow, $Q_{sf}(=Q/\Delta h)$, has been plotted for $b_p=10$ kPa as depicted in Fig. 5-11.

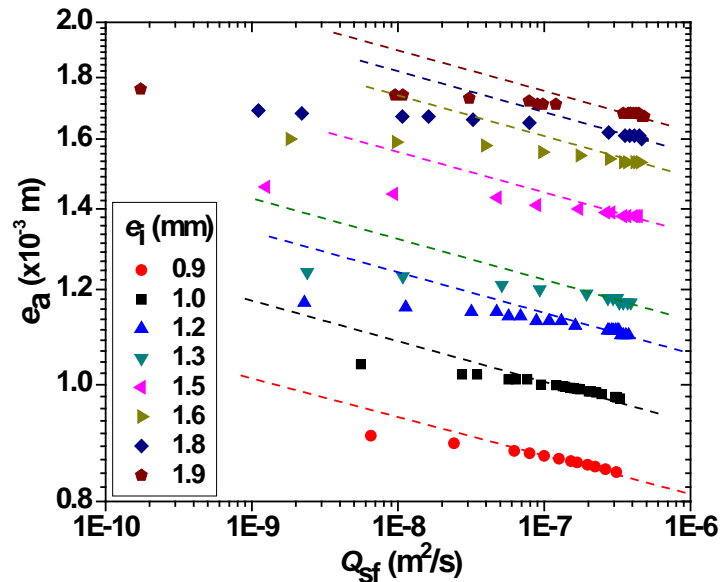


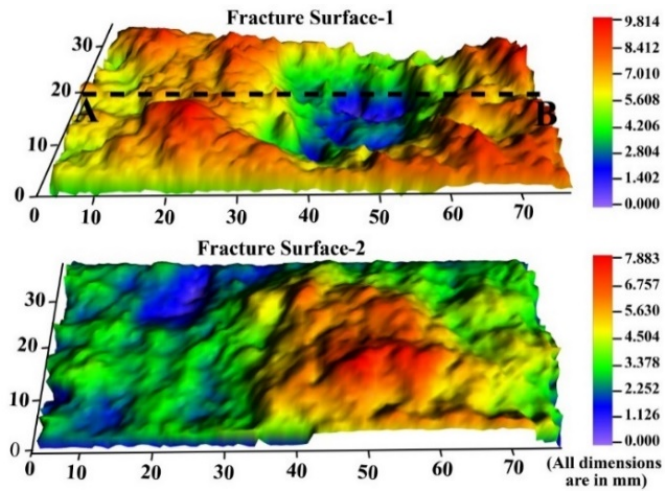
Fig. 5-11 The relationship between the apparent fracture aperture and the specific flow (corresponding to $b_p=10$ kPa)

It can be observed from the figure that, as expected, Q_{sf} decreases with an increase in e_a , which is consistent with the findings of the earlier researchers (Brown, 1987; Cook, 1992; Li et al., 1997; Brown, et al., 1998; Nicholl and Detwiler, 2001). When 1:3 sloping lines, representing the “cubic law” (Louis, 1969; Pyrak et al., 1987; Thompson and Brown, 1991; Cook, 1992), are fitted to the data, a substantial amount of data confirm the cubic law. It can be observed from the Fig. 5-11, that in case of $b_p = 10$ kPa, and for $e_i \leq 1.2$ mm, most of the data points ($\sigma_3 \leq 900$ kPa) fall on the 1:3 straight line. On the contrary, for $e_i > 1.2$ mm, data exhibits deviation ($\sigma_3 \geq 700$ kPa) from the straight line representing the cubic law. This indicates that the flow reduces more rapidly for $e_i > 1.2$ mm at high confining stress and hence this shows that cubic law is valid only for the smaller fracture aperture, and at low confining stress. These observations are consistent with the findings reported by earlier researchers (Witherspoon et al., 1980; Engelder and Scholz, 1987; Pyrak et al., 1987). Subsequently, the ranges of e_a and Q_{sf} , for which the data follows the cubic law were determined and listed in Appendix H. Corresponding to these e_a and Q_{sf} , the range of σ_3 was also determined, from the Fig. 5-4(a) corresponding to $b_p = 10$ kPa and the same is listed in Appendix H. It can be observed from the Appendix H that for $e_i \leq 1.2$ mm, the range of σ_3 corresponding to e_a and Q_{sf} , overlying the straight line cubic relationship is 50 to 900 kPa. This range of σ_3 reduces further with an increase in e_i and exhibits a large deviation of Q_{sf} and e_a as compared to the values represented by the cubic law. A reduction in the range of σ_3 corresponding to $e_i > 1.2$ mm indicates a rapid reduction in Q_{sf} due to an increase in e_a . This rapid reduction in Q_{sf} for $e_i > 1.2$ mm, as compared to $e_i \leq 1.2$ mm, can mainly be attributed to rapid closure of the fracture aperture due to an increase in grain to grain contact, which may further result in an increase in tortuosity, developed due to the presence of larger grains ≥ 600 μm in case of $e_i > 1.2$ mm, and lower values of the base pressure, $b_p = 10$ kPa. In such case, the flow rate is not proportional to the cube of the fracture aperture, as it would be for parallel smooth fracture aperture, but to a higher power of fracture aperture and therefore for $e_i > 1.2$ mm, most of the data points show deviation from the straight line (refer Fig. 5-11).

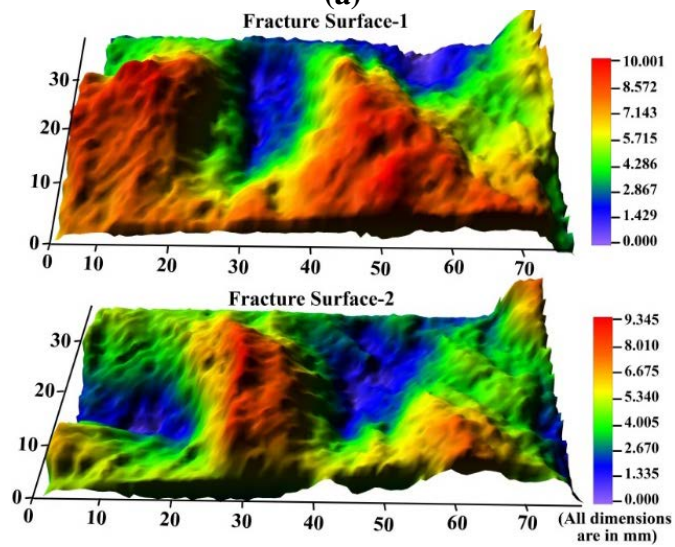
5.5 Determination of roughness of fracture surface

Data obtained from the 3D laser scanner of both the surfaces of fracture for the samples, S1-CG-38, S2-MG-38, S3-FG-38 and S1-CG-54, S2-MG-54 and S3-FG-54 were analyzed statistically and the following statistical parameters such as, mean, median, mode,

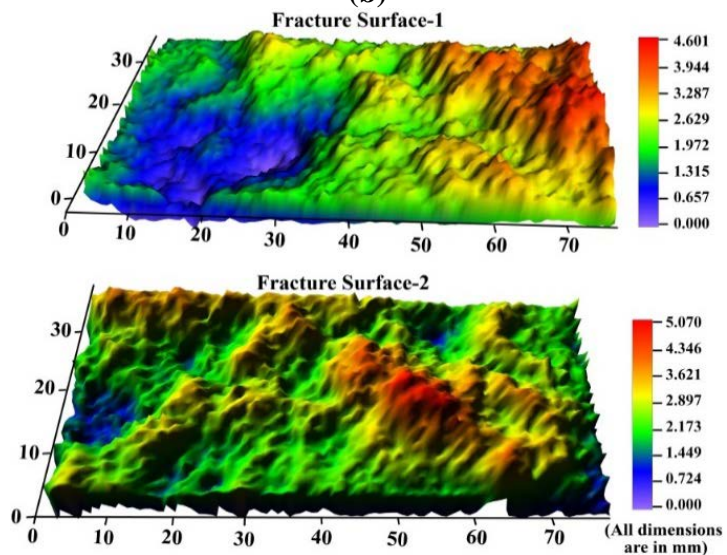
standard deviation, skewness, kurtosis, along with RMS roughness, R_q and roughness average, R_a were obtained and presented in Table 5-2 and Table 5-3 respectively. It can be observed from the Table 5-2, that the standard deviation and range (Max. – Min.), values of the fracture surface (FS_1) of samples, S1-CG-38, S2-MG-38 and S3-FG-38 are 1.89, 2.23, 0.95 and 9.81, 10.00, 4.60, respectively. Further, the parameters mean, median and variance for (FS_1) of samples, S1-CG-38, S2-MG-38 and S3-FG-38 are 4.56, 4.22, 3.59; 5.57, 5.64, 4.97; and 2.31, 2.34, 0.34 respectively. It can be inferred that the higher values of above mentioned parameters indicate rough surface, whereas, lower values indicate smooth surface and the same can be visualize from the 3D profile of the samples S1-CG-38, S2-MG-38, and S3-FG-38 (refer Fig. 5-12). Fig. 5-12(b), for sample S2-MG-38, shows more undulations in topography of the fracture surfaces as compared to Fig. 5-12(a) and Fig. 5-12(c) for samples S1-CG-38 and S3-FG-38, respectively. It can also be observed from the Table 5-2, that the calculated R_q and R_a by employing Eq.3.2 and 3.3, respectively, are well correlated and R_q values is systematically higher than the R_a values. Higher value of R_q and R_a (2.23 and 1.90, respectively) for FS_1 of sample S2-MG-38, indicate that the fracture surface is rough as compared to FS_1 of samples S1-CG-38 and S3-FG-38. Also, the FS_1 of sample S3-FG-38 shows the least R_q and R_a , values of 0.58 and 0.47, respectively, indicates the smooth fracture surface. Though, the sample S2-MG-38, consists of medium grain, the fracture surface developed by using tensile technique is more rough. This can be attributed to difference in mineral composition (presence of more Biotite mica), grain size distribution and presence of discontinuities (micro cracks/flaws) in the sample. However, fracture surface developed for samples S1-CG-38 and S3-FG-38 are rough and smooth, respectively, and systematically correlated with the grain size (visual identification) of the samples, i.e., finer the grain size, smoother the developed fracture surface. It is interesting to note that the fracture surface developed of samples, S1-CG-54, S2-MG-54 and S3-FG-54, also offers the similar behaviour (refer Table 5-3 and Fig. 5-13).



(a)

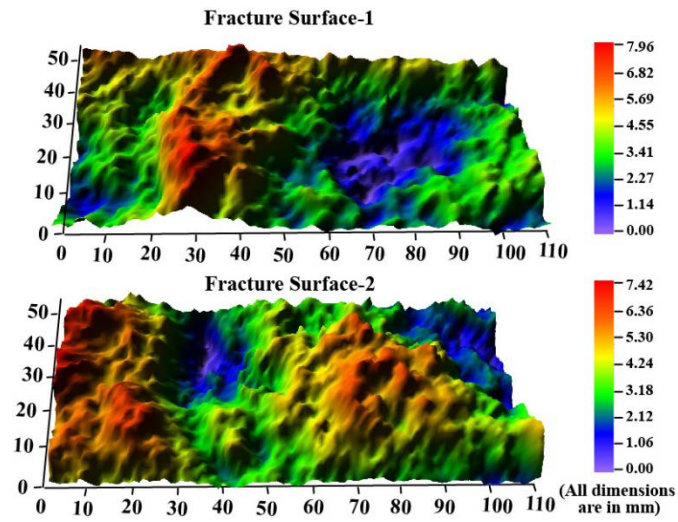


(b)

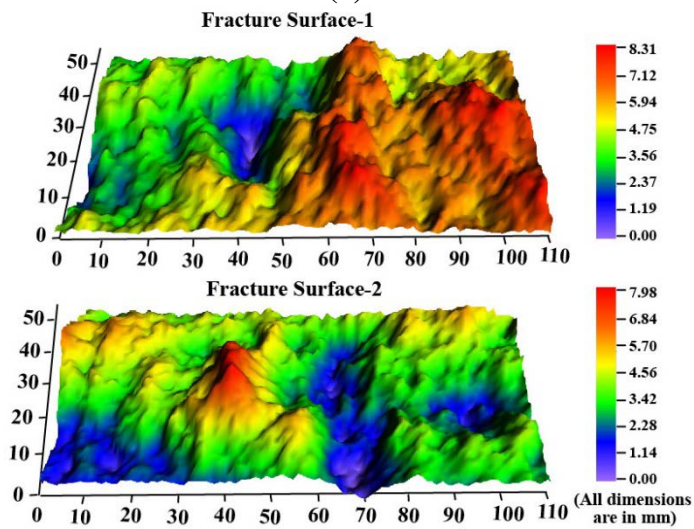


(c)

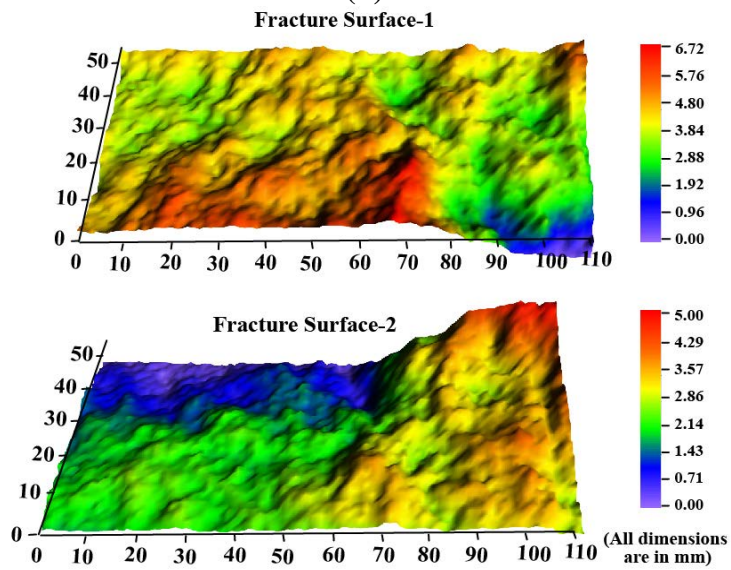
Figs. 5-12 3-Dimensional surface profile of the fracture surfaces of Samples (a) S1-CG-38, (b) S2-MG-38 and (c) S3-FG-38



(a)



(b)



(c)

Figs. 5-13 3-Dimensional surface profile of the fracture surfaces of Samples (a) S1-CG-54, (b) S2-MG-54 and (c) S3-FG-54

Table 5-2 Statistical parameters of the surfaces of the fracture/cylindrical halves (all values in mm) for 38 mm diameter rock samples

Statistical Parameter	S1-CG-38		S2-MG-38		S3-FG-38	
	FS ₁	FS ₂	FS ₁	FS ₂	FS ₁	FS ₂
Mean	4.56	4.24	5.57	4.20	2.31	2.36
Median	4.22	4.60	5.64	4.12	2.34	2.27
Standard Deviation	1.89	1.47	2.23	1.77	0.58	0.95
Sample Variance	3.59	2.17	4.97	3.15	0.34	0.90
Kurtosis	-0.79	-0.53	-1.02	-0.61	0.01	-0.73
Skewness	0.36	-0.60	-0.17	0.30	0.03	0.32
Standard Error	0.003	0.002	0.004	0.003	0.001	0.002
Range	9.81	7.88	10.00	9.35	4.60	5.07
Minimum	0.00	0.00	0.00	0.00	0.00	0.00
Maximum	9.81	7.88	10.00	9.35	4.60	5.07
RMS Roughness, R_q	1.89	1.47	2.23	1.77	0.58	0.95
Roughness Average, R_a	1.61	1.22	1.90	1.45	0.47	0.80
Confidence Level (95.0%)	0.007	0.005	0.008	0.006	0.002	0.003

Table 5-3 Statistical parameters of the surfaces of the fracture/cylindrical halves (all values in mm) for 54 mm diameter rock samples

Statistical Parameter	S1-CG-54		S2-MG-54		S3-FG-54	
	FS ₁	FS ₂	FS ₁	FS ₂	FS ₁	FS ₂
Mean	4.29	3.38	5.03	4.17	2.75	1.96
Median	4.30	3.20	5.17	4.28	2.54	1.92
Standard Deviation	1.40	1.48	1.53	1.52	1.12	0.86
Sample Variance	1.95	2.18	2.33	2.32	1.25	0.73
Kurtosis	-0.70	-0.55	-0.73	-0.89	-0.32	0.38
Skewness	-0.10	0.27	-0.31	-0.17	0.60	0.48
Range	7.96	7.42	8.31	7.98	6.72	5.00
Standard Error	0.002	0.003	0.002	0.002	0.002	0.001
Minimum	0.00	0.00	0.00	0.00	0.00	0.00
Maximum	7.96	7.42	8.31	7.98	6.72	5.00
RMS Roughness, R_q	1.40	1.48	1.53	1.52	1.12	0.86
Roughness Average, R_a	1.16	1.20	1.30	1.30	0.92	0.65
Confidence Level (95.0%)	0.004	0.005	0.004	0.005	0.004	0.003

5.6 Determination of Flow Characteristics of the Rockmass

Experimental results of the samples of rockmass having two different sizes (diameter to length ratio of 1:2), (a) Small samples - 38 mm and 76 mm and (b) Large samples - 54 mm and 108 mm, have been analyzed further and the relationship between Q and b_p , corresponding to different σ_3 values, have been plotted as depicted in Fig. 5-14 and Fig. 5-15 for both small and large samples having coarse, medium and fine grains, respectively. It can be observed from these figures that there exists a linear relationship between Q and b_p . It can also be inferred from these figures that the flow behavior is almost laminar for most of the data points except for the case, where the difference in σ_3 and b_p is $<1\text{MPa}$ (i.e., $\sigma_3=15\text{ MPa}$ and $b_p=14\text{ MPa}$). In such cases, most probably, the flow starts entering into the sample through the membranes and hence, the data deviates from approximately linear relationship between Q and b_p (such data are enclosed in a circle). As most of the measured experimental data of the Q and b_p plots (refer Fig. 5-14 and Fig. 5-15) follow the linear trend, it can be assumed that the flow through the fracture obeys the Darcy's law. So, the well-known "cubic law", which assumes linear flow between two parallel smooth plates (Gangi, 1978; Kranz et al., 1979; Tsang and Witherspoon, 1981; Schrauf and Evans, 1986) can be employed to estimate the hydraulic fracture aperture (e) of the fractures (by assuming the density of water $=997.05\text{ kg/m}^3$ at $25\text{ }^\circ\text{C}$ and the dynamic viscosity of water $=8.90\times 10^{-4}\text{ kg/m}\cdot\text{s}$ for water, at $25\text{ }^\circ\text{C}$). Further, it must be noted that it would require highly sophisticated instrumentation to measure hydraulic aperture of the fracture, which decreases due to incremental change in the confining pressure.

Further, the variation in Q , with σ_3 , for coarse, medium and fine grained sample for $b_p = 2, 4, 8, 14, 18,$ and 25 MPa has been plotted as depicted in Fig. 5-16, and Fig. 5-17, respectively, for both the sizes of samples. It can be noticed from these figures that the reduction in Q with σ_3 is less for the fine grained sample as compared to its counterparts, for all the values of b_p . The trend for fine grained samples can be clearly distinguished in all these figures, and the variation in Q is much more prominent. Whereas, in case of the coarse and medium grained samples, the behavior is highly puzzling and crossing over each other. However, Fig. 5-16(f) shows prominent variation in Q with σ_3 , for coarse, medium and fine grained samples. It can be observed from this figure that in case of the coarse grained sample, Q is less as compared to the medium and fine grained sample. This can be mainly attributed to the fact that at high σ_3 , ($\geq 40\text{ MPa}$), the effect of fracture roughness and tortuosity are more prominent in case of coarse grained samples and hence the behavior of

Q at $b_p=25$ MPa is quite distinct. Whereas, Q is higher for fine grains, which is having less roughness (refer Table 5-2) and hence the less tortuous path of flow as compared to the medium and coarse grained samples (refer Fig. 5-16f).

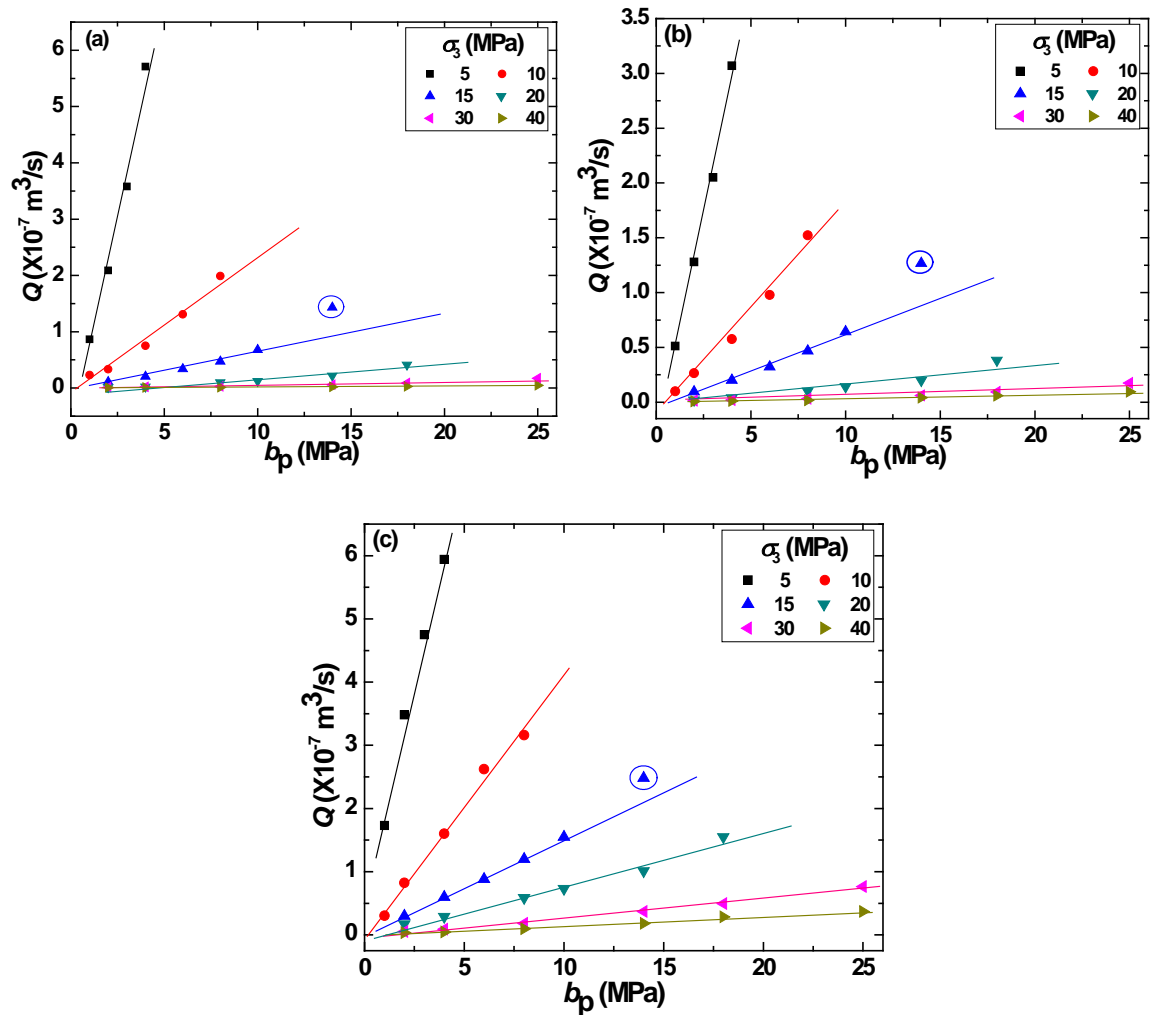


Fig. 5-14 The variation of Q with b_p for samples (a) S1-CG-38, (b) S2-MG-38 and (c) S3-FG-38

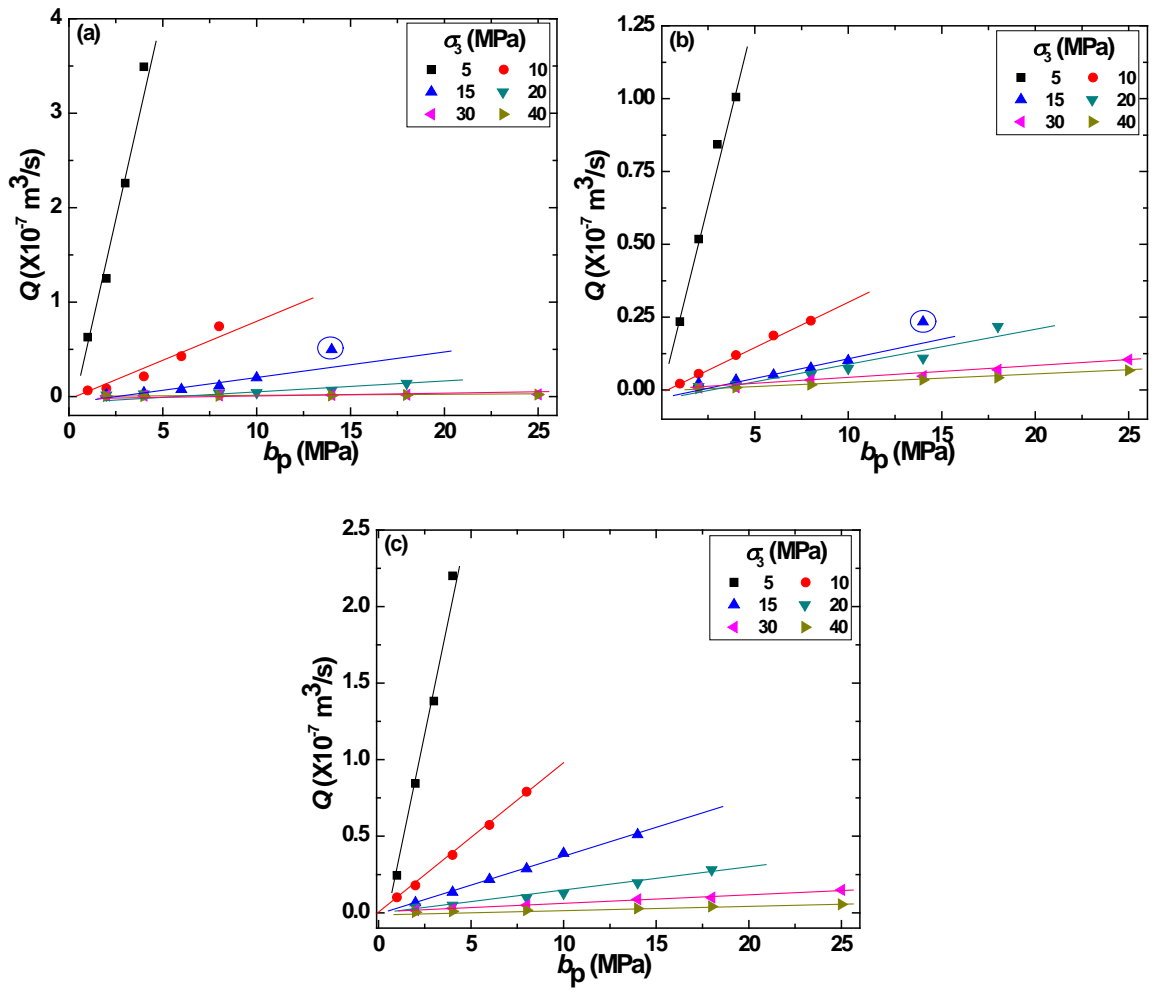


Fig. 5-15 The variation of Q with b_p for samples (a) S1-CG-54, (b) S2-MG-54 and (c) S3-FG-54

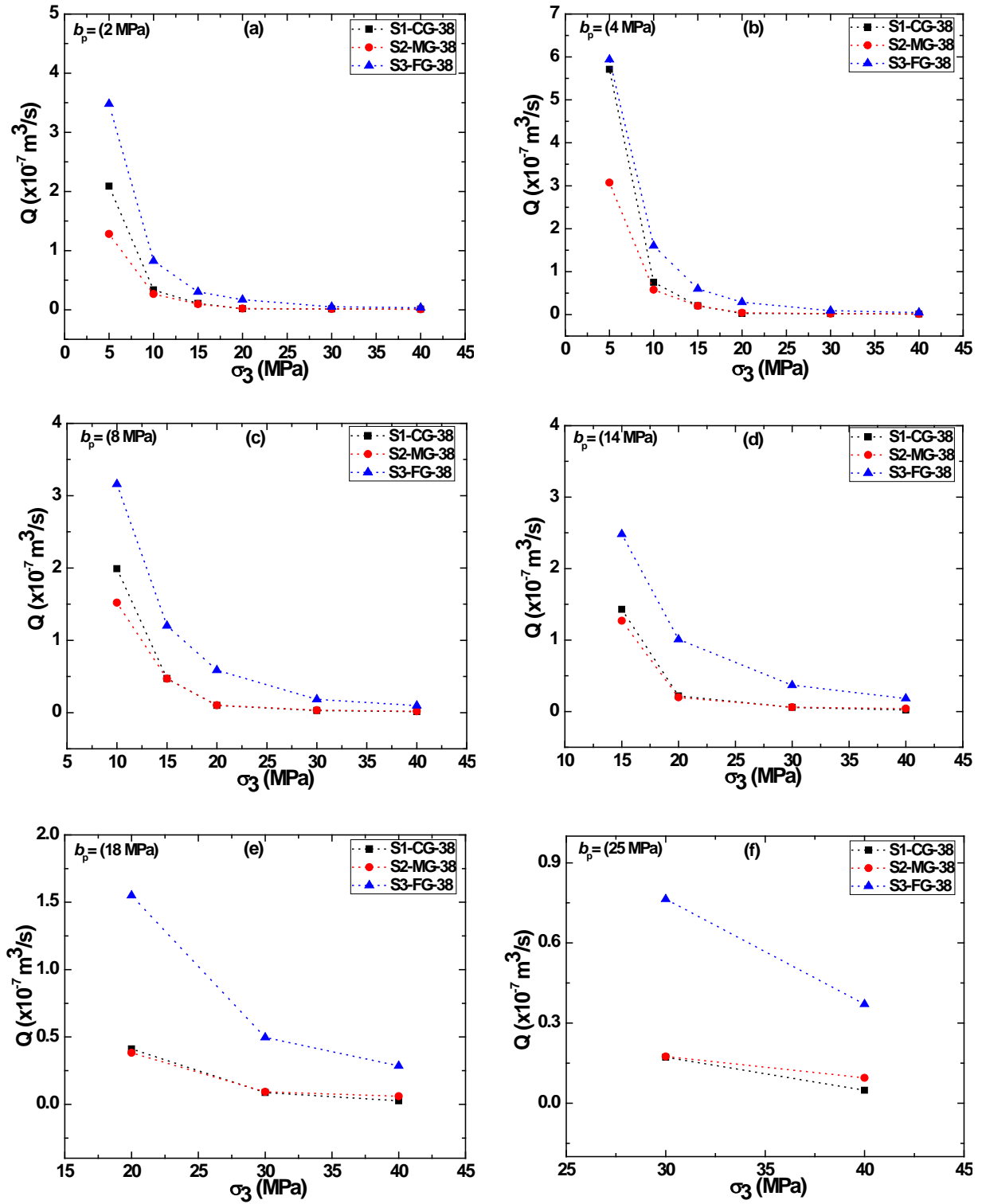


Fig. 5-16 The variation of Q with the σ_3 corresponding to different b_p for the samples S1-CG-38, S2-MG-38 and S3-FG-38

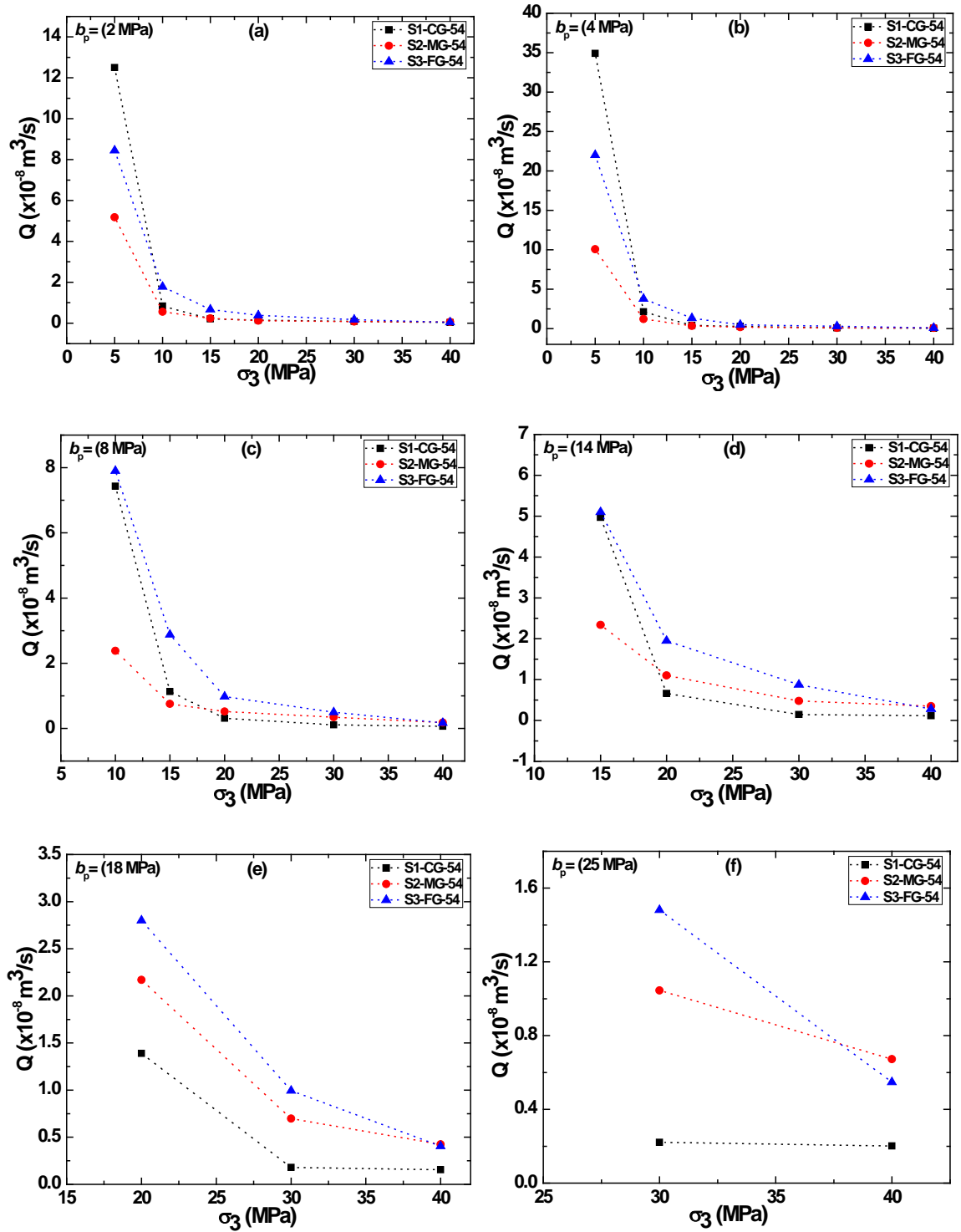


Fig. 5-17 The variation of Q with the σ_3 corresponding to different b_p for the samples S1-CG-54, S2-MG-54 and S3-FG-54

The variation of hydraulic aperture, e (back computed from the Cubic law relation), with b_p , for coarse, medium and fine grained samples for several values of σ_3 , have been plotted as depicted in Fig. 5-18 and Fig. 5-19, for both the samples, respectively. It can be observed from these figures that e increases with an increase in b_p , and non-linear relationship exists between e and b_p for all the samples. It can also be observed from Fig. 5-18 and Fig. 5-19, that the variation in e , with b_p , decreases with an increase in σ_3 . This can be attributed to the fact that at higher values of σ_3 , effect of b_p on Q is less significant. These observations are consistent with the findings reported by earlier researchers (Witherspoon et al., 1980; Engelder and Scholz, 1987; Pyrak et al., 1987; Ranjith, 2010).

Further, e with σ_3 , for coarse, medium and fine grained samples for several values of b_p , have been plotted as depicted in Figs. 5-20 and Figs. 5-21, for both the samples sizes (38 mm and 54 mm), respectively. It can be observed from these figures that e decreases non-linearly with σ_3 for all the samples. A closer view of Fig. 5-20 (a) and Fig. 5-21 (a) for smaller and larger samples respectively, corresponding to $b_p = 2\text{MPa}$, indicate that before $\sigma_3 \leq 15\text{ MPa}$, closure of e is quite significant and rapid. However, after $\sigma_3 \geq 15\text{ MPa}$, reduction in e is less and gently and becomes almost constant and finally amalgamate at a point ($\sigma_3 \geq 40\text{ MPa}$). It can be inferred that beyond $\sigma_3 \geq 15\text{ MPa}$, most of the asperities of the fracture have joined together and hence beyond $\sigma_3 \geq 15\text{ MPa}$, reduction in e is less and gentle. However, further reduction is only possible after the rupture or deformation of the asperities which requires quite high stress.

It can also be observed from these figures (refer Figs. 5-20 and Figs. 5-21) that reduction in e is less in samples S3-FG-38 and S3-FG-54 as compared to the S1-CG-38, S2-MG-38 and S1-CG-54, S2-MG-54. It should be noted that S3-FG-38 and S3-FG-54 are of fine grained and with less R_q and R_a values (refer Tables 5.2 and 5.3) indicate smooth fracture surfaces. As the average height of asperities in samples S3-FG-38 and S3-FG-54 are smaller, as compared to samples S1-CG-38, S2-MG-38 and S1-CG-54, S2-MG-54 (refer Figs. 5.12 and Figs. 5.13), the closure of fracture aperture or asperities contact is also less, for samples with smooth fracture surfaces. On the contrary, samples S1-CG-38, S2-MG-38 and S1-CG-54, S2-MG-54 indicates more reduction in e as these samples consists of larger asperities (refer Figs. 5-12 and Figs. 5-13).

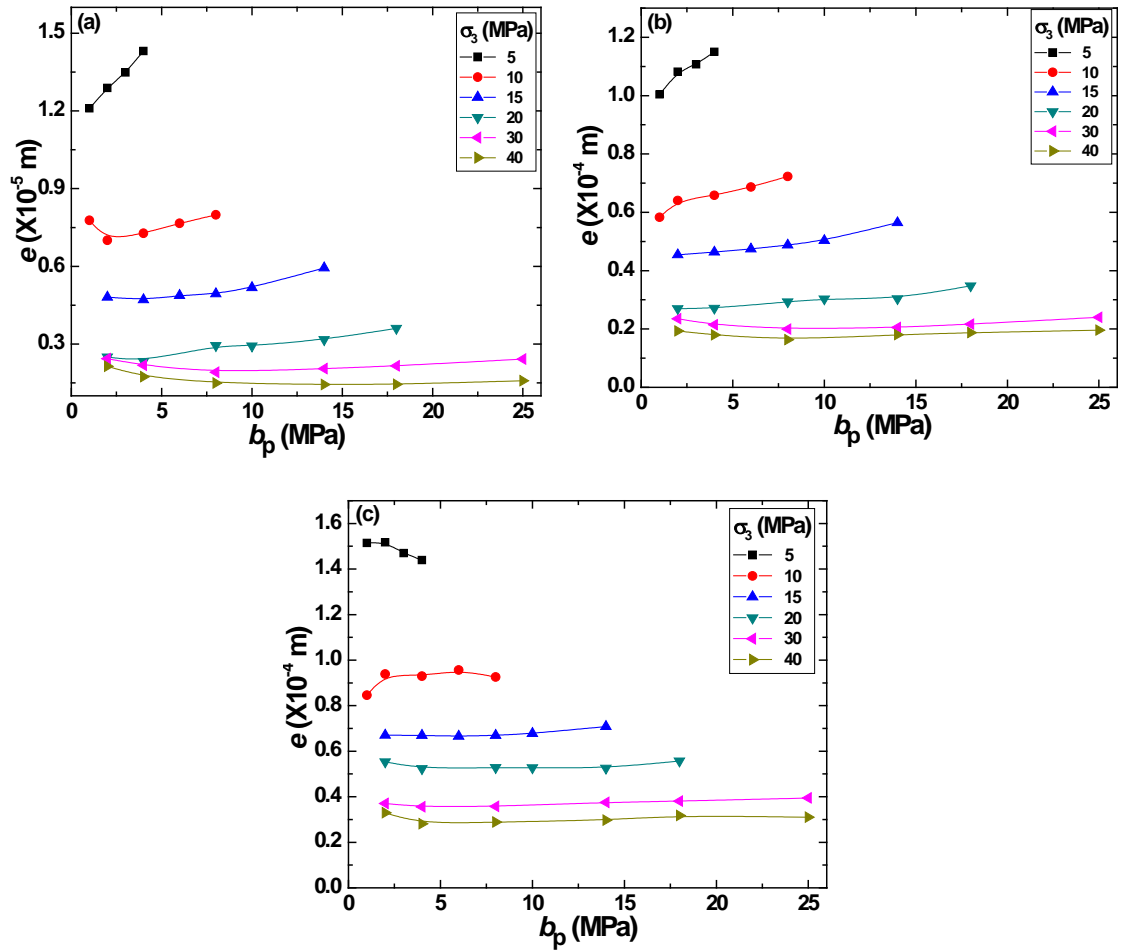


Fig. 5-18 The variation of hydraulic fracture aperture, e , with base pressures, b_p , for samples (a) S1-CG-38, (b) S2-MG-38 and (c) S3-FG-38

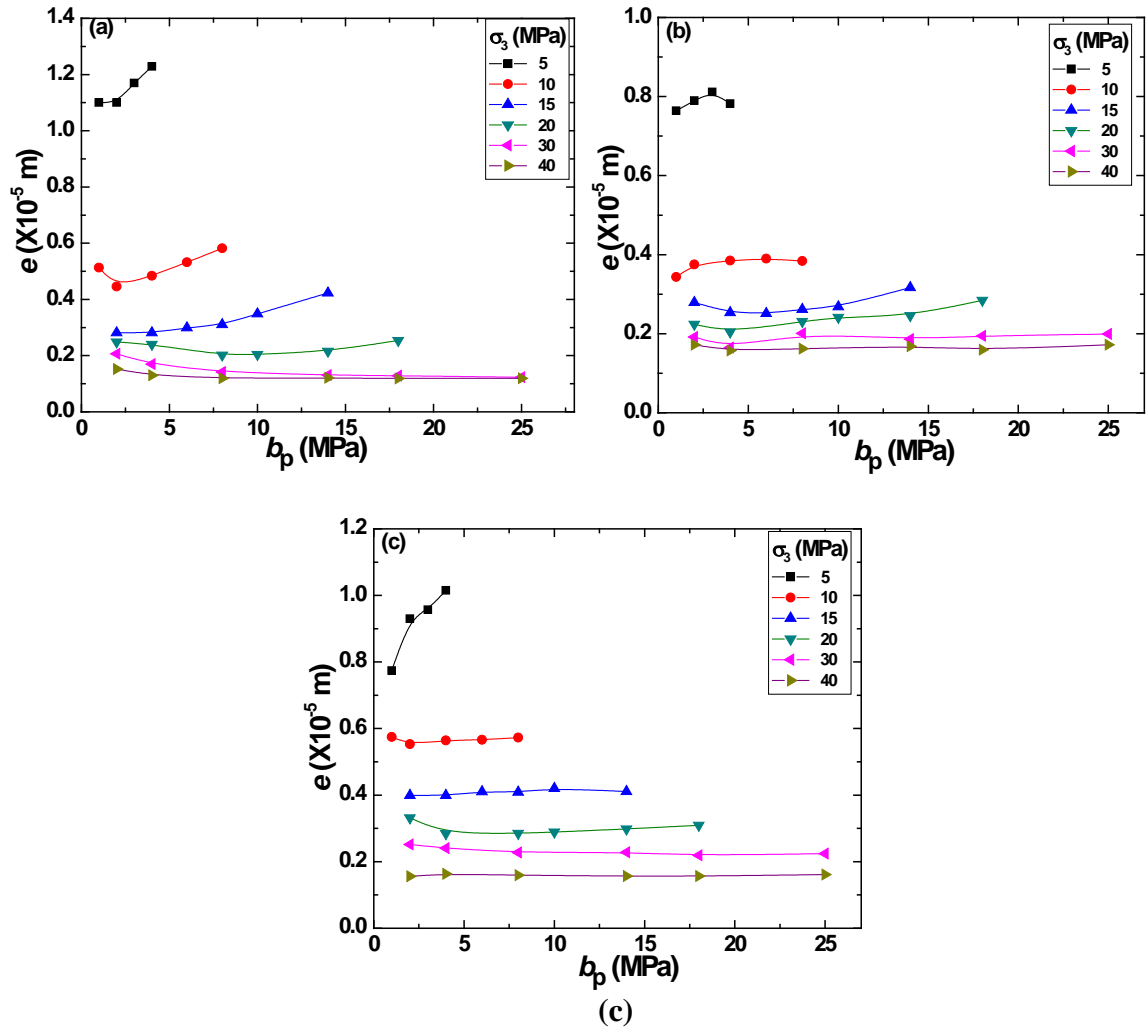


Fig. 5-19 The variation of hydraulic fracture aperture, e , with base pressures, b_p , for samples (a) S1-CG-54, (b) S2-MG-54 and (c) S3-FG-54

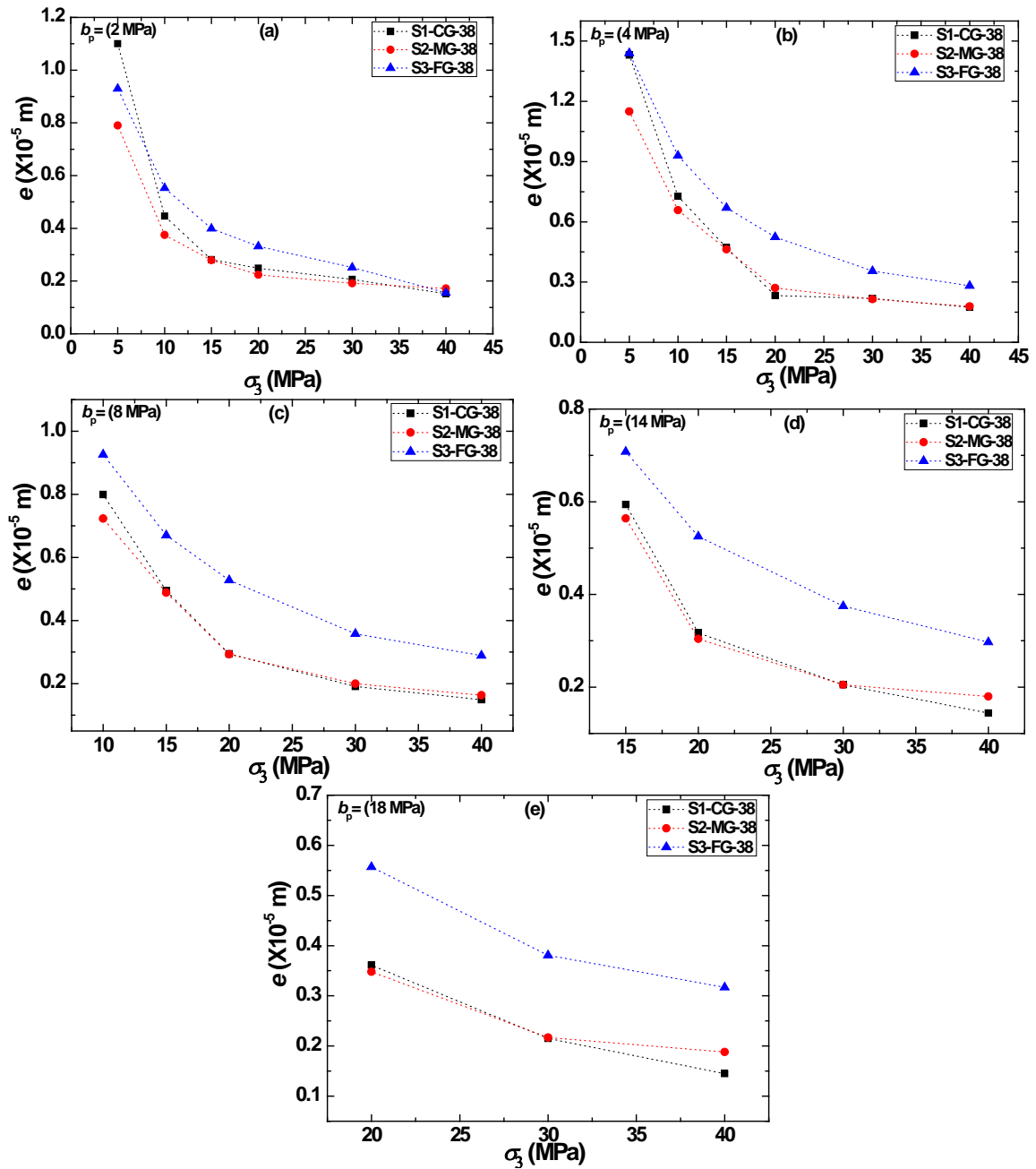


Fig. 5-20 The variation of e with σ_3 corresponding to different b_p , for sample S1-CG-38, S2-MG-38 and S3-FG-38

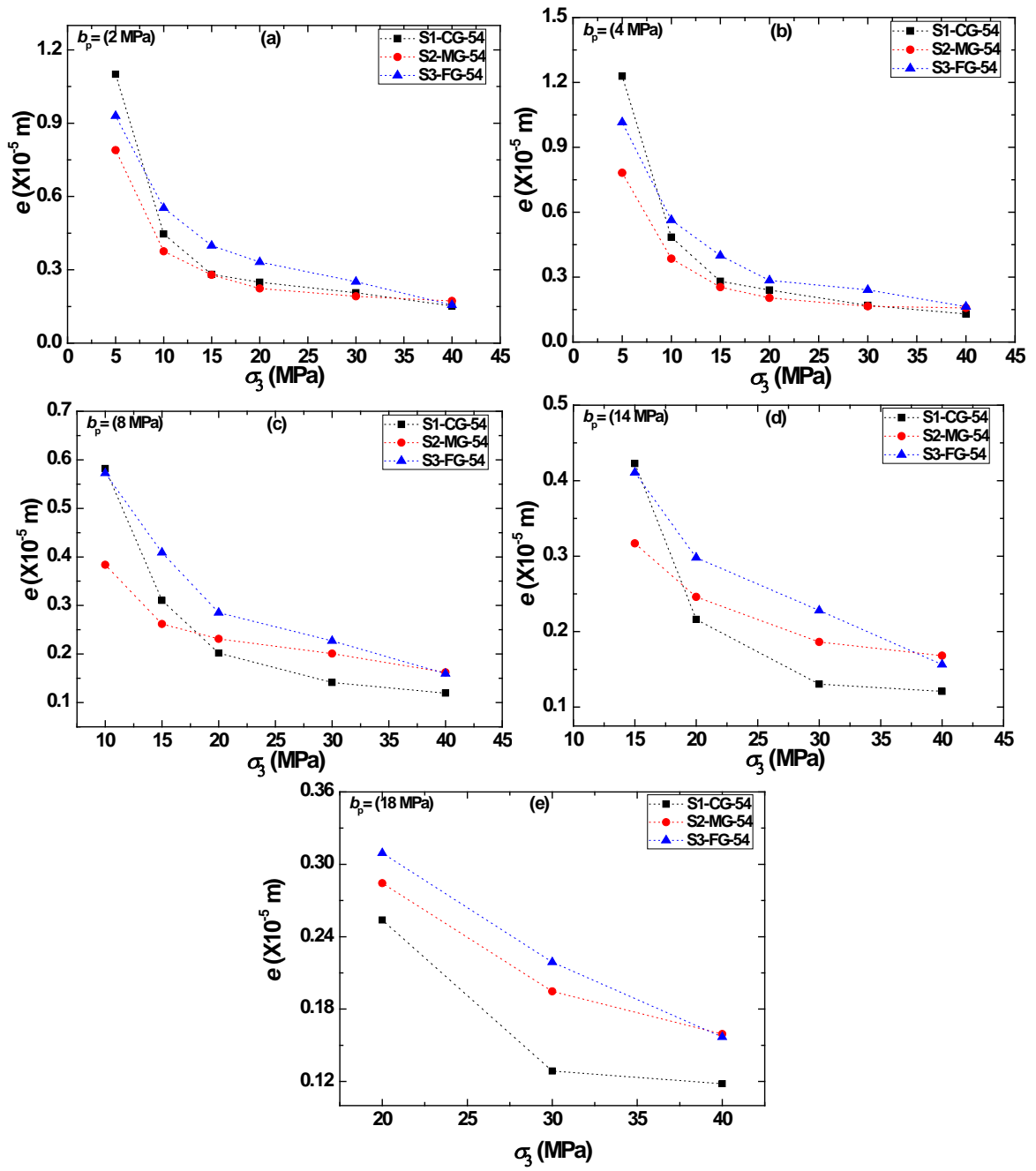


Fig. 5-21 The variation of e with σ_3 corresponding to different b_p , for samples S1-CG-54, S2-MG-54 and S3-FG-54

The variation in Q with respect to effective confining pressure, $\sigma_{\text{eff.}} (= \sigma_3 - b_p)$, for samples S1-CG, S2-MG and S3-FG has been plotted in Fig. 5-22(a) and (b), for small and large samples, respectively. It can be observed from the figures that Q decreases almost non-linearly with $\sigma_{\text{eff.}}$, and the variation in Q with $\sigma_{\text{eff.}}$, is less significant for samples S1-CG-38 and S2-MG-38, and S1-CG-54 and S2-MG-54. On the contrary, the effect of fracture roughness is quite distinct for the samples S3-FG-38 and S3-FG-54, showing higher Q .

Further, the variation in Q with $\sigma_{\text{eff.}}$ is negligible, corresponding to coarse, medium and fine grained samples at $\sigma_{\text{eff.}} \geq 20$ MPa and $\sigma_{\text{eff.}} \geq 15$ MPa, for smaller and larger samples, respectively. This indicates that fracture roughness does not contribute to fluid flow beyond certain critical $\sigma_{\text{eff.}} \geq 20$ MPa and $\sigma_{\text{eff.}} \geq 15$ MPa, for smaller and larger samples respectively. Further, the fracture aperture is changing to residual aperture beyond $\sigma_{\text{eff.}} \geq 20$ MPa and $\sigma_{\text{eff.}} \geq 15$ MPa, for smaller and larger samples respectively. It can be inferred that most part of the asperities comes in contact with each other at higher effective stress and fluid flow through such fracture completely ceases and asymptote at a point, as depicted in Fig. 5-22(a) and (b). It can also be observed from the Fig. 5-22 that Q is less for the larger samples on contrary to the smaller samples.

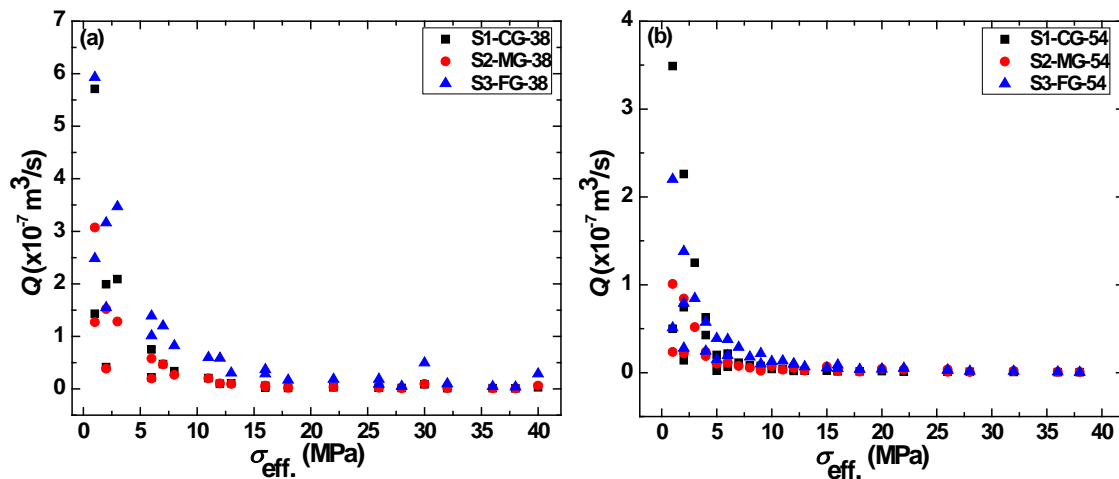


Fig. 5-22 Discharge as a function of effective confining pressure, (a) small samples and (b) large samples

The variation of R_e with b_p for samples S1-CG-38, S2-MG-38 and S3-FG-38 and S1-CG-54, S2-MG-54 and S3-FG-54, is depicted in Fig. 5-23 and Fig. 5-24, respectively. For the sake of brevity, typical data sheet of measured and calculated parameters for sample, S1-CG-38 is depicted in Appendix J. It can be observed from the Appendix J, Fig. 5-23 and Fig. 5-24, that as expected R_e is quite sensitive to b_p and linear relationship exists between R_e and b_p .

Further, a line representing $Re > 10$ (Hassanizadeh and Gray, 1987) was added to mark the transition in flow from laminar to turbulent and it can be observed from the Fig. 5-23, that most of the data points of all the samples falls below the line $Re > 10$, except for the case of S1-CG-38 and S3-FG-38, corresponding to $\sigma_{eff.} < 2$ MPa and $b_p > 2$ MPa. It should be noted that the sample S1-CG-38 is coarse grained sample with high R_q and R_a values (refer Table 5-2) indicates rough fracture surface and large aperture. In case of large aperture, effect of surface roughness becomes negligible and hence higher Q and higher $Re > 10$. On the contrary, sample S3-FG-38 has less R_q and R_a values (refer Table 5-2), which indicate smooth fracture surface and less tortuous path of the flow corresponding to $\sigma_3 \leq 5$ MPa and hence yields higher discharge and higher $Re (> 10)$. For such cases, transition in flow takes place from laminar to turbulent and computation of e employing cubic law relationship would result in incorrect results.

Also, a line representing $Re > 4$ (Ranjith and Viete, 2011) was added to the Fig. 5-23, to further quantify the transition boundary and it can be observed from Fig. 5-23(a) that sample S1-CG-38, yields higher $Re (> 4)$, for most of the data points, except for the case, where $\sigma_{eff.} < 5$ MPa. This can be mainly attributed to higher Q , due to less reduction in e . On the contrary, with an increase in $\sigma_{eff.} > 5$ MPa, Q reduces rapidly due to higher reduction in e , which indicates $Re < 4$. Flow path increases due to variable surface roughness as indicated in Fig. 5-25. The length of the fractured surface (l_2) has increased as compared to plane smooth surface (l_1).

Further, it can also be observed from Fig. 5-23(c) that sample, S3-FG-38 having less R_q and R_a values (refer Table 5-2) indicate higher $Re > 4$, for most of the data points, corresponding to $\sigma_3 < 10$ MPa and for such cases, influence of b_p on Re is much more pronounced. On the contrary, with an increase in $\sigma_3 > 10$ MPa, influence of b_p on Re is less. It can be inferred that in case of smooth fracture surface, corresponding to $\sigma_3 < 10$ MPa, flow takes place through less tortuous path and hence higher $Re > 4$, suggest turbulent flow. However, with $\sigma_3 > 10$ MPa, due to closure of fracture aperture, Q is less and hence $Re < 4$ was observed. On the contrary, samples, S2-MG-38 and S2-MG-54, are having higher roughness value [refer Table 5-2, Table 5-3 and Fig. 5-23(b), Fig. 5-24(b)] shows low $Re < 4$, corresponding to $\sigma_3 > 10$ MPa.

It can be observed from the Fig. 5-23 that all the data points of all the samples falls below a line representing $Re > 10$ [Hassanizadeh and Gray (1987)]. However, according to Ranjith and Viete, (2011), $Re > 4$ indicate turbulent flow, so it can be observed from the Fig. 5-23(a) and (c) corresponding to coarse and fine grained samples respectively that only at

low confining pressure <5 MPa and $b_p > 2$ MPa indicate turbulent flow conditions and others show laminar flow condition.

The variation in Q with σ_3 corresponding to both the sample sizes (38 mm and 54 mm diameter, respectively) is depicted in Figs. 5-27, Figs. 5-28 and Figs. 5-29 for coarse, medium and fine grained samples, respectively. It can be observed from these figures that larger the sample size, lesser the Q and this variation is quite distinct in all the samples. It can also be observed from these Figs. 5-27, Figs. 5-28 and Figs. 5-29, that Q decreases with an increase in σ_3 and non-linear relationship exists between Q and σ_3 . A closer look at Fig. 5-27(a), indicates that for $\sigma_3 \geq 20$ MPa, data of both the samples becomes asymptotic and beyond $\sigma_3 > 20$ MPa, no significant variation can be noticed. It can be inferred that the effect of sample size is not perceptible beyond $\sigma_3 \geq 20$ MPa, which indicates that effect of σ_3 is much pronounced than the b_p on the Q .

The variation in R_e with $\sigma_{eff.}$, is plotted in Figs. 5-26, indicate that R_e is decreasing non-linearly with $\sigma_{eff.}$. Most of the data points falls below the line representing $R_e > 10$ shows laminar flow conditions. It can also be observed that R_e is decreasing rapidly with $\sigma_{eff.}$, initially upto $\sigma_{eff.} \leq 20$ MPa and beyond $\sigma_{eff.} \geq 20$ MPa, data of all the samples becomes asymptotic and no significant variation can be perceived. It can be inferred that the effect of surface roughness on R_e is insignificant beyond $\sigma_{eff.} \geq 20$ MPa. This is mainly because of complete closure of e at $\sigma_{eff.} \geq 20$ MPa and Q can't occur hence, R_e becomes almost constant beyond $\sigma_{eff.} \geq 20$ MPa.

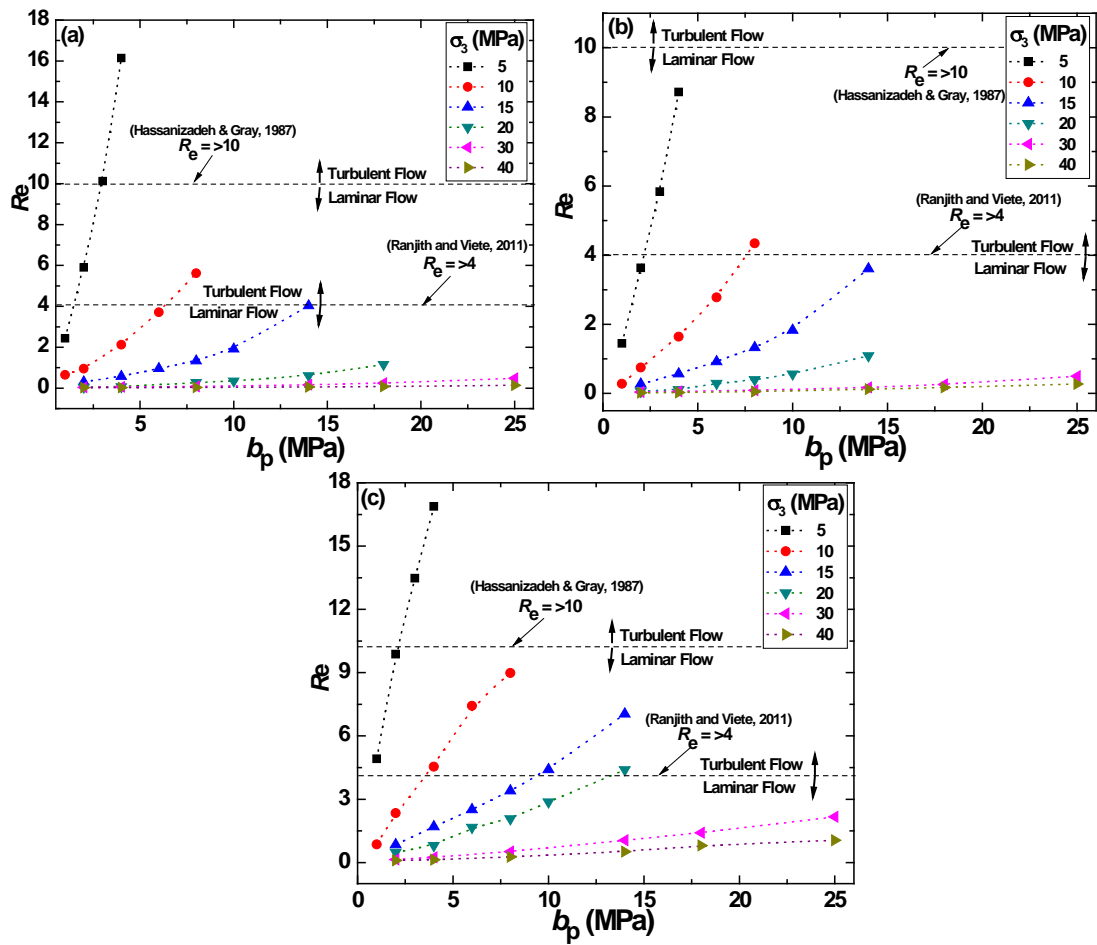


Fig. 5-23 The variation of Re with b_p corresponding to different σ_3 , for samples (a) S1-CG-38, (b) S2-MG-38 and (c) S3-FG-38

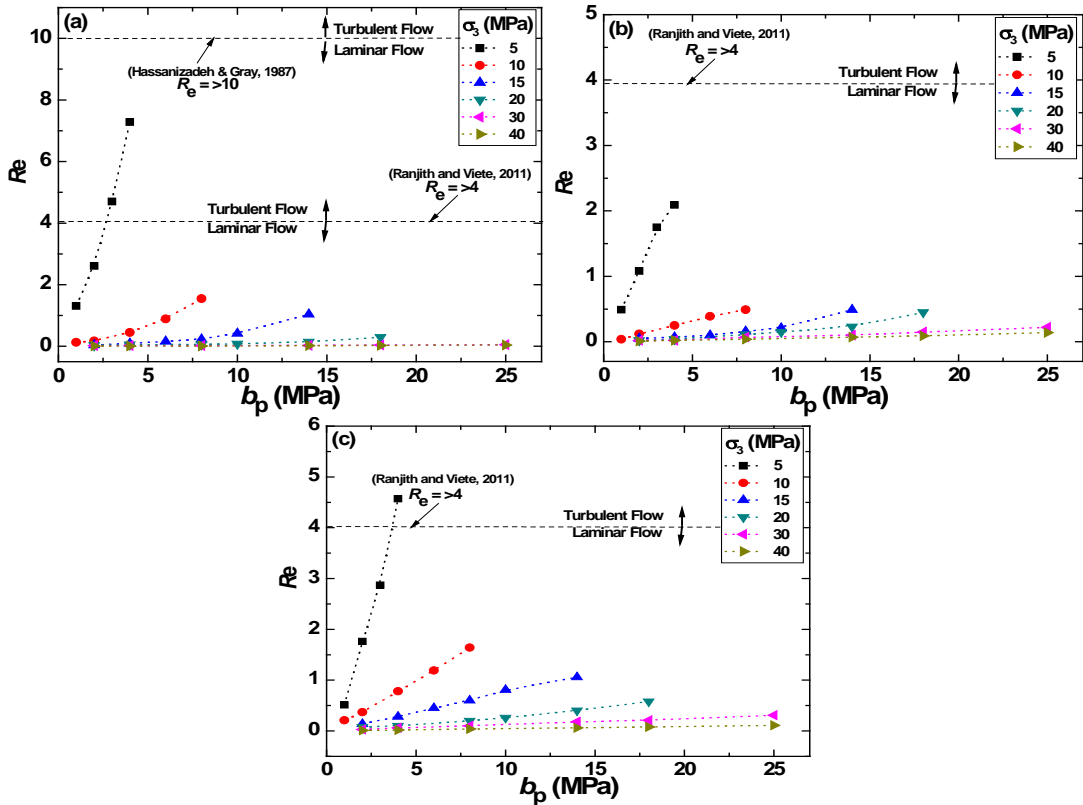


Fig. 5-24 The variation of Re with b_p corresponding to different σ_3 , for samples S1-CG-54, (b) S2-MG-54 and (c) S3-FG-54

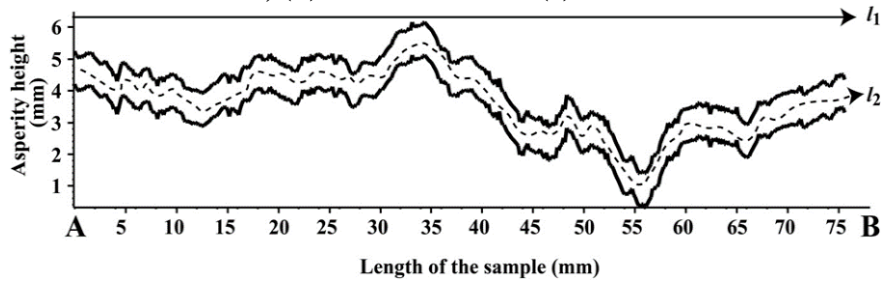


Fig. 5-25 A. The computed surface roughness profile from the center of the sample S1-CG-38, showing length l_1 and l_2

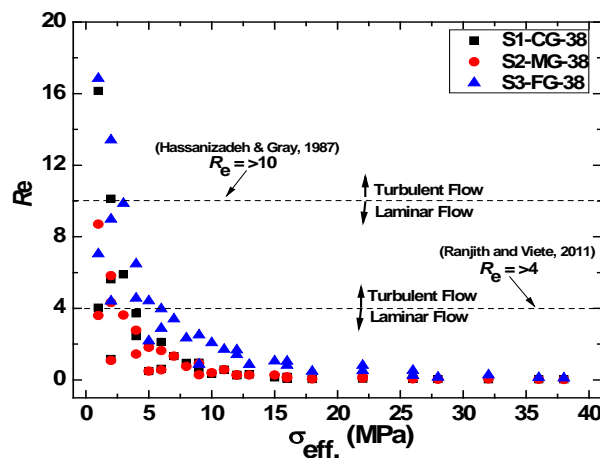


Fig. 5-26 The variation of Re with σ_{eff} .

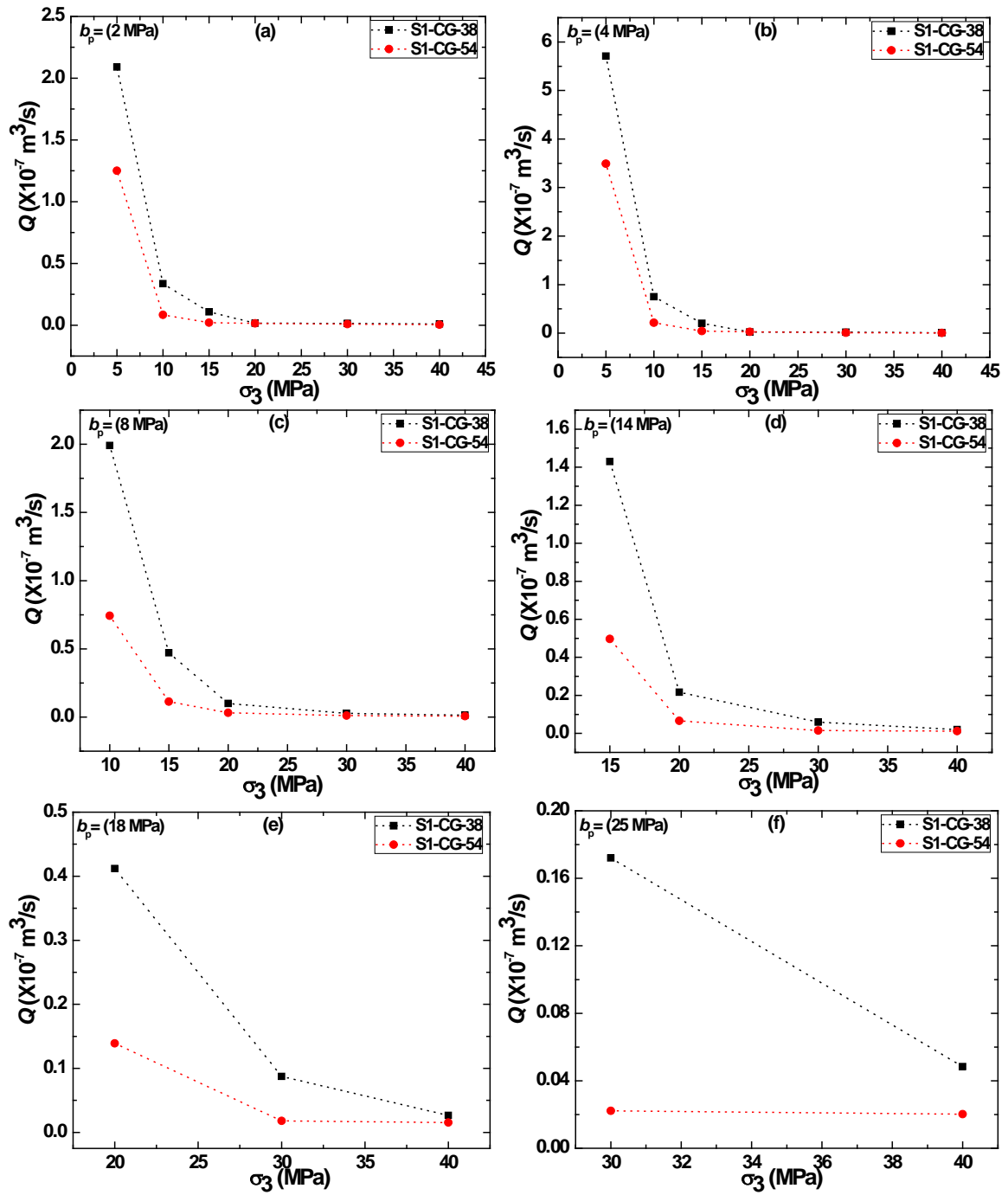


Fig. 5-27 The variation of Q with σ_3 corresponding to different b_p for coarse grained samples

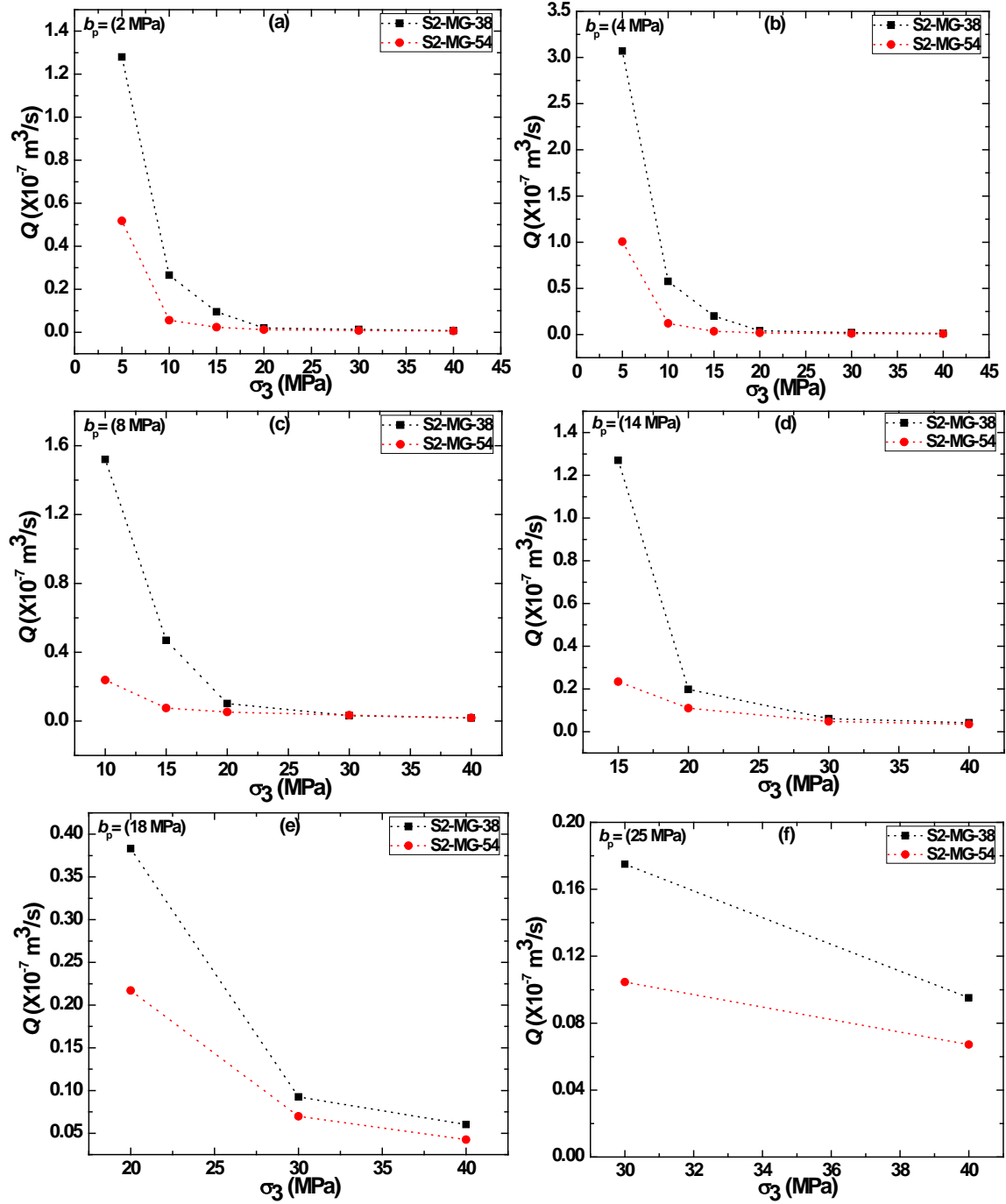


Fig. 5-28 The variation of Q with σ_3 corresponding to different b_p for medium grained samples

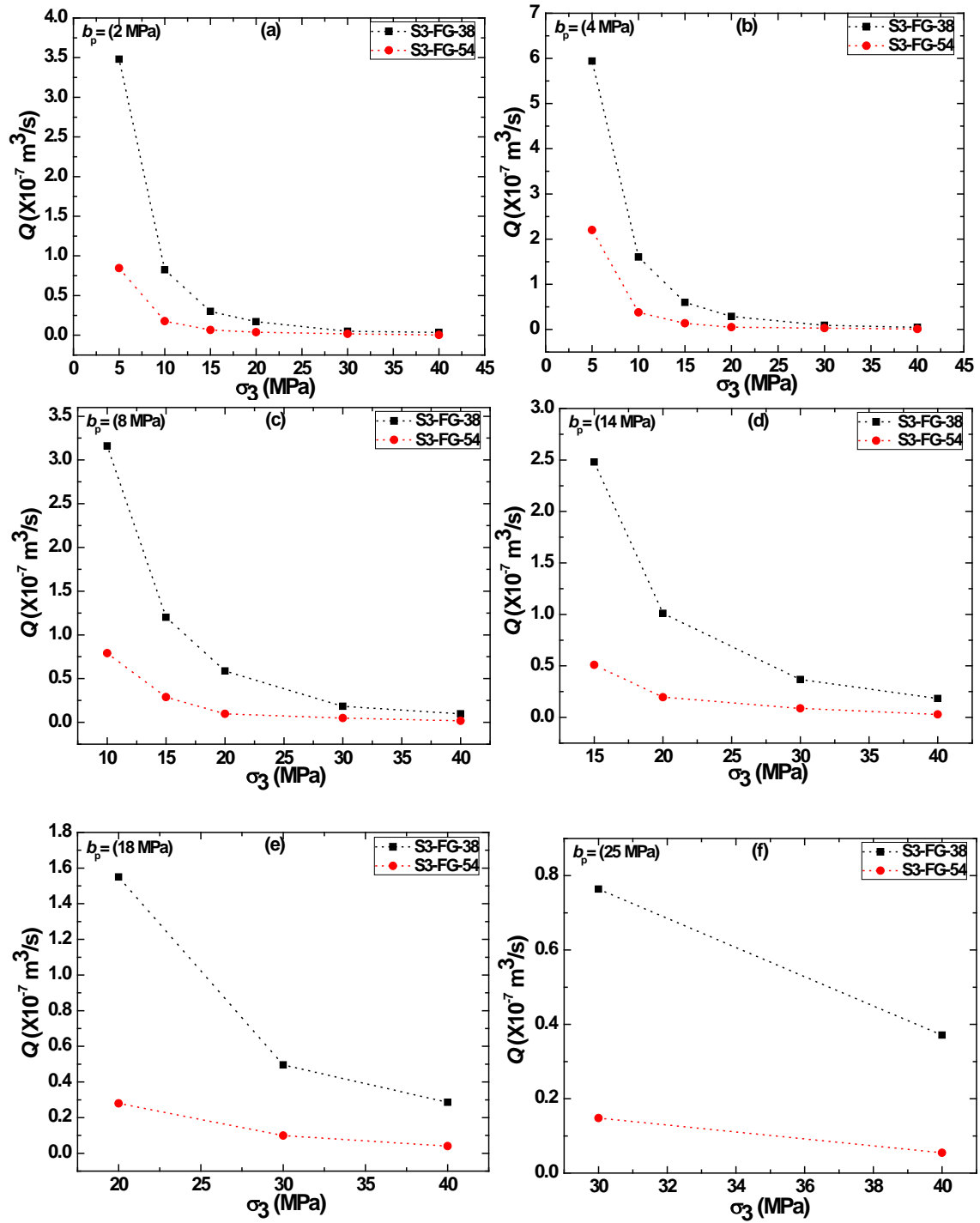


Fig. 5-29 The variation of Q with σ_3 corresponding to different b_p for fine grained samples

5.7 A comparison of the flow properties of the analogue and natural materials

A comparison between the analogue and natural materials was established by plotting the variation of Q with respect to σ_3 on the same scale, as depicted in Fig. 5-30. For a better understanding, the plotting has been done on a log-log scale. It can be inferred from the figure that though both the materials are different in terms of strength, S , modulus of elasticity, E , density, ρ and Poisson's ratio, ν , the mechanism of fluid flow through them remains unchanged. It can also be observed from the trends depicted in the figure that, as expected, Q decreases with an increase in σ_3 for the material in the similar way. Incidentally, in case of analogue material, sudden decrease in Q corresponds to the data points beyond σ_3 (>0.7 MPa), which is due to the complete closure of e . The influence of σ_3 over Q is much more pronounced as compared to their counterparts 'natural material'. However, at higher σ_3 values σ_3 (>30 MPa), similar behavior can be observed from the plot, i.e., complete closure of the fracture at higher confining stress. As such, if the material properties are ignored, a perfect overlapping of the results would emerge.

Further, correlation between the analogue and natural materials has been established by plotting e against σ_3 , as depicted in Fig. 5-31. It can be observed from the figure that in general, e , decreases with an increase in σ_3 .

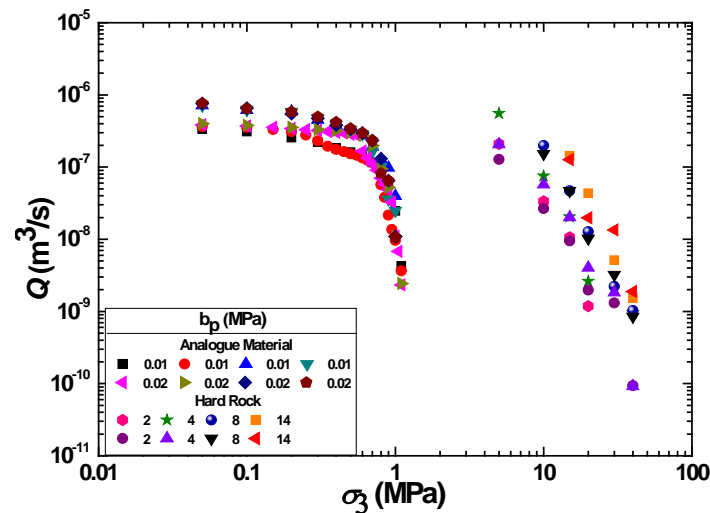


Fig. 5-30 The variation in discharge with confining pressure for correlation between analogue and natural material

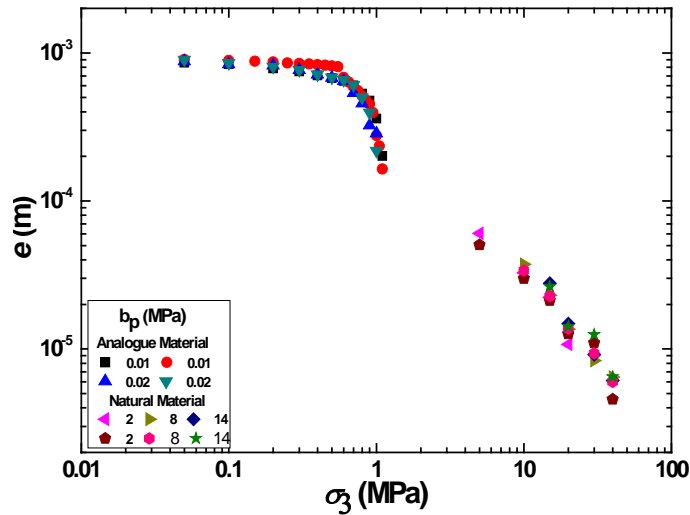


Fig. 5-31 The variation in hydraulic aperture with confining pressure for correlation between analogue and natural material

5.8 Relationship between σ_3 , b_p and Q

A critical analysis of the experimental results was done by employing Mathematica v. 7.0. A Non-linear Model Fit function was applied to derive the best possible relationship between σ_3 , b_p and Q , for analogue as well as natural samples as described in the following.

5.8.1 Analogue Material

From the obtained results of analogue sample (Fig. 5-4), a relationship is established between the σ_3 , b_p and Q_A , as represented in Eq. 5.2,

$$Q_A = X\sigma_3^a b_p^b \quad (5.2)$$

where Q_A is discharge through analogue sample, A, a and b are empirical constants and depend on the material properties.

Also, a relationship is established between the σ_3 , b_p , e , and Q_A , as represented in Eq. 5.3.

$$Q_A = X\sigma_3^a b_p^b e^c \quad (5.3)$$

where e , is the hydraulic aperture. The obtained values of the constants A, a, b, and c for Eq. 5.2 and 5.3, are listed in Table 5-4.

Table 5-4 The value of empirical constants appearing in Eq. 5.2 and 5.3

Equation	X	a	b	c
5.2	3.88×10^{-7}	-0.49	0.89	-
5.3	19.33	-0.017	0.99	2.85

5.8.2 Natural Material

From the obtained results of coarse, medium, and fine grained granite sample (Fig. 5-16), a relationship is established between the σ_3 , b_p and Q_R , by employing Mathematica v. 7.0, as represented in Eq. 5.4 ,

$$Q_R = A_1 \sigma_3^{a_1} b_p^{b_1} \quad (5.4)$$

where Q_R , is the discharge through the natural sample, A_1 , a_1 and b_1 are empirical constants and depend on the material and fracture properties. The obtained values of constants for all the samples are listed in Table 5-5.

Table 5-5 The value of empirical constants appearing in Eq. 5.4

Equation	Description of the grains	A_1	a_1	b_1
5.4	Coarse	1.04×10^{-5}	-3.04	1.42
	Medium	1.68×10^{-6}	-2.14	1.07
	Fine	4.48×10^{-6}	-2.03	0.93

CONCLUSION

In this study, attempts were made to develop a novel methodology to simulate flow of water through a fractured rockmass using an analogue material- 'Paraffin wax' imbibing a single fracture. Also, fluid flow properties of the naturally occurring granitic rock containing a 'single fracture' was also investigated under the varied conditions of confining pressure, groundwater pressure, and by changing the geometry of the fracture (length, width, and fracture roughness) by employing high pressure triaxial permeability tests apparatus. In addition, efforts were made to develop a test setup to determine the fluid flow properties of the rockmass under the laboratory conditions. Based on these studies, the following conclusions can be drawn.

1. The use of an analogue material- 'Paraffin wax' to create a cylindrical sample containing a 'single fracture' created with the help of sand grains to determining the fluid flow properties, can simulate the fluid flow conditions of the single fractured rockmass quite satisfactorily and was found useful, handy, and economical to use. This can be attributed to the fact that creation of fracture in the natural rock material as well as collection of undisturbed rock samples from the deep earth crust is quite difficult, tedious and time consuming and requires sophisticated and high pressure equipment. However, natural fractures are of varying thicknesses along the length and the width and therefore, the analogue material used in the present study are not truly representative of fractures seen in naturally fractured rocks. Further, the effect of the temperature on the fluid flow behaviour through analogue material has not been addressed in the present study as behaviour of wax is very sensitive to temperature.
2. The grains of the sands used for creating a fracture of certain aperture in sample made up of the analogue material, exhibit practically same elongation index, EI and the initial fracture aperture, e_i , is dependent on the EI and the arrangement of the sand grains. It can be attributed to the fact that arrangement of sand grains on the surface of the wax follows one of the hypothesized grain model, even the grains are affixed randomly.
3. Experimental observations of the fluid flow experiments on analogue material employing FWP demonstrate that as expected, Q decreases with an increase in σ_3 in a non-linear manner.

4. It can also be observed from the fluid flow experiments on analogue material that Q is function of σ_3 , b_p as well as e_i .
5. It has also been observed that due to the applied σ_3 , fracture with $e_i > 1.2$ mm, is more susceptible to closure than the fracture with $e_i \leq 1.2$ mm, corresponding to $b_p \leq 20$ kPa. The rapid reduction in Q corresponding to $\sigma_3 > 500$ kPa for $e_i > 1.2$ mm can be attributed, mainly, to an increase in grain-to-grain contact (which may also result in an increased tortuosity) and low values of base pressure, b_p .
6. Further, it has also been demonstrated that Reynolds number is quite sensitive to the fracture aperture and the base pressure, and there is a critical base pressure, beyond which transition in laminar to turbulent flow occurs.
7. High precision 3D laser scanning data has been found to be quite useful for quantifying the effect of fracture roughness and to further correlate the results of fluid flow experiments on the natural material.
8. Fluid flow experiments on a cylindrical sample of granite, containing a 'single rough walled fracture', were carried out by employing a high pressure (<60 MPa) triaxial permeability cell under varied conditions of confining pressures (which can simulate the condition occurring 1000 m below in the earth crust), elevated fluid pressures (≥ 25 MPa) and fracture roughness (by selecting different types of rocks based on their grain size) and the study has demonstrated that Q is quite sensitive to the confining pressure, the base pressure and the fracture roughness and there is a critical base pressure, beyond which the pressure gradient relationship starts behaving non-linearly. However, the present study could not demonstrate real-world flow problems involving multiple and inter-connected (and not connected) fractures.
9. Q decreases almost non-linearly with $\sigma_{eff.}$, and asymptote beyond certain critical $\sigma_{eff.} \geq 20$ MPa and $\sigma_{eff.} \geq 15$ MPa, for smaller and larger samples, respectively. Also, the variation in Q with $\sigma_{eff.}$, is less perceptible for coarse and medium grained samples, on the contrary, fine grained samples displays more discharge. It can be inferred that most part of the asperities come in contact with each other at higher effective stress and fluid flow through such fracture completely ceases and becomes a asymptote at a point of critical $\sigma_{eff.}$.

FUTURE SCOPE

The present study was an attempt to determine fluid flow characteristic of fractured rockmass by employing the flexible wall permeameter and high pressure triaxial cell, in tandem. To achieve this, different methodologies were developed and their utility has been demonstrated, primarily. However, the scope of the study can be extended by considering the following:

- For generalization of the findings, exhaustive investigations should be made with some other analogue materials.
- An effort should be made to determine the permeability of natural rock samples having different fracture density and orientation.
- Numerical simulation considering different geometry of single and multiple fractures and with different materials should be performed for better correlation.
- An attempt should be made to explore the use of centrifuge in determining the permeability of intact and fractured rockmass.

Appendix A Sample designation and geometrical detail of the analogue samples and the fracture, ($l=60$ mm, $W=34.5$ mm)

Sample	b_p (kPa)	d_i (mm)	d_f (mm)	e_i (mm)	A_{fi} (mm ²)
S-SG-425	10	34.78	35.71	0.93	32.09
	10	34.57	35.63	1.06	36.67
	20	34.75	35.90	1.15	39.68
	20	33.93	35.16	1.23	42.33
	30	34.77	35.77	1.00	34.50
	40	34.63	35.73	1.10	37.95
S-SG-500	10	34.82	36.08	1.26	43.37
	10	34.82	36.29	1.47	50.61
	10	34.43	35.63	1.19	41.19
	20	34.77	35.97	1.21	41.61
	20	34.74	35.96	1.23	42.30
	20	34.89	36.23	1.34	46.33
	30	34.63	35.87	1.23	42.57
	40	34.77	35.93	1.17	40.23
S-SG-710	10	34.79	36.50	1.70	58.79
	10	34.79	36.56	1.77	61.17
	10	34.87	36.50	1.62	56.03
	20	34.74	36.34	1.60	55.30
	20	34.73	36.38	1.65	56.93
	30	34.83	36.27	1.43	49.47
	30	34.65	36.57	1.92	66.34
	30	34.73	36.57	1.83	63.27
	40	34.73	36.39	1.66	57.27
	40	34.73	36.30	1.57	54.06

Appendix B Sample designation and geometrical detail of the samples and the fracture prepared using glass beads (l=60 mm, W=34.5 mm)

Sample	b_p (kPa)	d_i (mm)	d_f (mm)	e_i (mm)	A_f (mm ²)	e_c $2 \cdot d$ (mm)	e_c $d \cdot (1 + \cos 30^\circ)$ (mm)
S-GB-0.45	10	35.05	35.93	0.88	30.36	0.9	0.52
	10	34.74	35.58	0.84	28.98		
	20	34.74	35.57	0.83	28.63		
	20	34.77	35.61	0.84	28.98		
	30	34.71	35.45	0.74	25.53		
	40	34.64	35.47	0.83	28.63		
S-GB-1.00	10	34.7	36.22	1.52	52.44	2	1.15
	10	34.54	36.15	1.61	55.55		
	20	34.9	36.41	1.51	52.09		
	20	34.65	36.41	1.76	60.72		
	30	34.61	36.38	1.77	61.07		
	40	34.53	36.26	1.73	59.68		
S-GB-1.42	10	34.79	37.26	2.47	85.22	2.84	1.64
	10	34.79	37.2	2.41	83.15		
	20	34.7	37.18	2.48	85.56		
	20	34.69	37.14	2.45	84.53		
	30	34.97	37.25	2.28	78.66		
	40	35.11	37.36	2.25	77.63		
S-GB-1.85	10	34.82	37.69	2.87	99.01	3.74	2.16
	10	34.72	37.72	3	103.50		
	20	34.81	37.56	2.75	94.88		
	20	34.6	37.37	2.77	95.56		
	30	34.95	37.64	2.69	92.80		
	40	34.91	37.61	2.7	93.15		

Appendix C Computed Initial fracture aperture, e_c , of S-SG-425 based on grain model equations

S-SG-425					
l_1 (mm)	l_2 (mm)	EI	$2l_1$ (mm)	$l_1(1+EI)$ (mm)	$2l_2$ (mm)
0.90	0.55	0.60	1.81	1.45	1.09
0.72	0.57	0.79	1.45	1.30	1.14
0.94	0.64	0.68	1.88	1.58	1.28
0.70	0.60	0.85	1.40	1.30	1.20
0.75	0.62	0.83	1.51	1.38	1.25
0.66	0.54	0.82	1.33	1.21	1.09
0.81	0.64	0.79	1.62	1.45	1.28
0.68	0.57	0.84	1.35	1.24	1.13
0.81	0.74	0.91	1.63	1.56	1.49
0.69	0.54	0.78	1.38	1.22	1.07
0.87	0.46	0.53	1.73	1.32	0.91
0.84	0.55	0.65	1.68	1.39	1.10
0.83	0.61	0.74	1.66	1.44	1.22
0.63	0.55	0.86	1.27	1.18	1.09
0.82	0.57	0.70	1.64	1.39	1.14
0.67	0.50	0.75	1.33	1.17	1.00
0.64	0.47	0.74	1.27	1.11	0.94
0.67	0.60	0.90	1.34	1.27	1.20
0.78	0.50	0.64	1.56	1.28	1.00
0.68	0.46	0.68	1.35	1.14	0.92
0.66	0.65	0.98	1.32	1.31	1.30
0.70	0.48	0.68	1.40	1.18	0.95
0.67	0.55	0.82	1.35	1.23	1.11
0.65	0.56	0.86	1.31	1.22	1.13
0.73	0.57	0.78	1.47	1.30	1.14
0.67	0.59	0.87	1.35	1.26	1.18
0.74	0.52	0.70	1.48	1.26	1.04
0.77	0.56	0.73	1.54	1.33	1.12
0.79	0.52	0.65	1.59	1.31	1.03
0.67	0.57	0.85	1.35	1.24	1.14

Appendix D Computed Initial fracture aperture, e_c , of S-SG-500, based on grain model equations

S-SG-500					
l_1 (mm)	l_2 (mm)	EI	$2l_1$ (mm)	$l_1(1+EI)$ (mm)	$2l_2$ (mm)
1.15	0.87	0.75	2.30	2.01	1.73
0.83	0.68	0.82	1.66	1.51	1.37
1.03	0.67	0.65	2.06	1.70	1.35
1.13	0.90	0.79	2.27	2.03	1.80
1.33	0.65	0.49	2.67	1.99	1.31
0.93	0.76	0.82	1.86	1.69	1.52
0.94	0.79	0.85	1.87	1.73	1.59
1.02	0.52	0.51	2.04	1.54	1.04
1.07	0.88	0.82	2.15	1.95	1.75
1.10	0.69	0.63	2.20	1.79	1.39
1.19	0.81	0.68	2.37	1.99	1.61
0.95	0.79	0.83	1.89	1.73	1.57
0.92	0.71	0.77	1.84	1.63	1.41
0.88	0.61	0.69	1.76	1.49	1.22
0.74	0.70	0.94	1.48	1.44	1.39
1.12	0.68	0.61	2.25	1.81	1.36
1.28	0.83	0.64	2.57	2.11	1.66
0.95	0.90	0.94	1.90	1.85	1.80
0.94	0.73	0.78	1.88	1.67	1.47
0.91	0.81	0.90	1.81	1.72	1.63
1.01	0.76	0.75	2.03	1.77	1.51
1.41	0.68	0.48	2.81	2.08	1.36
0.81	0.67	0.82	1.62	1.48	1.34
0.82	0.76	0.92	1.64	1.58	1.51
1.03	0.90	0.87	2.06	1.93	1.80
0.96	0.77	0.80	1.91	1.72	1.53
1.36	0.61	0.45	2.72	1.97	1.22
1.13	0.64	0.57	2.25	1.76	1.28
0.93	0.83	0.89	1.86	1.76	1.66
0.92	0.89	0.97	1.83	1.81	1.78

Appendix E Computed Initial fracture aperture, e_c , of S-SG-710 based on grain model equations

S-SG-710					
l_1 (mm)	l_2 (mm)	EI	$2l_1$ (mm)	$l_1(1+EI)$ (mm)	$2l_2$ (mm)
1.73	0.76	0.44	3.46	2.49	1.52
1.22	0.84	0.69	2.44	2.06	1.68
1.41	0.85	0.60	2.83	2.26	1.70
1.33	0.89	0.67	2.65	2.22	1.78
1.16	0.81	0.69	2.33	1.97	1.61
1.31	0.95	0.72	2.63	2.26	1.90
1.46	0.69	0.47	2.91	2.14	1.37
1.18	0.87	0.73	2.37	2.05	1.73
1.41	1.11	0.79	2.82	2.52	2.22
1.29	0.84	0.65	2.59	2.14	1.68
1.12	0.79	0.71	2.25	1.92	1.59
1.05	0.91	0.87	2.10	1.96	1.82
1.28	0.78	0.61	2.56	2.06	1.57
1.10	1.03	0.94	2.20	2.13	2.06
0.91	0.88	0.96	1.83	1.79	1.76
1.14	0.88	0.77	2.27	2.02	1.76
1.14	0.88	0.77	2.29	2.02	1.75
1.15	0.90	0.79	2.30	2.05	1.80
1.06	0.71	0.67	2.12	1.77	1.43
1.13	0.91	0.80	2.27	2.04	1.82
1.41	0.95	0.68	2.82	2.36	1.91
1.14	0.86	0.75	2.29	2.00	1.72
1.23	0.93	0.75	2.46	2.16	1.85
1.12	0.85	0.76	2.24	1.97	1.71
1.52	0.76	0.50	3.05	2.29	1.53
1.11	0.85	0.77	2.21	1.96	1.70
1.45	0.91	0.63	2.90	2.36	1.82
0.90	0.73	0.81	1.80	1.63	1.46
1.14	0.79	0.69	2.28	1.93	1.58
1.68	0.82	0.49	3.36	2.50	1.64

Appendix F A typical datasheet used for recording experimental observations (for S-SG-425, $e_i=1.06 \times 10^{-3}$ m, $b_p=10$ kPa, Trial 1)

w_f (m) =	0.035	l_f (m) =	0.06	d_p (m) =1.02			ρ (kg/m ³) = 1000		μ (Pa.S) = 0.00089	
σ_3 (kPa)	t (s)	h_1	h_2	Q (cc)	($\times 10^{-7}$ m ³ /s)			($\times 10^{-5}$ m)	($\times 10^{-3}$ m)	R_e
					Q	ΔQ_s	ΔQ_i	e	e_a	
50	29	9.56	10	9.78	3.37	-	-	8.56	0.97	10.95
100	31	9.9	10	9.95	3.21	0.16	0.16	8.42	0.98	10.42
150	32	9.94	10	9.97	3.12	0.09	0.26	8.33	0.98	10.12
200	39	9.62	10	9.81	2.52	0.60	0.86	7.76	0.98	8.17
250	43	9.92	10	9.96	2.32	0.20	1.06	7.55	0.98	7.52
300	46	9.57	10	9.78	2.13	0.19	1.25	7.34	0.99	6.91
350	48	9.81	10	9.90	2.06	0.06	1.31	7.26	0.99	6.70
400	56	9.88	10	9.94	1.78	0.29	1.60	6.91	0.99	5.76
450	58	9.7	10	9.85	1.70	0.08	1.67	6.81	0.99	5.51
500	60	9.76	9.9	9.83	1.64	0.06	1.73	6.73	0.99	5.32
550	65	9.96	10	9.98	1.54	0.10	1.84	6.58	0.99	4.99
600	69	9.6	9.94	9.77	1.42	0.12	1.96	6.41	1.00	4.60
650	73	9.8	10	9.9	1.36	0.06	2.02	6.32	1.00	4.40
700	81	9.9	10	9.95	1.23	0.13	2.14	6.11	1.00	3.99
750	102	9.78	10	9.89	0.97	0.26	2.40	5.65	1.00	3.15
800	127	9.87	10	9.93	0.78	0.19	2.59	5.26	1.01	2.54
850	153	9.95	10	9.97	0.65	0.13	2.72	4.95	1.01	2.12
900	170	9.74	10	9.87	0.58	0.07	2.79	4.76	1.01	1.89
950	270	9.54	9.6	9.57	0.35	0.23	3.02	4.04	1.02	1.15
1000	346	9.58	9.76	9.67	0.28	0.07	3.09	3.73	1.02	0.91
1050	900	5.14	5.1	5.12	0.06	0.22	3.32	2.19	1.04	0.18

Appendix G A typical datasheet used for recording experimental observations (for S-GB-0.45 ($e_i=0.88 \times 10^{-4}$ m, $b_p=10$ kPa, Trial 1))

	w_f (m) =	0.0345	l_f (m) =	0.06	d_p (m) =	1.02	ρ (kg/m ³)	1000	μ (Pa.S)	0.00089
σ_3 (kPa)	t (sec)	h_1	h_2	Q (cc)	$(\times 10^{-7} \text{m}^3/\text{s})$			$(\times 10^{-5} \text{m})$	$(\times 10^{-4} \text{m})$	R_e
					Q	ΔQ_i	ΔQ_s	e	e_a	
0								88.00		
50	29	9.86	10	9.93	3.42			8.61	7.94	11.151728
100	34	9.96	10	9.98	2.94	0.49	0.48	8.18	7.98	9.5596617
200	39	9.84	10	9.92	2.54	0.88	0.39	7.80	8.02	8.2839594
300	53	9.98	10	9.99	1.88	1.54	0.65	7.06	8.09	6.1387581
400	87	9.92	10	9.96	1.14	2.28	0.74	5.98	8.20	3.7284728
600	195	9.96	10	9.98	0.51	2.91	0.63	4.57	8.34	1.6668128
800	900	6.84	6.88	6.86	0.08	3.35	0.43	2.42	8.56	0.2482404
900	900	2.96	3.08	3.02	0.03	3.39	0.04	1.84	8.62	0.1092837

Appendix H The computed e_a and Q_{sf} values corresponding to different e_i for $b_p (= 10 \text{ kPa})$

Sample	b_p (kPa)	e_i (mm)	$e_a (\times 10^{-4} \text{ m})$		$Q_{sf} (\times 10^{-7} \text{ m}^2/\text{s})$		σ_3 (kPa)	
			Min	Max.	Min	Max.	Min	Max.
S-SG-425	10	0.9	8.46	8.81	3.12	0.62	50	900
		1.0	9.74	10.11	3.30	0.35	50	950
		1.2	11.01	11.51	3.77	0.32	50	950
S-SG-500		1.3	11.70	11.88	3.90	1.95	50	700
		1.5	13.76	14.01	4.41	1.73	50	700
		1.6	15.25	15.63	4.52	0.97	50	700
S-SG-710		1.8	16.04	16.19	4.64	2.76	50	500
		1.9	16.73	17.09	4.83	1.20	50	500

Appendix I Typical datasheet used for recording experimental observations and calculated parameters for natural sample, S1-CG-38

S.No.	t (sec)	w (g)	Δw (g)	Q (g/sec)	Q (ml/s)	Q (m ³ /sec)
1	3	11.56	0.09	0.030	0.030	3.00E-08
2	6	11.65	0.11	0.037	0.037	3.67E-08
3	9	11.76	0.06	0.020	0.020	2.00E-08
4	12	11.82	0.09	0.030	0.030	3.00E-08
5	15	11.91	0.08	0.027	0.027	2.67E-08
6	18	11.99	0.07	0.023	0.023	2.33E-08
7	21	12.06	0.18	0.060	0.060	6.00E-08
8	24	12.24	0.14	0.047	0.047	4.67E-08
9	27	12.38	0.17	0.057	0.057	5.67E-08
10	30	12.55	0.16	0.053	0.053	5.33E-08
11	33	12.71	0.22	0.073	0.073	7.33E-08
12	36	12.93	0.19	0.063	0.063	6.33E-08
13	39	13.12	0.22	0.073	0.073	7.33E-08
14	42	13.34	0.21	0.070	0.070	7.00E-08
15	45	13.55	0.2	0.067	0.067	6.67E-08
16	48	13.75	0.24	0.080	0.080	8.00E-08
17	51	13.99	0.23	0.077	0.077	7.67E-08
18	54	14.22	0.23	0.077	0.077	7.67E-08
19	57	14.45	0.25	0.083	0.083	8.33E-08
20	60	14.7	0.24	0.080	0.080	8.00E-08
21	63	14.94	0.24	0.080	0.080	8.00E-08
22	66	15.18	0.25	0.083	0.083	8.33E-08
23	69	15.43	0.23	0.077	0.077	7.67E-08
24	72	15.66	0.26	0.087	0.087	8.67E-08
25	75	15.92	0.25	0.083	0.083	8.33E-08
26	78	16.17	0.27	0.090	0.090	9.00E-08
27	81	16.44	0.31	0.103	0.103	1.03E-07
28	84	16.75	0.27	0.090	0.090	9.00E-08
29	87	17.02	0.12	0.040	0.040	4.00E-08
30	90	17.14	0.06	0.020	0.020	2.00E-08
31	93	17.2	0.73	0.243	0.243	2.43E-07
32	96	17.93	0.41	0.137	0.137	1.37E-07
33	99	18.34	0.3	0.100	0.100	1.00E-07
34	102	18.64	0.33	0.110	0.110	1.10E-07
35	105	18.97	0.34	0.113	0.113	1.13E-07

**Appendix J The measured and calculated parameters for natural samples,
S1-CG-38**

ρ (kg/m ³)	997.05		μ (kg/m.S)	8.90×10 ⁻⁴	
d (m)	3.97×10 ⁻⁰²		l (m)	7.62×10 ⁻⁰²	
σ_3 (MPa)	b_p (MPa)	$\sigma_{eff.}=(\sigma_3-b_p)$ (MPa)	$Q_{Exp.}$ (×10 ⁻⁸ m ³ /s)	$e_{cal.}$ (×10 ⁻⁵ m)	$R_{e cal.}$
5	1	4	8.63	1.21	2.44
	2	3	20.88	1.29	5.90
	3	2	35.84	1.35	10.12
	4	1	57.14	1.43	16.14
10	1	9	2.29	0.78	0.65
	2	8	3.35	0.70	0.95
	4	6	7.51	0.73	2.12
	6	4	13.14	0.77	3.71
	8	2	19.88	0.80	5.62
15	2	13	1.08	0.48	0.31
	4	11	2.04	0.47	0.58
	6	9	3.39	0.49	0.96
	8	7	4.71	0.49	1.33
	10	5	6.77	0.52	1.91
	14	1	14.29	0.59	4.04
20	2	18	0.15	0.25	0.04
	4	16	0.25	0.23	0.07
	8	12	0.99	0.29	0.28
	10	10	1.22	0.29	0.34
	14	6	2.17	0.32	0.61
	18	2	4.12	0.36	1.16
30	2	28	0.14	0.24	0.04
	4	26	0.20	0.22	0.06
	8	22	0.27	0.19	0.08
	14	16	0.59	0.20	0.17
	18	12	0.88	0.22	0.25
	25	5	1.72	0.24	0.49
40	2	38	0.10	0.21	0.03
	4	36	0.10	0.17	0.03
	8	32	0.13	0.15	0.04
	14	26	0.20	0.14	0.06
	18	22	0.27	0.14	0.08
	25	15	0.48	0.16	0.14

REFERENCES

1. Arulanandan, K., Thompson, P. Y., Kutter, B. L., Meegoda, N. J., Muraleetharan, K. K., and Yogachandran, C., (1988) Centrifuge Modeling of Transport Processes for Pollutants in Soils, *J. Geotech. Eng.-Ascel*, Vol. 114(2), pp. 185–205.
2. ASTM Standards D 4543-08, (2008) Standard Practices for Preparing Rock Core as Cylindrical Test Specimens and Verifying Conformance to Dimensional and Shape Tolerances, ASTM International, West Conshohocken, Pennsylvania (PA), USA, Vol. 4 (8), pp. 1-9. doi.10.1520/D4543-08.
3. ASTM Standards D-5084-03, (2004) Standard test methods for measurement of hydraulic conductivity of saturated porous materials using a flexible wall permeameter, ASTM International, West Conshohocken, Pennsylvania (PA), USA, Vol. 08 Soil and Rock (I): D420 - D5876, pp. 1-23.
4. Balberg, I. and Binenbaum, N., (1983) Computer study of the percolation threshold in a two-dimensional anisotropic system of conducting sticks. *Phys. Rev.*, Vol. B (28), pp. 3799-3812.
5. Bandis S. C., Lumsden A. C. and Barton N. R., (1983) Fundamentals of rock joint deformation. *Int. J. Rock Mech. Sci. & Geomech. Abstr.*, Vol. 20, 249p.
6. Bartake, P.P., Patel, A. and Singh, D.N., (2008) Instrumentation for Bender Element Testing of Soils, *International Journal of Geotechnical Engineering*, Vol. 2(4), pp. 395-405.
7. Barton, N.R., Lien, R. and Lunde, J. (1974) Engineering classification of rock masses for the design of tunnel support. *Rock Mech.* Vol. 6(4), pp. 189-239.
8. Bear, J., Tsang, C.F., and de Marsily, D., (1993) Flow and Contaminant *Transport in Fractured Rock*. Academic Press, New York, 560pp.
9. Bernabe, Y., (1988) Comparison of the effective pressure law for permeability and resistivity formation factor in Chelmsford granite, *PAGEOPH*, Vol.127, pp. 607-625.
10. Bieniawski, Z.T. (1973) Engineering classification of jointed rock masses. *Trans S. Afr. Inst. Civ. Engrs* Vol. 15, pp. 335-344.
11. Bieniawski, Z.T. (1976) Rock mass classification in rock engineering. *In Exploration for rock engineering, proc. of the symp.*, (ed. Z.T. Bieniawski) Cape Town: Balkema, Vol. 1, pp. 97-106.
12. Bieniawski, Z.T. (1989) Engineering rock mass classifications. New York: Wiley.

13. Boadu, F. K., (1997) Fractured rock mass characterization parameters and seismic properties: analytical studies. *J. Appl. Geophys.*, Vol. 36, pp. 1–19.
14. Brace, W. F., Walsh J. B., and Frangos W. T., (1968) Permeability of granite under high pressure, *J. Geophys. Res.*, Vol. 73, 2225p.
15. Brace, W. F. (1978) A note on permeability changes in geologic material due to stress. Pageoph, Birkhauser Verlag, Basel, Vol. 116, pp. 627-633.
16. Brady, B.H.G. and Brown, E.T., (2006) Rock mechanics for underground mining, 3rd ed. Springer, 626p.
17. Brown S. R., (1987) Fluid flow through rock joints: the effect of surface roughness. *J. Geophys. Res.* Vol. 92, pp. 1337-1347.
18. Brown, S.R. and Scholz C. H., (1985) Broad bandwidth study of the topography of natural rock surfaces. *J. Geophys. Res.* Vol. 90, pp. 12575- 12582.
19. Brown, S.R., Caprihan, A., and Hardy, R., (1998), Experimental observation of fluid flow channels in a single fracture, *J. Geophys. Res.* Vol. 103, (B3), pp. 5125-5132.
20. Chen Yifeng, Zhou Chuangbing, and Sheng, Yongqing, (2007) Formulation of strain-dependent hydraulic conductivity for a fractured rock mass, *Int. J. Rock Mech. Min. Sci.*, Vol. 44, pp. 981–996.
21. Cook, N.G.W. (1992) Natural joints in rock: mechanical, hydraulic and seismic behavior and properties under normal stress, *Int. J. Rock Mech. Min. Sci. Geomech. Abstr.* Vol. 29, pp. 198-223.
22. Cord, A., et al., (2007) Surface roughness and geological mapping at subhectometer scale from the High Resolution Stereo Camera onboard Mars Express, DOI: 10.1016/j.icarus.2007.04.029, *Icarus*, Vol. 191(1), pp. 38-51.
23. Deere, D.U., Hendron, A.J., Patton, F.D. and Cording, E.J. (1967) Design of surface and near surface construction in rock. *In Failure and breakage of rock, proc. 8th U.S. symp. rock mech.*, (ed. C. Fairhurst), 237-302. New York: Soc. Min. Engrs, Am. Inst. Min. Metall. Petrolm Engrs.
24. Eid Hisham T., (2007) A technique for estimating permeability of a randomly fractured rock mass. *Acta Geotechnica*, Vol. 2, pp. 97–102.
25. Engelder T. and Scholz C. H. (1987) Fluid flow along very smooth joints at effective pressures up to 200 megapascals. *In Mechanical Behavior of Crustal Rocks, Am. Geophys. Union Monograph No. 24*, 147p.

26. Fecker, E. & Rengers N. (1971) Measurement of large scale roughness of rock planes by means of profilograph and geological compass. *Rock Fracture, Proc. of Int. Symp. Rock Mech.* Nancy, pp. 1-18.
27. Gangi, A. F., (1978) Variation of whole and fractured porous rock permeability with confining pressure. *Int. J. Rock Mech. Min. Sci. & Geomech. Abstr.*, Vol. 15/5, pp. 249– 257.
28. Gangi, A.F., and Richard, L.C., (1996) An asperity-deformation model for effective pressure. *Tectonophysics*, Vol. 256, pp. 241-251.
29. Gere, J. M., and Timoshenko, S. P., (1987) *Mechanics of Materials*. Van Nost. Reinhold, U.S., ISBN-13.
30. Giacomini, A., Buzzi, O., Ferrero, A.M., Migliazza M., and Giani G.P., (2008), Numerical study of flow anisotropy within a single natural rock joint, *Int. J. Rock Mech. Min. Sci.*, Vol. 45, pp. 47-58.
31. Goodman, R. E., (1976) *Methods of Geological Engineering in Discontinuous Rocks*. West New York.
32. Gowd, T.N., and Rummel, F., (1980) Effect of Confining Pressure on the fracture behavior of a porous rock. *Int. J. Rock Mech. Min. Sci. & Geomech. Abstr.*, Vol. 17, pp. 225-229.
33. Guerrero C., Reyes, E., and Gonzalez, V., (2002) Fracture surface of plastic materials: the roughness exponent. *Polymer* Vol. 43, pp. 6683–6693.
34. Haberfield, C. M, Johnston, I. W., (1994) A mechanistically-based model for rough rock joint. *Int. J. Rock Mech. Min. Sci. Geomech. Abstr.*, Vol. 31(4), pp. 279–292.
35. Hakami, E., and Larsson, E., (1996) Aperture measurements and flow experiments on a single natural fracture, *Int. J. Rock Mech. Min. Sci. & Geomech. Abstr.*, Vol. 33, (4), pp. 395-404.
36. Hans J. (2002), *Etude expérimentale et modélisation numérique multiéchelle du comportement hydromécanique des répliques de joints rocheux*, PhD thesis, Joseph Fourier University, Grenoble, France.
37. Hassanizadeh, S. M. and Gray, W. G., (1987) High velocity flow in porous media. *Transport in Porous Media*, Vol. 2, pp. 521–531.
38. Hoek, E., (1994) Strength of rock and rock masses, *ISRM News Journal*, 2(2), 4-16.

39. Hsieh, P.A. and Neuman, S.P., (1985), Field determination of the three dimensional hydraulic conductivity tensor of anisotropic media, 1, Theory: *Water Resour. Res.*, Vol. 21, (11), pp. 1655- 1665.
40. Hugh, M., Huang, C., Dash, Z., Zyvoloski, G., and White, A., (2004) Semianalytical solutions for fluid flow in rock joints with pressure-dependent openings. *Water Resour. Res.*, Vol. 40, pp. 1-16.
41. Indraratna, B., Ranjith, P.G., and Gale W., (1999) Single phase water flow through rock fractures, *Geotechnical and Geological Engineering* Vol. 17, pp. 211–240.
42. Indraratna, B., Ranjith, P. G., Price, J. R., and Gale, W., (2003) Two-phase (air and water) flow through rock joints: analytical and experimental study. *J. Geotech Geoenviron* (ASCE), Vol. 129 (10), pp. 918-928.
43. Inoue, I., and Sugita, H., (2003) Fourth-order approximation of fluid flow through rough-walled rock fracture. *Water Resour. Res.*, Vol. 39 (8), pp. 1-10.
44. ISRM (1981) Rock Characterization, Testing and Monitoring, ISRM suggested methods. Ed. E.T. Brown. Pergamon Press, Oxford.
45. ITSCA, Itasca Consulting Group (1996) User's manuals: version 3.0, Vol. 1, 2 and 3. UDEC-Universal Distinct Element Code, USA.
46. Iwai, K, (1976) Fundamental studies of fluid flow through a single fracture. PhD thesis, University of California, Berkeley.
47. Jones, F. O., (1975) A laboratory study of the effects of confining pressure on fracture flow and storage capacity in carbonate rocks. *J. Petrol.*, pp. 21– 27.
48. Jones, F. O., and Owens, W. W., (1980) A laboratory study of low permeability gas sands. *Soc. Pet. Eng. J.*, Vol. 32, pp. 1631–1640.
49. Kahraman S (2001) A correlation between P-wave velocity, number of joints and Schmidt hammer rebound number. *Int. J. Rock Mech. Min. Sci.*, Vol. 38, pp. 729–733.
50. Kahraman S (2002) The effects of fracture roughness on P-wave velocity. *Eng Geol* Vol. 63, pp. 347–350.
51. Kahraman, S., Soylemez, M. and Fener, M., (2008) Determination of fracture depth of rock blocks from P-wave velocity. *Bull Eng Geol Environ*, Vol. 67, pp. 11–16.
52. Kim, Hyung-Mok, Inoue, Junya, and Horii, Hideyuki, (2004) Flow analysis of jointed rock masses based on excavation-induced transmissivity change of rough joints. *Int. J. Rock Mech. Min. Sci.*, Vol. 41, pp. 959–974.

53. Koura, M. M., and Omar, M. A., (1981) The effect of surface parameters on friction. *Wear* Vol. 73(2), pp. 235–246.
54. Krahn, J., Morgenstern N.R., (1979) The ultimate frictional resistance of rock discontinuities. *Int J Rock Mech Min Sci*, Vol. 16, pp. 127-133.
55. Kranz, R.L, Frankel A.D, Engelder T, Scholz C.H., (1979) The permeability of whole and jointed barre granite. *Int. J. Rock Mech. Min. Sci. & Geomech Abstr.*, Vol.16: pp. 225-34.
56. Krumbein, W.C., and Pettijohn, E.T., (1938) *Manual of Sedimentary Petrography*, Appleton-Century-Crofts: New York.
57. Lanaro, F. (2000) A random field model for surface roughness and aperture of rock fractures. *Int. J. Rock Mech. Min. Sci. & Geomech. Abstr.*, Vol. 37, pp. 1195-1210.
58. Li, S. P., Li, Y. S., Li, Y., Wu Z. Y., and Zhou, G., (1994) Permeability-strain equations corresponding to the complete stress– strain path of Yinzhuang sandstone. *Int. J. Rock Mech. Min. Sci. & Geomech. Abstr.*, Vol. 31/4, pp. 383– 391.
59. Li, S. P., Wu, D. X., Xie, W. H., Li, Y. S., Wu Z. Y., Zhou, G., and Zhao H. Y., (1997) Effect of confining pressure, pore pressure and specimen dimension on permeability of Yinzhuang sandstone. *Int. J. Rock Mech. & Min. Sci.*, Vol. 34 (3-4) No. 175.
60. Li, C., Prikryl, R., and Nordlund E., (1998) The stress-strain behavior of rock material related to fracture under compression. *Engineering Geology*, Vol. 49, pp. 293-302.
61. Lomize G. M., (1951) *Water flow through jointed rock*. Moscow: *Gosenergoizdat*, (in Russian).
62. Long, J. C. S., Remer, J. S., Wilson, C. R., and Witherspoon, P. A., (1982) Porous media equivalents for networks of discontinuous fractures. *Water Resour. Res.*, Vol. 18, pp. 645-658.
63. Louis, C., (1969) *A Study of Groundwater Flow in Jointed Rock and its Influence on the Stability of Rock Masses*. Imperial College Rock Mechanics Research Report No. 10, 90 p.
64. Marshak, S., and Mitra, G., (1988) *Basic methods of structural geology*, Englewood Cliffs, New Jersey, Prentice-Hall, 445 p.
65. Marsily, Ghislain, (1986) *Quantitative Hydrogeology: Groundwater Hydrology for Engineers*, Academic Press, N.Y.
66. Mellott, N.P., Brantley, S.L., Hamilton, J.P., and Pantano, C.G., (2000) Evaluation of surface preparation methods for glass. *Surf. Interface Anal.* 2001; 31: pp. 362–368.

67. Min, Ki-Bok, Rutqvist, Jonny, and Elsworth, Derek, (2009) Chemically and mechanically mediated influences on the transport and mechanical characteristics of rock fractures. *Int. J. Rock Mech. Min. Sci.*, Vol. 46, pp. 80-89.
68. Neuman, S.P., (1987) Stochastic continuum representation of fractured rock permeability as an alternative to the REV and fracture network concept Rock Mechanics, *Proc. of the 28th U.S. Rock Mech. Symp.*, A.A. Balkema, Rotterdam, pp. 533-561.
69. Neuzil, C. E., and J. V. Tracy, (1981) Flow through fractures, *Water Resour. Res.*, Vol. 17(1), pp. 191-199.
70. Nicholl, M.J. and R.L. Detwiler, (2001) Simulation of flow and transport in a single fracture: Macroscopic effects of underestimating local head loss, *Geophysical Research Letters*, Vol. 28(23) pp. 4351-54.
71. Oda M., (1985) Permeability tensor for discontinuous rock mass. *Geotechnique*, Vol. 35(4), pp. 483-495.
72. Oda, M., Yamabe, T., and Kamemura, K., (1986) A crack tensor and its relation to wave velocity anisotropy in jointed rock masses. *Int. J. Rock Mech. Min. Sci. Geomech. Abstr.*, Vol. 23, pp. 387-397.
73. Olsson R, Barton N.R., (2001) An improved model for hydromechanical coupling during shearing of rock joints. *Int. J Rock Mech. Min. Sci.*, Vol. 38 (3), pp. 317-329.
74. Oron AP, Berkowitz B., (1998) Flow in fractures: the local cubic law assumption reexamined. *Water Resour. Res.*, Vol. 34(11), pp. 2811-2825.
75. Palmstrom A., (1995) RMi – a rock mass characterization system for rock engineering purposes. PhD thesis, University of Oslo, Department of Geology, 400 p.
76. Pantelidis, L., (2009) Rock slope stability assessment through rockmass classification systems. *Int. J. Rock Mech. and Min. Sci.*, Vol. 46, pp. 315-325.
77. Patel, A., Bartake, P.P., and Singh, D. N., (2009) An Empirical Relationship for Determining Shear Wave Velocity in Granular Materials Accounting for Grain Morphology, *Geotechnical Testing Journal*, ASTM, Vol. 32(1), pp. 1-10.
78. Pariseau, W. G., S. C. Schmelter and Sheik, A. K., (1997) Mine slope stability analysis by coupled finite element modelling, *Int. J Rock Mech. & Min. Sci.*, Vol. 34, 3-4, No. 242.
79. Pratt, H. R., Black, A. D., Brace, W. F. and Swolfs, H., (1977) Elastic and transport properties of an in-situ jointed granite. *Int. J. Rock Mech. & Min. Sci.*, Vol. 14, 35.

80. Pyrak-Nolte, L.J., Myer, L.R., Cook, N.G.W. and Witherspoon, P.A., (1987) Hydraulic and mechanical properties of natural fractures in low permeability rock. *In Proceeding of the Sixth International Congress on Rock Mechanics*, edited by G. Herget and S. Vongpaisal, A.A. Balkema, Brookfield Vt., pp. 225-231.
81. Pyrak-Nolte, L.J. and Cook, N.G.W., (1988) Fluid percolation through single fractures, *Geophysical Research Letters*, Vol. 15, (11), pp. 1247-1250.
82. Qian, J., Chen, Z., Zhan, H., and Guan H., (2011) Experimental study of the effect of roughness and Reynolds number on fluid flow in rough-walled single fractures: a check of local cubic law. *Hydrol. Process.* Vol., 25, pp. 614–622.
83. Ramsay, J.G. (1980) Shear zone geometry: a review, *Journal of Structural Geology* 2, pp. 83–99.
84. Ranjith, P.G., (2010) An experimental study of single and two-phase fluid flow through fractured granite specimens. *Environ Earth Sci.*, Vol. 59, pp. 1389-1395.
85. Ranjith, P.G. and Viete, D.R. (2011) Applicability of the ‘cubic law’ for non-Darcian fracture flow. *Journal of Petroleum Science and Engineering* Vol. 78, pp. 321-327.
86. Raven, K. G. and Gale, J. E., (1985) Water flow in natural rock fractures as a function of stress and sample size. *Int. J. Rock Mech. Min. Sci. & Geomech. Abstr.*, Vol. 22 (4), pp. 251-261.
87. Reeves, M. J., (1985) Rock surface roughness and frictional strength. *Int. J. Rock Mech. Min. Sci. & Geomech. Abstr.*, Vol. 22(6), pp. 429-442.
88. Riley, N. Allen, (1941) Projection sphericity, *Journal of Sedimentary Research*; August 1941; Vol. 11(2), pp. 94-95.
89. Rissler, P., (1978) Determination of the water permeability of jointed rock. Ins. Foun. Eng. Soil Mech. Rock Mech., and Water Ways Const., University of Aachen, Federal Republic of Germany, 150 p.
90. Rengers, N., (1970) Influence of surface roughness on the friction properties of rock planes. *Proc. 2nd Cong. Int. Soc. Rock Mech.*, Belgrad, Vol. I, pp.229-234.
91. Robinson, D.A. and Friedman S.P., (2002) Observations of the effects of particle shape and particle size distribution on avalanching of granular media. *Physica A. Statistical Mechanics and its Applications*, Vol. 311, pp. 97-110.
92. Romana, M., (1985) New adjustment ratings for application of Bieniawski classification to slopes, *Int. Symp., on the role of rock mechanics*, ISRM. Zacatecas, pp. 49-53.

93. Rutqvist, J., Barrb, D., Dattac, R., Gensd, A., Millarde, A., Olivellad, S., Tsang, C. F., and Tsang, Y., (2005) Coupled thermal–hydrological–mechanical analyses of the Yucca Mountain Drift Scale Test—Comparison of field measurements to predictions of four different numerical models, *Int. J. Rock Mech. Min. Sci.*, Vol. 42, pp. 680–697.
94. Samingan, A.S., E. Leong, and H. Rahardjo, (2003) A flexible wall permeameter for measurement of water and air coefficients of permeability of residual soils. *Can. Geotech. J.* Vol. 40 (3), pp. 559-574.
95. Schrauf, T. W., and D. D. Evans, (1986) Laboratory studies of gas flow through a single natural fracture, *Water Resour. Res.*, Vol. 22, (7), pp. 1038-1050.
96. Shimo, M. and Long, J., (1987) A numerical study of transport parameters in fracture networks. In: D.D. Evans and T.J. Nicholson (Editors), Flow and transport through unsaturated rock. *Am. Geophys. Union, Geophys. Monogr.*, Vol. 42, pp. 121-131.
97. Shiotani, T., (2006) Evaluation of long-term stability for rock slope by means of acoustic emission technique, *NDT&E International*, Vol. 39, pp. 217-228.
98. Singh, R. N., and Gahrooe , D. R., (1990) Deterministic stability and sensitivity analyses of slopes in jointed rock masses, *Mining Science and Technology*, Elsevier Science, Vol.10, pp. 265-286
99. Snow, D.T., (1965) A parallel plate model of fractured permeable media. PhD Thesis, Univ of California.. 331 p.
100. Snow, D.T., (1969) Anisotropic permeability of fractured media. *Water Resour. Res.*, Vol. 5(6), pp. 1273-1289.
101. Somerton, W. H., Soylemezoglu, I.M., and Dudley, R.C., (1975) Effect of stress on permeability of coal. *Int. J. Rock Mech. Min. Sci. & Geomech. Abstr.*, Vol. 12, pp. 241-251.
102. Sour, L., and Ubbes, W., (1987) Fracture flow response to applied stress: a field study. In Proceedings of the 28th U.S. Symposium Rock Mechanics, ed. I.W. Farmer, J.J.K. Dacmen, C.S. Desai, and S.P. Neuman,. Tucson, Arizona. New York: Routledge, pp. 501-508.
103. Suthaker, N.N., and Scott, J.D. (1996) Measurement of hydraulic conductivity in oil sand tailings slurries, *Can. Geotech. J.*, 33(4), pp. 642-653.
104. Taylor, R.N., (1995) Geotechnical Centrifuge Technology, Blackie Academic and Professional.
105. Tempone, P., Lavrov, A., (2008), DEM modelling of mudlosses into single fractures and fracture networks, The 12th International Conference of *International*

- Association for Computer Methods and Advances in Geomechanics (IACMAG)*, Goa, India, pp. 2475-2482.
106. Terzaghi, K. (1946) Rock defects and loads on tunnel supports. In *Rock tunneling with steel supports*, (eds R. V. Proctor and T. L. White). Youngstown, OH: Commercial Shearing and Stamping Company, Vol. 1, pp. 17-99.
 107. Thompson ME, Brown SR. (1991) The effect of anisotropic surface roughness on flow and transport in fractures, *J Geophys. Res.* Vol. 96 (B13), pp. 21923-21932.
 108. Tsang, Y.W, and Witherspoon P.A., (1981) Hydromechanical behavior of a deformable rock fracture subject to normal stress. *J Geophys. Res.* Vol. 86, pp. 9287-9298.
 109. Tsang, Y W; Witherspoon, Paul A., (1983) The dependence of fracture mechanical and fluid flow properties on fracture roughness and sample size. *J Geophys. Res B*, Vol. 88 (3), pp. 2359-2366.
 110. Tsang, Y.W., (1984) The effect of tortuosity on fluid flow through a single fracture. *Water Resour. Res.*, Vol. 20 (9), pp. 1209-1215.
 111. Tsang, Y.W., (1992) Usage of “equivalent apertures” for rock fractures as derived from hydraulic and tracer tests, *Water Resour. Res.*, Vol. 28, pp. 1451-1455.
 112. Tse, R. and Cruden, D.M., (1979) Estimating joint roughness coefficients, *Int. J. Rock Mech. Min. Sci. & Geomech. Abstr.*, 16, pp. 303-307.
 113. Vasconcelos, G., Lourenço, P.B., and Costa, M.F.M., (2006) Characterization of the fracture surfaces obtained in direct tensile tests. 10th Portuguese Conference on Fracture.
 114. Wadell H., (1935) Shape and Roundness of Quartz Particles. *J. Geol.*, p. 250.
 115. Walsh, J. B., (1981), Effect of pore pressure and confining pressure on fracture permeability. *Int. J. Rock Mech. Min. Sci. & Geomech. Abstr.* Vol. 18/5, pp. 429-435.
 116. Wang, M., and Kulatilake, P.H.S.W., Um, J., and Narvaiz, J., (2002), "Estimation of REV size and three dimensional hydraulic conductivity tensor for a fractured rock mass through a single well packer test and discrete fracture fluid flow modeling", in *Int. J. Rock Mech. Min. Sci.*, Vol. 39(7), pp. 887-904.
 117. Wang, J.A., Park, H.D., (2002) Fluid permeability of sedimentary rocks in a complete stress–strain process. *Engineering Geology*, Vol. 63, pp. 291-300.
 118. Wickham, G.E., Tiedemann, H.R. and Skinner, E.H. (1972) Support determination based on geologic predictions. In *Proc. North American rapid excav. tunneling conf.*,

- Chicago, (eds K.S. Lane and L.A. Garfield), New York: Soc. Min. Engrs, Am. Inst. Min. Metall. Petrolm Engrs, pp. 43-64.
119. Williams, P.F. (1977) Foliation: A Review and Discussion. *Tectonophysics*, Vol. 39, pp. 305-328
 120. Williams, A. F., (1980) The design and performance of piles socketed into weak rock. PhD thesis, Monash Univ., Melbourne, Australia.
 121. Witherspoon, P. A. and Gale, J. E. (1977) Mechanical and hydraulic properties of rocks related to induced seismicity. *Engineering Geology* Vol. 11, 23.
 122. Witherspoon, P. A., Wang, J. S. Y., Iwai, K. and Gale, J. E., (1980) Validity of cubic law for fluid flow in a deformable rock fracture. *War. Resour. Res.*, Vol. 16, 1016.
 123. Zisser, N., and Nover, G., (2009) Anisotropy of permeability and complex resistivity of tight sandstones subjected to hydrostatic pressure. *J. Appl. Geophys.* Vol. 68(3), pp. 356-370.
 124. Zhang Xing and Sanderson, J. David, (1995) Anisotropic features of geometry and permeability in fractured rock masses. *Engineering Geology*, Vol. 40, pp. 65-75.
 125. Zhang X, Sanderson D.J, Harkness R.M, Last N.C., (1996) Evaluation of the 2-D permeability tensor for fractured rock masses. *Int. J. Rock Mech. Min. Sci. Geomech. Abstr.* 33(1), pp. 17-37.
 126. Zhang, J. C., Zhang, Y. Z., and Liu, T. Q., (1997) Fluid flow in rock mass and water in-rush in floor strata of coal seam. *Geology Press*, Beijing (in Chinese).
 127. Zhou, B. Chuang, Sharma, S. Radhey, Chen, Yi, F., and Rong, Guan, (2008) Flow-stress coupled permeability tensor for fractured rock masses. *Int. J. for Numer. and Anal. Meth. Geomech.*, Vol. 32, pp. 1289-1309.
 128. Zhu, W., and Wong, T. F., (1997) The transition from brittle faulting to cataclastic flow: permeability evolution. *J. Geophys. Res.*, Vol. 102 (B2), pp. 3027-3041.
 129. Zimmerman RW, Al-Yaarubi AH, Pain CC, Grattoni CA., (2004) Nonlinear regimes of fluid flow in rock fractures. *Int. J. Rock Mech. Min. Sci* Vol. 41: 1A27.
 130. Zimmerman, R., and Bodvarsson, G., (1996) Hydraulic conductivity of rock fractures. *Transp. Porous Media*, Vol. 23, pp. 1-30.
 131. Zimmerman, R.W., and Yeo I. W., (2000) Fluid flow in rock fractures: from the Navier–Stokes equations to the cubic law. In Dynamics of Fluids in Fractured Rock, Faybishenko B, Witherspoon PA, Benson SM (eds). *American Geophysical Union Monograph 122*: Washington, DC; pp. 213–224.

SUMMARY

Investigation of permeability is important in understanding the behavior of fluid flow through the rockmass. Rockmass consists of, intact rock as well as discontinuities/fractures such as, joints, faults, shear zones, bedding plane, lineation, foliation, gneissosity etc. The behavior of fluid flow through the rockmass depends upon the properties of the rockmass (strength, modulus, and poisson's ratio), properties of fractures (orientation, length, density, aperture, roughness, in-filling materials, and inter-connectivity) and properties of the fluid (density and viscosity). Execution of any civil and hydro-geological engineering projects especially, in the hard and crystalline rockmass will bring about a concentration of stresses and subsequently local joints or tension fractures in the rock mass come into existence. Consequently, strength of the rockmass decreases and in addition, fluid flow through such rockmass results in the development of excess internal water pressure, which substantially reduces the effective normal stress. Such a situation may lead to failure of underground constructions (tunnel/mine roof, rock caverns, longwall mines, etc) and in-stability of deep and steep open cut slopes. Therefore, understanding the behavior of fluid flow (mechanics and transport of fluid) through a rockmass, especially occurring at great depth (>200 m) becomes essential.

In this regard, works of earlier researchers are worth mentioning, such as, non-linear flow behavior through fractured rockmass under different stress conditions and investigating fluid flow behavior through a fractured rockmass considering several factors such as, geometry of the fracture (aperture, length, density, orientation, interconnection of void spaces/fracture and fracture in-filling materials). Experimental results of on air flow tests conducted on a fractured granite specimen under triaxial test conditions have shown that the 'cubic law' expression used by for parallel plate theory, which assumes linear flow between two parallel smooth plates without having contact with each other can be employed to non-Darcian flow case for $Re \leq 3.5$ to $Re < 4$, depending on flow pressure. However, in general, most of the time, natural fracture surfaces are rough and irregular, contacting each other at discrete points. It has been stated that due to the rough/irregular fracture surface, error in flow estimation occur in terms of 1–2 order of magnitude, if modeled using parallel plate theory. It has also been reported that the effects of topography on fluid flow are negligible at low fluid pressures and large joint apertures, whereas, at elevated fluid pressures, fluid flow properties may not be modeled using conventional 'cubic law' because of the development of turbulent/non-linear flow.

Consequently, several non-linear relationships have been proposed to simulate flow through a fracture and the most commonly used ones are Forchheimer equation and Izbash equation. Also, few analytical solutions based on Buckley and Leverett and Barree and Conway models, were derived for non-Darcy displacement of immiscible fluids in porous media. It must be noted that the constants of these equations are mainly based on either numerical simulation or in-situ scale testing conditions. This calls for developing techniques that would facilitate measurement of permeability through the fractured rock masses under varied confining stresses and ground water pressures. Based on these studies efforts should also be made to develop a mathematical model which correlates these parameters with the rock mass specific parameters.

With this in view, an effort has been made to develop an experimentation technique that facilitates simulation of flow of water through the fractured rockmass by (a) using an analogue material - 'paraffin wax' and (b) naturally occurring rockmass, which imbibe a 'single fracture' and their details are presented here. Based on these studies, it has been observed that discharge decreases with an increase in effective stresses and variation in discharge and base pressure shows linear relationship and deviation occurs due high base pressure. Reynolds number and pressure gradient relationship is quite sensitive to the base pressure and fracture roughness. Further, there is a critical base pressure, beyond which transition in laminar to turbulent flow occurs. It has also been observed that discharge decreases with increase in the sample size, and increases with an increase in fracture aperture. The study has demonstrated the usefulness of analogue material for easy and fast simulation of fluid flow properties of the rockmass in cost effective manner and by avoiding a collection of the undisturbed rock samples from the deep locations and creation of the fracture(s) in it, which becomes a cumbersome and tedious task under a laboratory conditions.

PUBLICATIONS

Singh, K.K, Singh, D.N., and Ranjith, P.G., 2014. “Simulating Flow through a Fracture in the Rockmass using Analogue Material”, *International Journal of Geomechanics, ASCE*, 14:8-19. DOI: 10.1061/(ASCE)GM.1943-5622.0000295.

Singh, K.K., Singh, D.N., and Ranjith, P.G., 2012. “Permeability of the Fractured Rockmass” - A review, *22nd Australasian Conference on the Mechanics of Structures and Materials “Materials to Structures: Advancement through Innovation”*, (ACMSM 22), Sydney, Australia.

Singh, K.K, Singh, D.N., and Ranjith, P.G., 2013. “Laboratory Simulation of Flow through Single Fractured Granite” *Rock Mechanics and Rock Engineering*, (under review).

Singh K.K., Singh, D.N., and Ranjith, P.G., (2012), Permeability of the fractured rockmass - A review. *Journal of Civil Engineering and Architecture* (under review).

Patel, A, Singh, D. N., and Singh, K.K., 2010. “Performance Analysis of Piezoceramic Elements in Soils”, *Geotechnical and Geological Engineering*, 28:681-694.

Patel, A., Singh, K. K., and Singh, D. N., 2011. “Application of Piezoceramic Elements for Determining Elastic Properties of Soils”, *Geotechnical and Geological Engineering*, DOI: 10.1007/s10706-011-9476-z.

ACKNOWLEDGEMENT

I wish to express my sincere gratitude towards my supervisors, Prof. D. N. Singh and Prof. Ranjith P. G., for their guidance, continuous encouragement and thorough motivation throughout the research program.

I also thanks to the IITB-Monash Research Academy and BHP Billiton for giving me opportunity to work on the given project.

I am thankful to the members of my research progress committee Prof. T. N. Singh and Prof. J. N. Mandal, Dr. Daniel Viète, and Prof. T. Xi for their critical comments and suggestions, which has helped in improving various aspects of my research work.

I would like to thank staff of soil engineering laboratory, Mr. H. D. Rane, Mr. Kadam and Mr. Chalke, and Civil Engineering office staff for their support during the course of my research work.

Thanks are also due to my friends, to name a few, Dr. S. Shathakumar, Dr. Anjan Patel, Dr. Hanumantha Rao, Dr. B. Jha, Dr. K. Srinivas, Dr. K. Venkat Uday, Dr. G.P. Padmakumar, Mr. B.S. Patil, Mr. S. Shinde, Ms. S. Gurnani, Ms. Sneha J., Mr. Ravitej P., Ms. Pankaj Pathak, Mr. Kannan Iyer, Mr. Prakash Kumar Singh and many unnamed, for their constant support and cooperation which was quite significant throughout my stay at this campus.

I would also like to bestow my love and respect to my family who has continuously supported and encouraged me during the course of this study.

Finally, I would also take this opportunity to remember “The Great Almighty” whose blessings have helped me to reach the goal.



Kunal Kumar Singh